博士論文（要約）

Doctorate Thesis (digest)

Effect of the contact states on electron transport of single molecule systems within an STM junction

（STM ジャンクション中の一分子の電子輸送特性とコンタクト状態の研究）

Department of Advanced Materials Science
Graduate School of Frontier Science
The University of Tokyo

東京大学大学院 新領域創成科学研究科 物質系専攻

Ryoichi Hiraoka

平岡　諒一

Contents

Chapter 1
Introduction

1.1 General Introduction

In materials science, it has become important to control, design and measure samples with the nanoscale resolution. The trend of the microscopic investigations arises from both scientific and technological requests, which is now known as nanoscience and nanotechnology.

For example, in condensed matter physics, the macroscopic physical properties of materials, such as the mechanical strength, the heat capacity, the electrical conductivity, the magnetism and so on, cannot be explained without quantum theory based on the ideas of the atoms and electrons. Quantum physics provides us the way to systematically understand physical properties of materials such as the band theory, which describes the behavior of electrons in the materials. Consequently, quantum physics is absolutely necessary in a frontier of condensed matter physics to explore novel phenomena, which are not basically observable in the macroscopic scale experiments. Quantum theory is also important in chemistry. For instance, in order to understand the mechanism of chemical reactions such as catalytic reactions, we need to know each elementary step in the reaction at a single molecule level.

Both nanoscience and nanotechnology develop like the two wheels of a cart. The developments in nanoscience has contributed to the industrial technology and engineering; the knowledge in condensed matter physics is essential for the recent electronic devices, and the design of chemical reactions cannot be achieved without the

knowledge of chemistry based on quantum theory. In turn, developments in nanotechnology raise further questions to be investigated in nanoscience. Basic studies on physical and chemical phenomena at the nanoscale have been performed to obtain insights for improving functions of devices and catalysts, and for realizing novel and desired functions.

Under such trend of nanoscience, it is now essential to characterize physical properties at a single molecule level. Scanning tunneling microscope (STM) has greatly contributed to nanoscience. STM is one of probe microscopes, which was invented by Binnig and Rohrer in 1982[1,2]. The characters and advantages of STM are briefly summarized as follows;

(1) STM provides us the real-space images of a conductive surface with the atomic resolution. We can identify a position of a single adsorbate on the surface. Combination with the cryogenic condition enables us to perform a spectroscopy measurement known as scanning tunneling spectroscopy (STS)[3,4].

(2) STS provides us information about the electronic states of the surface near the Fermi level (E_F). Due to the spatial resolution of STM, the local electronic states at the position of the STM probe (generally called STM tip) can be obtained in STS, i.e., the electronic states of the single adsorbate is measureable.

(3) Furthermore, STS spectra contain information of inelastic excitation processes such as the vibration excitation and the magnetic excitation, which is known as inelastic electron tunneling spectroscopy (IETS)[5-8].

(4) STM can be used as the nano-size tweezers as well as the microscope, which is known as the STM manipulation technique. Thanks to the atomic sharpness of the STM tip apex, we can manipulate the adsorption site and geometry of the single adsorbate[9,10]. In addition, we can induce the chemical reactions[11,12]

by the precise control of the STM tip position, bias voltage and tunnel current. In the STM manipulation techniques, the atomic force and the energy of the tunnel electrons are generally used to induce the changes and reactions. The STM tip works as the source of the external perturbation for the adsorbate.

(5) The STM manipulation technique enables us to construct a nano-junction of the single adsorbate, where the STM tip contacts the adsorbate. We can observe the electronic states of the adsorbate as a function of the STM tip-adsorbate distance from the tunnel region to the contact region. We call this measurement as the STM contact measurement in this thesis.

In spite of a few imperfections and drawbacks, STM is an exclusive experiment technique in the researches on the nanotechnology and quantum physics.

1.2 Outline of This Thesis

In this thesis, we present that the STM contact measurement provides us valuable information of physical properties of materials at the single molecule level. The STM contact measurement reveals the electron transport characteristics of the molecule in the junction together with the contact state: the geometrical configuration and electronic states of the molecule in the junction. In addition, we can *in-situ* control the local environment of the molecule by the STM contact measurement; the interaction between the molecule and substrate can be controlled by lifting up the molecule. We can induce the external perturbation by the approaching STM tip. Hence, the effect of the electrode (STM tip) on the molecule can be investigated by comparing the results of the STM contact measurement and the STM and STS measurements (non-contact situation).

This thesis is organized as follows:

Chapter 1. Introduction.

Chapter 2. Experimental Methods.

Chapter 3. Electron Transport of Fullerene (C_{60}).

Chapter 4. Electron Transport of Silicene Nano Ribbon (SiNR).

Chapter 5. Magnetic Properties of Iron(II) Phthalocyanine (FePc) Junction.

Chapter 6. Summary and Outlook.

The results and discussion are provided in Chapter 3, 4 and 5. Three different systems, which are related to three different topics, are investigated by the STM contact measurement in Chapter 3, 4 and 5, respectively. In the following sections, we describe the backgrounds and current problems of the topics and our approach to solve the problems by using STM.

1.3 Electron Transport Channel

1.3.1 Single Molecule Device

Single molecule device is a device where a function of the device is fulfilled by a single molecule. The expected usage of the single molecule device is the complementary of electronic devices, which are generally made of semiconducting bulk materials (especially silicon-based materials) in the current industries. Compared to the semiconducting bulk materials, the expected advantages of the single molecule device are as follows; since the molecule is small and stable compared to metal and semiconducting clusters, the single molecule device is expected to be an ultimately miniaturized device, where the devices of bulk materials cannot reach. In addition, the variety of molecules due to the chemical

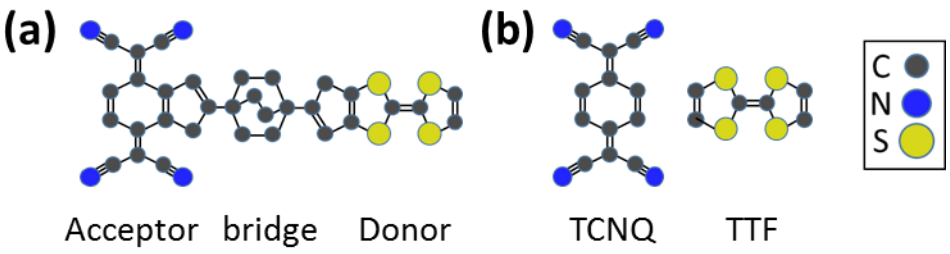

Fig. 1.1. (a) Model structure of the rectifier molecule. (b) Structures of TCNQ and TTF. Hydrogen atoms are omitted in both models.

modification may enable us to design, control and realize unique functions in the device which is difficult for bulk materials. Theoretical studies have suggested several single molecule devices utilizing unique characters of molecules; a switching function by the photo-isomerization of a molecule[13], utilizing the rotation of functional groups by the electric fields[14], realizing a spintronic device by a metal-organic complex[15,16] and so on.

The concept of the single molecule device was proposed by Aviram and Ratner in 1974[17]. In their work, they mentioned both the progress in the semiconductor electronic devices such as the transistor and integrated circuits and the discovery of electron-conductive (and superconductive) organic crystals[18]. Motivated by these developments in the solid-state devices and the organic materials, they suggested and theoretically considered a single molecule rectifier (diode). Figure 1.1 shows one of the example molecules investigated in their work. This molecule is a mimic of the p-n junction which is a typical diode. Focusing on the molecular framework, this molecule is divisible to three parts: a framework of an electron-acceptor molecule tetracyanoquinodimethane (TCNQ), an electron-donor molecule of tetrathiafulvalene (TTF) and a methylene bridge part connecting both the donor part and acceptor part. Since the π-electron systems in the donor and acceptor part are separated by the σ-bonds

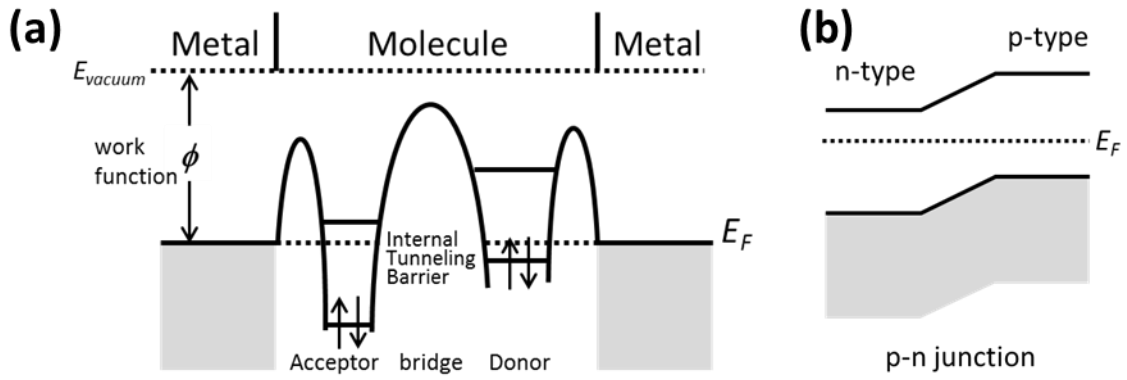

Fig. 1.2. (a) Schematic energy diagram of the single molecule junction proposed in Ref. [17]. (b) Schematic band diagram of the p-n junction. Gray regions represent the filled states (valence states).

of the bridge part, the electronic states and properties of the π-electron systems such as the ionization potential and electron affinity are expected to remain unchanged from the original states of the isolated molecules. The bridge part consisting of σ-bonds is regarded as a potential barrier region when the electron transfer between the donor and acceptor part can be described by the tunneling mechanism. Supposing a weak interaction between the molecule and metal electrodes, the energy diagram of the single molecular junction is drawn as shown in Fig. 1.2(a). Since the energy diagram is similar to that of the p-n junction, the molecule is expected to show the diode characteristic. They theoretically calculated the *I-V* characteristics of the single molecular junction and actually obtained a clear diode characteristic in the *I-V* characteristics of single molecular junction. Although the model was too simple, their work motivated the research field of the single molecule device, which remains an attractive topic today.

In the next section, we will introduce the mechanism and formulation of the electron transport in a nanoscale sample such as the single molecular junction.

1.3.2 Electron Transport in Nano-constriction, Atom and Molecule

To begin with, we will briefly introduce the carrier transport in the macroscopic region and then in the mesoscopic region. In the macroscopic region, the most fundamental expression of the carrier transport is the Ohm's law. In a more detail description based on the quantum physics, the carrier transport is described as follows; electrons are accelerated by the uniform electric field of the bias voltage and scattered in the time constant τ. The conductivity of a material is obtained by the Boltzmann equation under the relaxation-time approximation, which is expressed by the products of the density of states (DOS), the relaxation time τ and the Fermi velocity of electrons. For example, the conductivity σ of a simple three-dimensional isotropic metal is given in the form;

$$\sigma = \frac{1}{3} e^2 \tau v_f D, \tag{1.1}$$

where e is the elemental charge, v_f is the Fermi velocity and D is the DOS at the E_F. Although too simple, this expression shows the important description about the conductivity of bulk materials; the band structure of a material, which contains both information of the DOS and the Fermi velocity, is important.

In contrast, when the scale of the system decreases to the mesoscopic region, the above model of the carrier scattering is no longer valid because the mean free path of carriers is comparable to the size of the system. The carriers can pass the sample without being scattered in this situation. In other words, the electron can transmit coherently as a wave, without losing the information of the phase of its wave function. The carrier transport in the mesoscopic sample was theoretically considered by Landauer[19-21]. He showed that the quantization of the conductance appears in the situation, which were experimentally observed later[22]. Let us describe the conductance quantization by employing a simple one-dimensional model below. The model consists of left and right

electrodes and a sample, as shown in Fig. 1.3. We introduce the following assumptions;

(1) The effective temperature is absolute zero, i.e., the electronic states under the chemical potentials are fully occupied for both electrodes.

(2) The potential difference caused by the bias voltage V_b is concentrated at the sample. The bias voltage introduces a difference in the chemical potential of the left and right electrodes μ_L and μ_R:

$$V_b = (\mu_L - \mu_R)/e\,. \tag{1.2}$$

(3) In the left electrode, we consider only the electrons which are moving right.

(4) Each electrode has sufficiently high density of states as electron reservoirs. The electrodes are in the equilibrium under the bias voltage and the current.

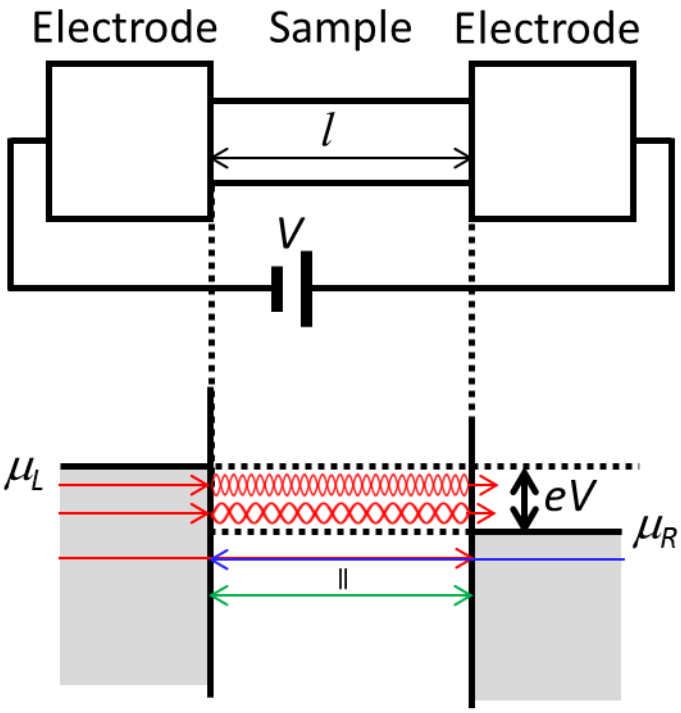

Fig. 1.3. Schematic picture of the one-dimensional Landauer model. The lower panel represents the energy diagram. The chemical potentials of the left and right electrodes are $\mu_{L,R}$. The red (blue) color indicates the right (left) moving mode and the red waves represent the wave functions in the sample. Electronic states with the energy below μ_R do not contribute to the net current across the junction (green).

(5) All electrons reaching the electrodes are captured by the electrodes. There is no scattering and reflection at both inside and interface of the sample and electrodes.

Under these assumptions, the contribution to the current from the electron with wave number k is expressed as

$$j(k) = \frac{e}{\hbar}\frac{1}{l}\frac{dE(k)}{dk}, \tag{1.3}$$

where $\hbar$ is the plank constant h divided by 2π, l is the length of the sample and $E(k)$ is the energy of the electron whose wave number is k. The total current across the sample is obtained by a summation in the region of potential difference:

$$J = \int_{k_R}^{k_L} j(k)\frac{l}{2\pi}dk = \frac{e}{h}\int_{\mu_R}^{\mu_L} dE = \frac{e}{h}\left(\mu_L - \mu_R\right). \tag{1.4}$$

Substituting Eq. (1.3) into Eq. (1.4) yields,

$$J = \frac{e^2}{h}V_b. \tag{1.5}$$

Considering the spin degrees of the freedom, the conductance G is obtained as:

$$G = \frac{J}{V_b} = \frac{2e^2}{h} \approx \left(12.9\ \mathrm{k\Omega}\right)^{-1}. \tag{1.6}$$

Eq. (1.6) indicates that the conductance is quantized to a universal value, which is known as the conductance quantum or the quantized conductance G_0. The obtained conductance is independent of the band structure of the sample. Hence, a single electronic state in the sample exhibits the conductance G_0. When there are several states (the total number is n) which can transport carriers across the junction, the total conductance of the sample is written as nG_0. Here, we call the electronic states as transport channels and n as the number of transport channels. In addition, when the reflection of carriers at the interface occurs due to the potential barrier at the interface, the conductance is given by introducing the transmission coefficient τ:

$$G = G_0 \sum_{i=1}^{n} \tau_i \,. \tag{1.7}$$

This is called the Landauer formula, describing the conductance in the mesoscopic sample; the total conductance of the sample G is given by the summation of contributions from each transport channel $\tau_i G_0$.

According to the theoretical studies above, the transport channels in the single molecular junction correspond to the electronic states of a molecule inside the junction. Since we focus on the electron transport under small bias voltage, electronic states around the E_F is important, i.e., the highest occupied molecular orbital (HOMO) and lowest unoccupied molecular orbital (LUMO) are important.

In order to obtain the deeper insight on the electron transport phenomenon, especially, on the role of the molecular electronic states, we have to determine the key quantities n and τ. It is of great importance to discuss the relation between the parameters (n and τ) and the molecular orbitals. Furthermore, experimentally unveiling the effect of geometrical configurations of the molecule on the transport characteristics is also required, which is often considered in the theoretical studies. We need a special method to quantitatively determine these parameters as well as to visualize the molecular configuration in the junction for the reason below: although the total conductance ($G = I/V$) can be easily obtained by measuring the current (I) under the bias voltage (V), we cannot decompose G into the contributions from each transport channel determine $\tau_i G_0$. In the next paragraph, the experimental methods to determine n and τ will be introduced.

1.3.3 Mechanically Controllable Break Junction (MCBJ) and Transport Channel Analysis

Experiments on the single molecular junction has been successfully done in the last two decades. One of the experimental method is called mechanically controllable break junction (MCBJ) method[23-26]. The experimental set-up of the MCBJ method is schematically illustrated in Fig. 1.4. An etched metal wire is placed and glued-on a stage covered by an insulating film. The constriction part of the metal wire is in the target molecule atmosphere, generally in the aqueous solution. A piezo-electric device under the stage pushes the stage, followed by bending of the stage and the metal wire. Then,

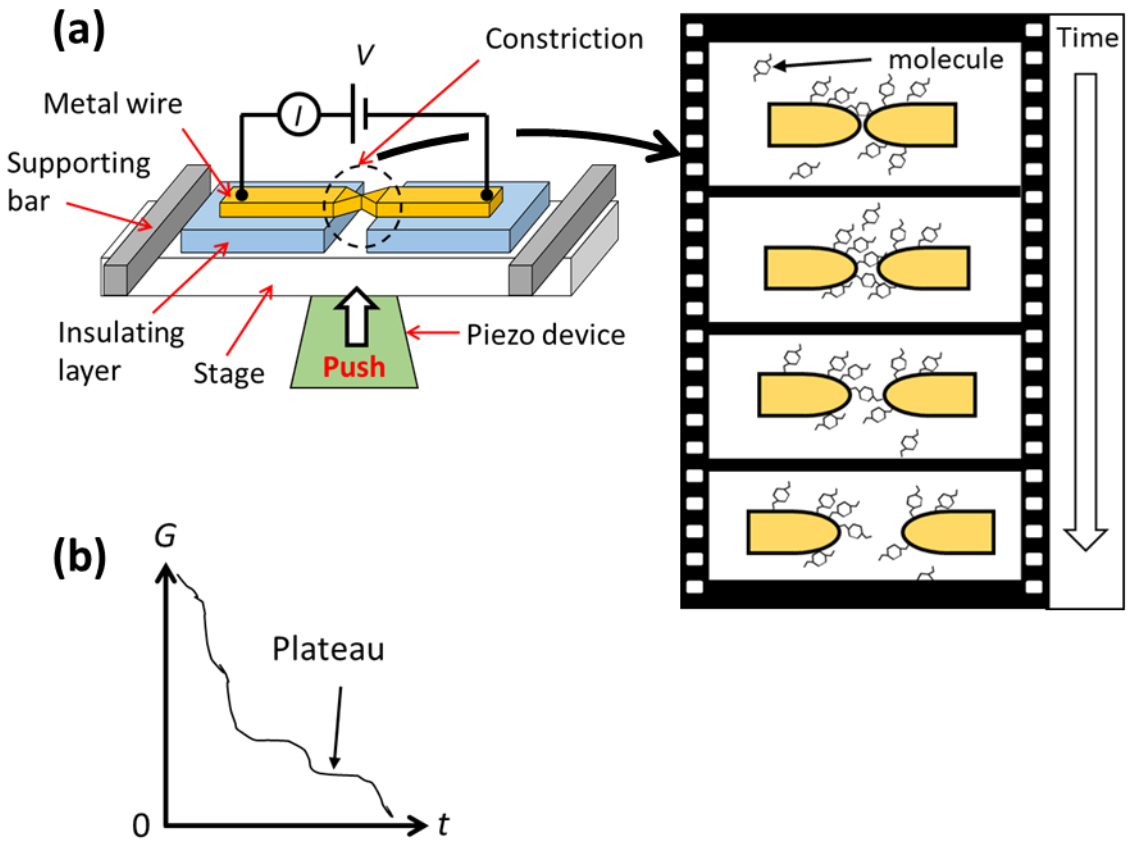

Fig. 1.4. (a) Schematic image of the set-up of the MCBJ measurement and the procedure of the MCBJ measurement. (b) Schematic image of the conductance trace obtained in the MCBJ measurement..

the constriction of the metal wire breaks and the target molecule is trapped in between the broken junction. Finally, the junction is broken with the gap larger than the molecule. For the next measurement, the piezo-electric device returns to the initial position and the gap of the metal wire is closed. During the measurement, the current I across the junction is measured under a certain bias voltage V. The increment of the applied voltage to the piezo-electric device is constant. The current I or the conductance G (= I/V) is plotted as a function of time, which is called current (or conductance) trace [Fig. 1.4(b)]. The formation of the single molecular junction is judged by the appearance of a plateau because the conductance of the single molecule is a certain value unique to the molecule and the conductance value is expected to be kept for a certain distance due to the flexibility of the molecule. Due to the randomness in the MCBJ method, the conductance traces are repeatedly obtained and the conductance histogram is presented in order to determine the conductance value of the single molecular junction.

By the MCBJ method, the conductance values of various single molecular junctions have been determined; for example, the self-assembled monolayer (SAM) of hydrocarbons[24], benzene derivatives[25,26] and larger molecules such as DNA[27]. Several metal electrodes are also tested such as Au, Ag and Pt. Experiments on simple molecules revealed the relationship between the conductance of the single molecular junction and the types of molecules and electrodes[28], which is in good agreement with the theoretical expectations. Figure 1.5 shows the conductance of single molecular junctions with several molecules and electrodes. The magnitude of the conductance is well explained by the electron hopping model; the anchoring group, the DOS of the electrodes at the E_F and the bonding strength between the molecule and electrodes strongly affect the conductance[28]. Not only the investigation of basic physical phenomena, but also the exploration of device functions in the single molecular junction

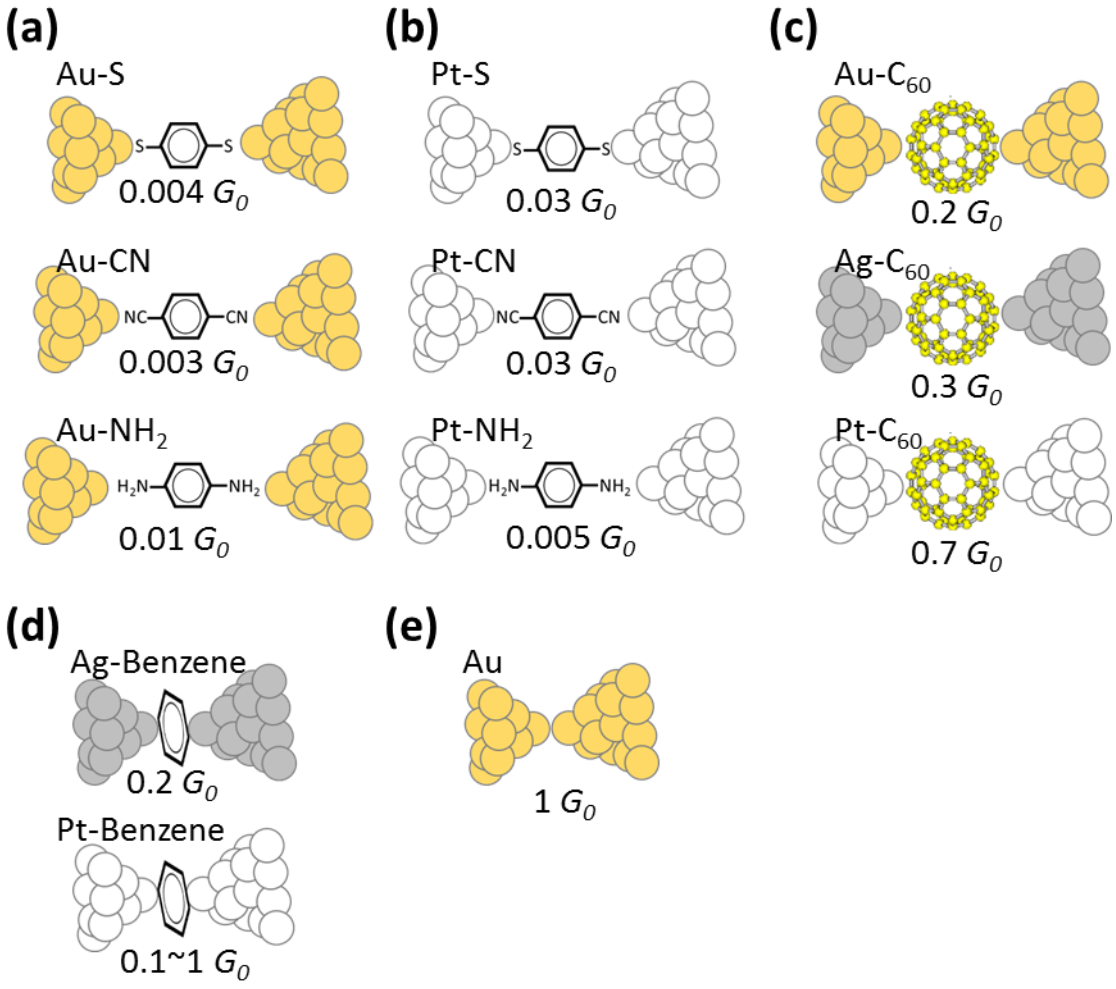

Fig. 1.5. Conductance of single molecular junctions determined by the MCBJ method (values are obtained from Ref. [28]). (a) Benzene derivatives bridging the Au. (b) Benzene derivatives in the Pt electrodes. (c) Fullerene (C_{60}) molecule in the Au, Ag and Pt electrodes. (d) Benzene molecule flatly sandwiched by the metal electrodes. (e) Metal point contact of the Au electrodes.

has been performed. Indeed, the diode characteristic was discovered[29].

Although the MCBJ method has been successfully applied to study the electron transport in nano-constrictions, the MCBJ method is not sufficient to investigate the detail physical phenomena in the single molecular junction. The molecular configuration in the junction is not visible. Furthermore, the local condition around the broken junction is expected to be complicated because the measurements are conducted in the aqueous solution condition. The statistical treatments may also cause a burying of important

information. We have to perform more precise measurements to provide detail information enough to discuss more basic physics in the single molecular junction; the effect of the molecular configuration on the electron transport properties of the single molecular junction. Using STM is one solution for this point. Together with STM observation, STS and STM manipulation technique under the ultrahigh vacuum and cryogenic condition, we can construct and characterize the single molecular junction in a well-defined manner.

In the following paragraphs, we introduce the experimental techniques to determine the electron transport characteristics n and τ. As mentioned, we cannot decompose the total conductance into the contributions from each transport channels in the conventional conductance measurements. Two methods have been reported for the determination of the parameters n and τ; the one is using superconducting metal electrodes[30-32] and the other is measuring the shot noise[33-36].

In the former method, the I-V characteristics of the junction strongly depend on the parameters n and τ due to the multiple Andreev reflection (MAR) process appearing in the junction with superconducting metal electrodes[37]. We briefly show the characters of the current flowing in the junction of the superconducting electrodes. Principles of the Andreev reflection and the MAR are given in Appendix. According to the simple formulation[37], where the right and left superconducting metal electrodes are identical and the effective temperature is absolute zero, the current I is expressed in the following form;

$$\begin{aligned} I_{total}(V) &= \sum_{i=1}^{n} I_i(V,\tau_i) \\ I_i(V,\tau) &= \sum_{m=1}^{\infty} \tau^m \, \theta(meV - 2\Delta) K_m(V,\tau) \end{aligned} \quad . \tag{1.8}$$

Here, the total current I_{total} is given by a summation of the contributions from each transport channel I_i. θ is the Heaviside step function, Δ is the superconducting gap of the electrodes, m is a number of the MAR process and K_m represents a coefficients of the m-times MAR process. Due to the term τ^m and the step function, the current of each channel I_i strongly and nonlinearly depends on the transmission coefficients τ and the bias voltage V. This I-V characteristic is called sub-harmonic gap structure (SGS) since it appears inside the superconducting gap region. As a result, we can identify the number of transport channels and their transmission coefficients by analyzing the total current I_{total}.

In the latter method, the shot noise appearing in the current depends on the parameters n and τ. According to quantum statistics, the shot noise power from one transport channel S_i is expressed as

$$S_i = 2eV G_0 \tau_i (1-\tau_i), \tag{1.9}$$

at the absolute zero temperature[34]. The total shot noise under the infinite temperature T is given in this from:

$$S = G_0 \sum_{i=1}^{n} 2eV \coth\left(\frac{eV}{2k_bT}\right)\tau_i(1-\tau_i) + 4k_bT\tau_i^2, \tag{1.10}$$

where k_b is the Boltzmann constant.

In practice, both methods have several difficulties; in the former method, the element of electrodes is restricted to superconducting metals. High energy resolution is required in the I-V measurements because the information about n and τ appears inside the superconducting gap region, which is typically several meV around the E_F. In the latter method, the treatment of the noise is basically difficult. Various noises which has no physical information about the transport channels arise from the external and internal factor in the experiments. At present, there are several reports on the transport channels; the parameters of transport channels n and τ were determined by the shot noise

measurement with the MCBJ method for small molecules such as hydrogen[34] and benzene[35]. By using superconducting electrodes, the atomic nano wires were studied[30-32]. The sample is expected to be the atomic point contact system. The *I-V* spectra of the junction clearly shows the SGS and the parameters n and τ were determined, as shown in Fig. 1.6. Even larger wire was also studied in Ref. [38]. In addition, SGS was observed when a molecule is inside the superconducting metal electrodes[39].

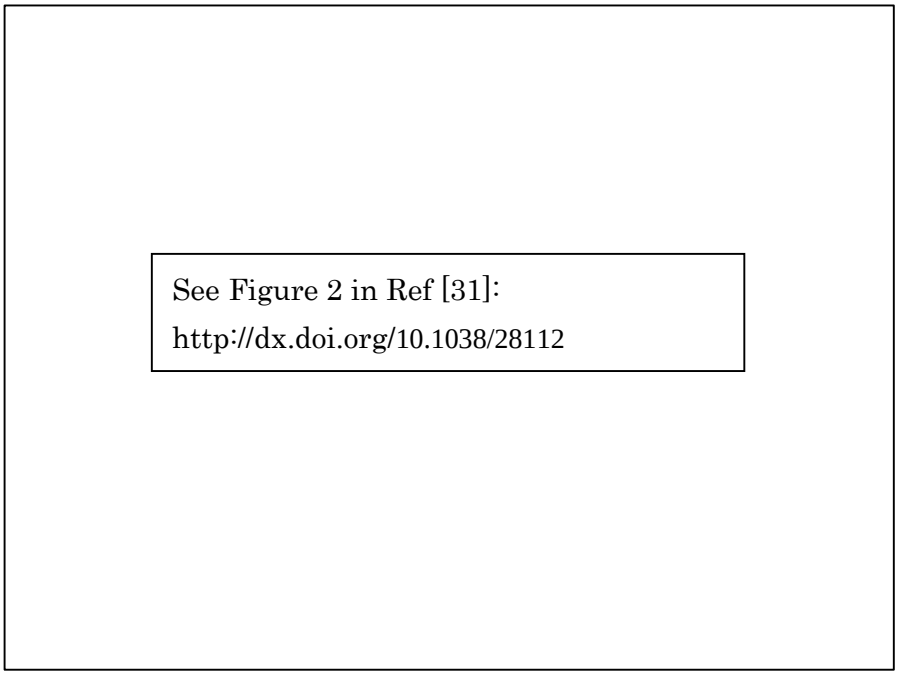

Fig. 1.6. *I-V* spectra of the Pb metal nano junction at T = 1.5 K (adopted from Ref. [31]). The curves a ~ d are obtained at around G = 1.4 G_0 and curve e is obtained in the tunneling regime. The curve (5) represents the typical *I-V* characteristic of the superconductor junction, where almost zero current appears under V = 2 (Δ/e). The superconducting gap Δ is 1.37 meV. For the curves a ~ d, the transport channels were determined as; τ_i = (0.955, 0.355, 0.085, 0.005) for the curve a, (0.89, 0.36, 0.145, 0.005) for b, (0.76, 0.34, 0.27, 0.02) for c, (0.65, 0.34, 0.29, 0.12) for d and (0.026) for e.

1.3.4 Purpose of the Study: Electron Transport Channel

Investigating the electronic properties of the single molecular junction is essential to the developments of future single molecule devices. One of the challenges is the experimentally determining the electron transport characteristics: the number of transport channel n and their transmission coefficients τ. For the deeper understanding of the electron transport phenomenon, we have to investigate the relation between the key parameters and the transport mechanism. We have to unveil the role of the electronic states of the molecule (especially LUMO and HOMO) on the parameters n and τ; the energy level alignment of the electronic states and the geometrical configuration of the molecule must be discussed.

Using STM with the superconducting metal substrate and tip is an effective way to answer the problems. STM observation enables us to identify the position and configuration of the single molecule on the substrate. STS helps us to investigate the electronic states of the molecule on the substrate around the E_F, i.e., we can access the HOMO and LUMO of the molecule, which are expected to be the origin of the transport channels. STM manipulation technique enables us to construct the single molecular junction in a well-defined manner and to measure both the conductance of the single molecular junction as well as the I-V characteristics. By using superconducting substrate and tip, the MAR occurs and the SGS is observed in the I-V characteristics, where we can analyze the number of transport channel n and their transmission coefficients τ.

In this thesis, we report the results on the fullerene (C_{60}) molecular junction with the superconducting Pb(111) substrate and Nb tip. In Chapter 3, we will describe and discuss in detail the results of the experiments as below: (a) Construction of the Nb-C_{60}-Pb(111) junction, (b) I-V characteristics of the C_{60} junction and the observed SGS, (c) analysis

procedure and the determined parameters n and τ, (d) the transport characteristics of different molecular configurations, (e) STS spectra of C_{60} on Pb(111) and the relationship between the transport characteristics and the electronic states of C_{60}.

1.4 Honeycomb Materials

1.4.1 Dirac Electron System in Honeycomb Lattice

Honeycomb lattice is one of the most attractive two-dimensional (2D) structures observed in layered materials. Graphene, a single layer of graphite, is the most famous 2D honeycomb materials. Although graphene was hidden behind other carbon allotropes such as fullerene[40] and carbon nano tube[41], graphene is now under the spotlight from

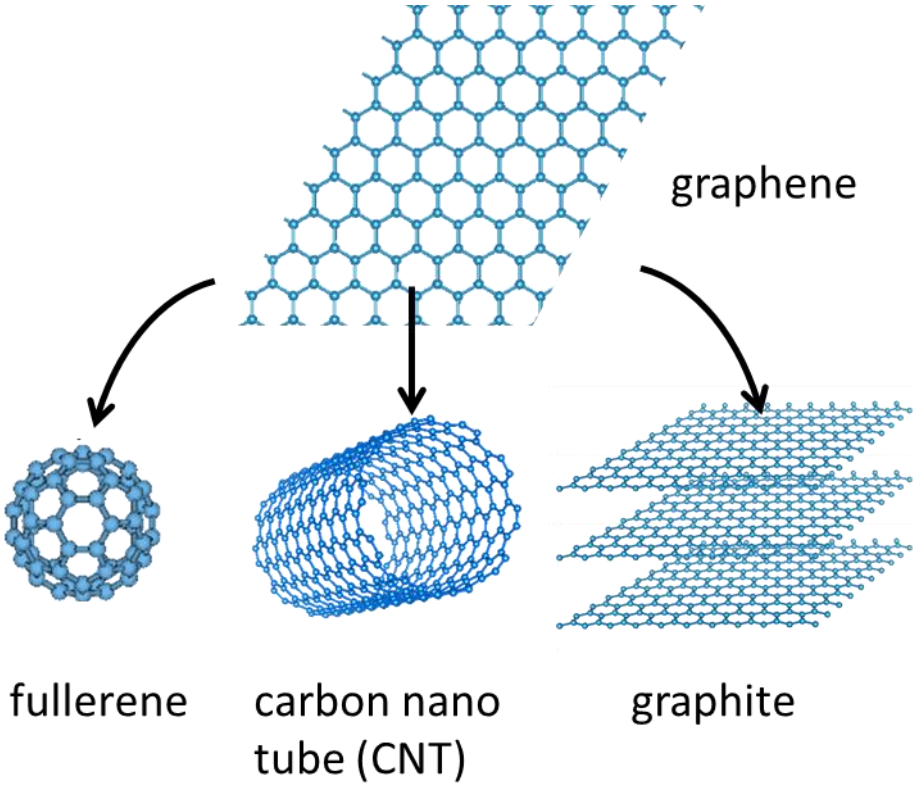

Fig. 1.7. Graphene and other carbon allotropes which have the π-electron system.

both scientific and industrial points of view as a key material which have π-electron systems (Fig. 1.7). After the successful fabrication by Novoselov et al. in 2004[42], graphene has been intensively studied because of its unique and remarkable quantum properties; electronic properties such as the high electron mobility[42] and the anomalous Hall effect[43], the optical properties[44], and thermal and mechanical stabilities[45,46], etc. Due to these properties, there are many approaches to realize the graphene based applications; used as a thin, light and strong membrane[46], electrode materials and catalysts[47] as well as electronic/optical devices and future spintronic devices[48].

The electronic and optical properties of graphene are characterized by the following key words: the Dirac cone and the Dirac electron. The Dirac cone is a linear band structure appearing at the E_F and at the K point[49] [Figure 1.8(b)]. Since the linear band dispersion is identical to that of the relativistic particle "massless Dirac fermion", the effective mass of the electron in the linear band can be regarded as zero and hence the electron is called the Dirac electron. The Dirac cone and Dirac electron arise from the honeycomb structure. The unit cell of the honeycomb lattice contains two atoms, as

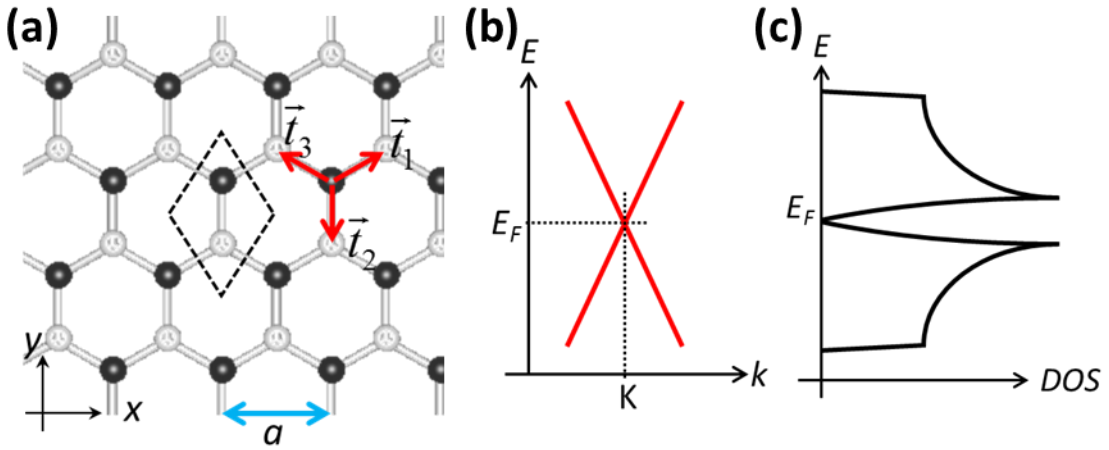

Fig. 1.8. (a) Schematic structure of graphene. The dotted diamond is the unit cell. White and black circles represent atoms in different sublattice. (b) Band structure of π-electrons in graphene at around the K point. (c) DOS of graphene around the E_F.

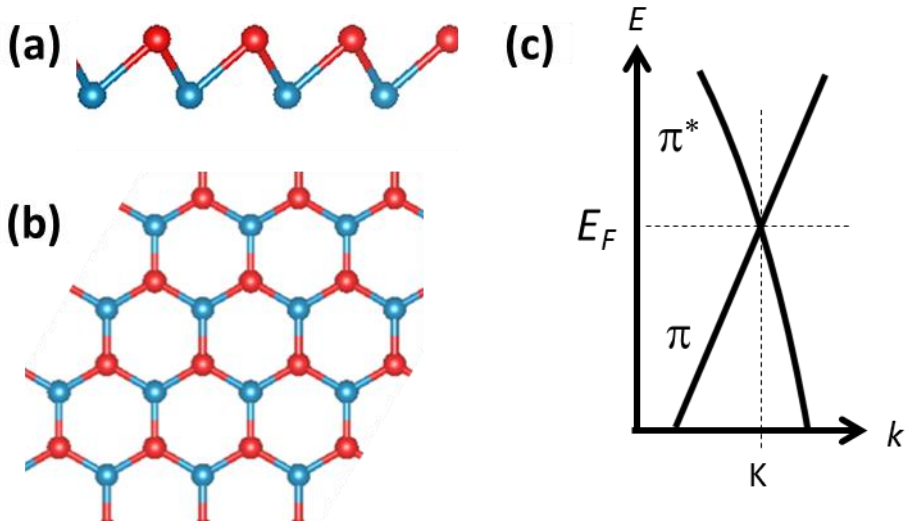

Fig. 1.9. Schematic model structure of silicene: (a) side view and (b) top view. (c) Calculated band structure of the low-buckled silicene at around the K point (see Ref. [50]).

shown in Fig.1.8(a). Figure 1.8(b) schematically shows the calculated band structure of the honeycomb lattice based on the tight binding model. Note that only the π electrons are considered in the tight binding model.

Since the 2D honeycomb lattice hosts the Dirac electron, the honeycomb lattice consists of other elements could also have the Dirac electron system. The honeycomb lattice consists of Si and Ge, which are in the same group in the periodic table as carbon, have been investigated theoretically[50,51]. These honeycomb materials are now known as silicene and germanene. We will briefly introduce the studies on silicene below. In contrast to graphene, silicene and germanene do not exist in nature. According to the theoretical studies, silicene and germanene are thermodynamically stable and host the Dirac electron system similar to graphene. The proposed structure of silicene is not perfectly flat but slightly buckled structure as shown in Fig. 1.9. The buckled structure is favored because the outermost shell of Si is the third shell; the chemical bonds of Si are composed of 3s and 3p orbitals. In the case of carbon, 2s and 2p orbitals hybridized to form the planer sp^2 bonds, and hence the planer structure is achieved. In contrast, the

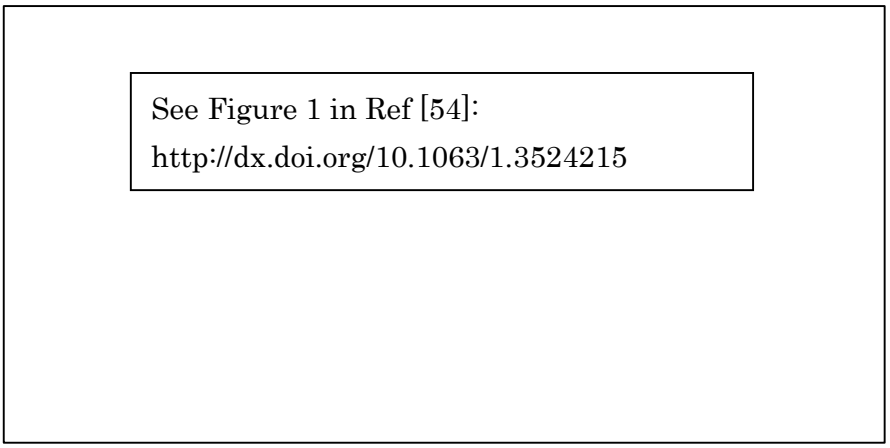

Fig. 1.10. STM images of the single layer silicene on Ag(111) (adopted from Ref. [54]). Reprinted with permission from [B. Lalmi, H. Oughaddou, H. Enriquez, A. Kara, S. Vizzini, B. Ealet, and B. Aufray, Applied Physics Letters **97,** 223109 (2010)]. Copyright 2010, AIP Publishing LLC.

perfectly hybridized sp^2 orbitals from 3s and 3p orbitals are unstable, and hence the sp^3 character is mixed into the sp^2 orbitals[52]. Therefore the buckled structure is formed. Although the structure is not planer and the perfect π electron system like graphene does not seems to be achieved, the buckled honeycomb structure of Si still has the Dirac cone at the K points.

The experimental synthesis and observation of silicene began with the work by Leandri et al. in 2005[53]. They deposited Si atoms onto the Ag(110) substrate and found self-assembled one-dimensional stripe nano structures, which is now called silicene nano ribbon (SiNR). The first report on 2D silicene was presented in 2010[54], where silicene was synthesized on Ag(111). Figure 1.10 shows the STM image of silicene. Although a commensurate 2D structure was obtained, the electronic properties investigated by STS[55] revealed that the Dirac electron system is not realized in the silicene on Ag(111). Figure 1.11 shows STS spectra of silicene on Ag(111) under the magnetic fields perpendicular to the surface. There are no peak structure attributable to the Landau levels, which are the direct evidence of the Dirac electron system.

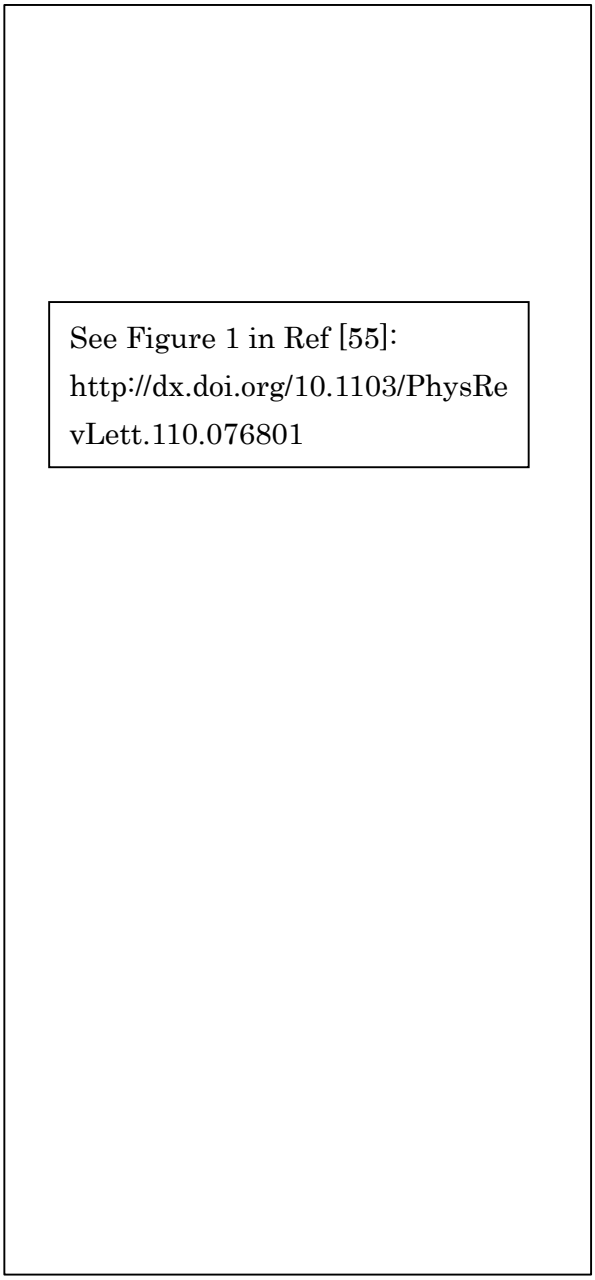

Fig. 1.11. (a) STM image of the single layer silicene on Ag(111). (b) Close-up image. (c) STS spectra obtained on silicene. Additional peaks do not appear under the magnetic fields 3 T and 7 T. (d) STS spectra of the HOPG sample. The peaks marked by symbols represent the Landau levels. (all figures are adopted from Ref. [55].)

The STS spectra of graphite (highly oriented pyrolytic graphite: HOPG) are also shown as reference in Fig. 1.11, where the Landau levels are clearly observed. Theoretical calculations of silicene with the Ag substrate also indicate the absence of the Dirac electron system due to the hybridization of electronic states between Si and Ag[55-57]. The strong hybridization of the electronic states indicates the formation of the bonding between Si and Ag, resulting in the vanishment of the delocalized π electron system, which serves as the Dirac electron system. These results pointed out that controlling the interaction between silicene and a substrate is the key to realize the Dirac electron system in silicene.

Consequently, one approach to realize the Dirac electron system in silicene is to find a suitable substrate, which supports silicene and has weak interfacial interaction with silicene. In terms of reducing the interaction between silicene and a substrate, semiconducting and insulating substrates would be candidates. Theoretical calculations predict that MoS_2 and hexagonal boron nitride would be promising candidates[58,59]. The calculated band structure of silicene on MoS_2 is shown in Fig. 1.12. Due to the semiconducting character of MoS_2, the Dirac cone structure remains in the band structure.

Although there still exist problems to overcome, silicene is fervently investigated because of their advantages compared to graphene. Silicene would be compatible to the current silicon technology and Si has the strong spin-orbit interaction compared to carbon. The latter character is favorable for the realization of spintronic devices and for the observation of spin-related physical phenomena. In the next section, we will describe briefly the spin-related phenomena in relation to the so-called edge state of honeycomb material.

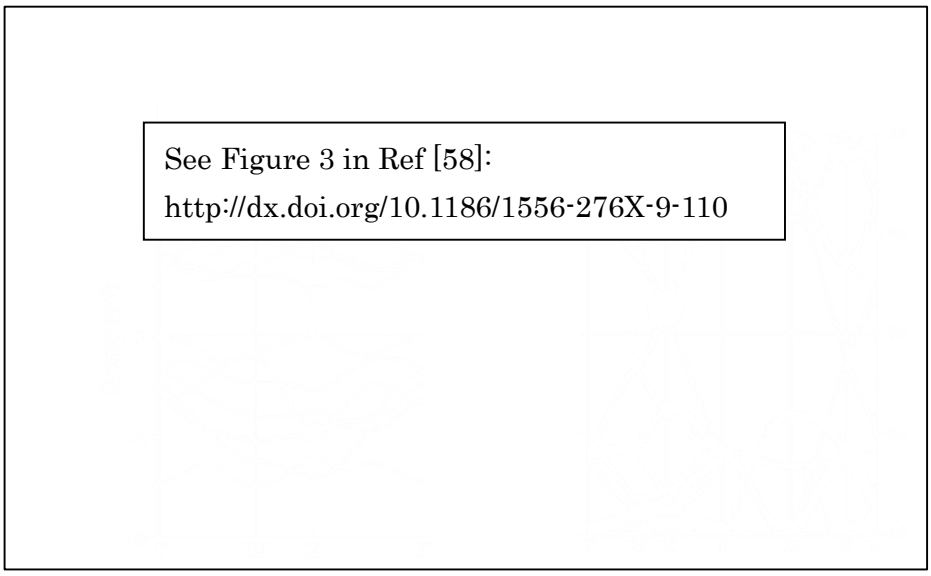

Fig. 1.12. Calculated band structure of (a) monolayer MoS_2 and (b) silicene on MoS_2. The band gap opens for the monolayer MoS_2. The Dirac cone is highlighted by the red circle in (b). Figures (a) and (b) are adopted from Figures 2(f) and 3(e) in Ref. [58], respectively, and redrawn for clearance.

1.4.2 Edge State

A finite sample has edges, not excepting the honeycomb materials. Figure. 1.13(a) shows the two stable edge structures of the honeycomb lattice. There are two type edges; the armchair edge and the zigzag edge. Theoretical tight binding calculations predicted that there are "peculiar" electronic states localized at the zigzag edge[60,61]. Hereafter, we focus on the nano graphene (not silicene) if not otherwise specified. Note that these theories and expected physical properties can hold true for other honeycomb materials such as silicene, in the same way of the Dirac electron system. Figure 1.13(b) and (c) show the model structures of one-dimensional honeycomb ribbons with the armchair and zigzag edge and Figure 1.13(d) and (e) show the calculated band structure. The zigzag edge honeycomb ribbon shows a flat band at around $k = \pi$ and at E_F, which is called the

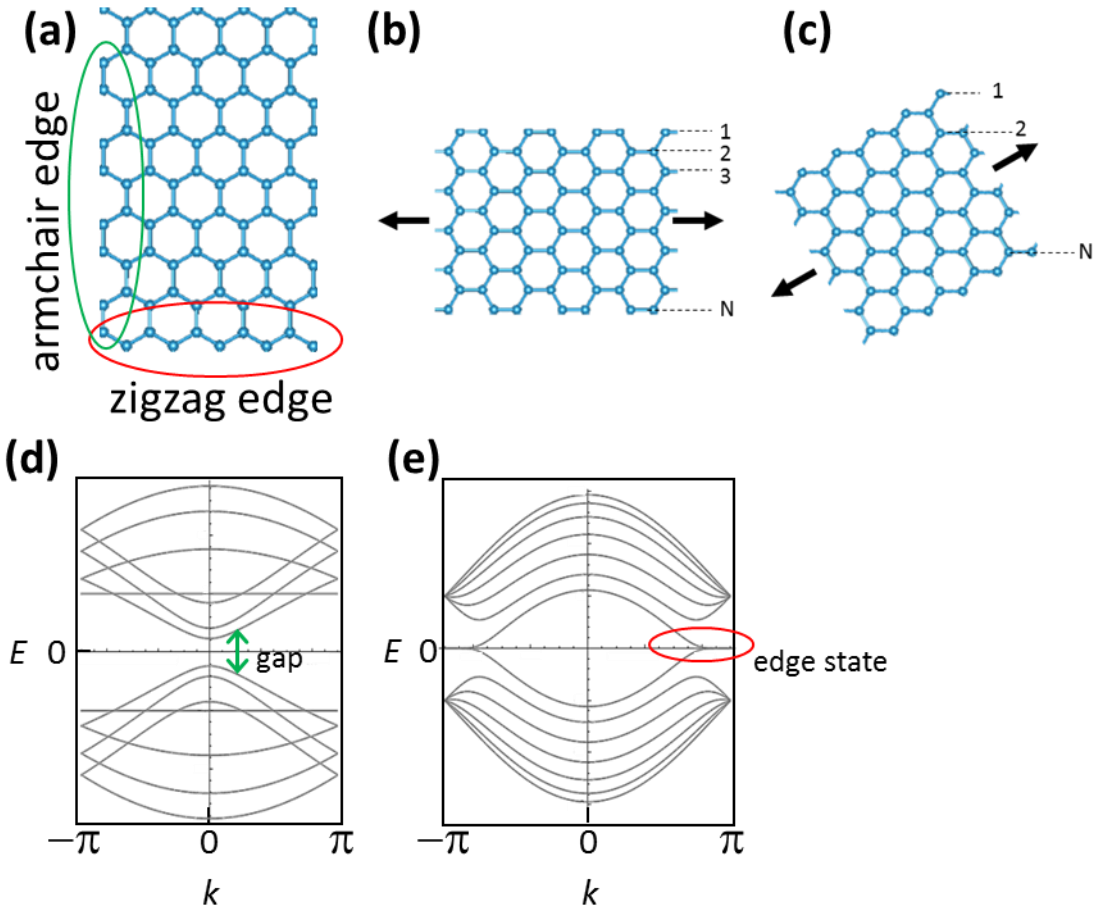

Fig. 1.13. (a) Two edge structures: armchair and zigzag edge. (b),(c) Honeycomb nano ribbon of the armchair and zigzag edge. Arrows indicate the longitudinal directions. (d) Calculated band structure of the armchair ribbon. The width of the ribbon is N = 7 [N is presented in (b)]. (e) Calculated band structure of the zigzag ribbon. The width of the ribbon is N = 7 [presented in (c)].

edge state. The edge state produces a sharp peak in the DOS[Fig. 1.14(b)]. Meanwhile, such structure does not appear for the armchair ribbon. The edge state is spatially localized along the zigzag edge, as shown in Fig. 1.14(a) and energetically locates in between the conduction and valence bands. The edge state is a bound state, like the Shockley state. In the chemical terms, the edge state is a non-bonding state, not bonding and anti-bonding state. In addition, it was pointed out that the spin polarization can take place at the edge as shown in Fig. 1.15. One edge shows spin-up magnetization and the other edge shows spin-down[60]. The origin of the ferrimagnetic ordering is

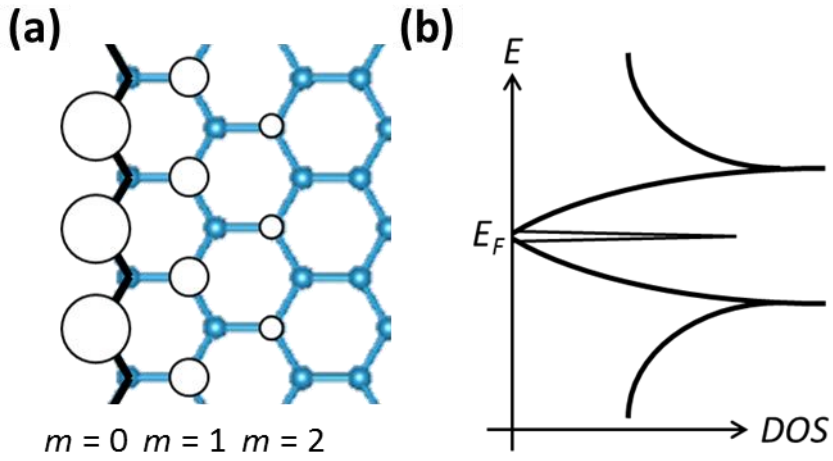

Fig. 1.14. (a) Spatial distribution of the edge state. The amplitude of the wave function is represented as white circles, decaying from the edge (m = 0) to the inner side (m = 2). The radius indicates the magnitudes. (b) Schematic DOS of the zigzag ribbon.

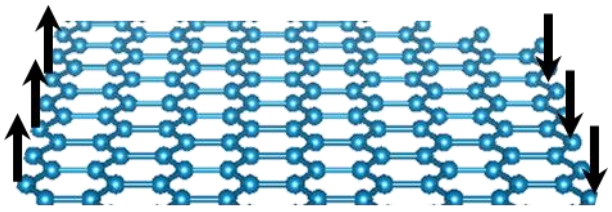

Fig. 1.15. Magnetization of the edge in the zigzag nano ribbon.

explained as follows; generally, electron system with a sharp peak appearing in the DOS is not stable. It is expected that electron system reduces the total energy via the lattice distortion or the magnetic polarization. Since the edge state has the non-bonding character, the lattice distortion around the edge is less likely to occur via the electron-phonon coupling in graphene[62]. Hence, at a certain condition, the electron-electron interaction produces the magnetic ordering.

Not only the Dirac electron system but also the edge state is intensively investigated. There are both fundamental and applicative reasons. In the scientific point of view, it is widely recognized that localized electronic states at the edge are important: for example, the edge state in the quantum Hall effect[63-65]. The edge state is inseparable from the physical phenomena of the series of the quantum Hall effect, i.e., the quantum anomalous Hall effect[43], the fractional quantum Hall effect[66] and the quantum spin Hall effect[48,67,68]. The edge state is also essential in the topological insulator[69,70] and topological superconductor[70,71], which have recently been attracting much interest in condensed matter physics. In these fields, the concepts of the topology and bulk-edge correspondence are important to consider the origin of the edge state and the physical phenomena. In the simplest term, the bulk-edge correspondence indicates that the topology and symmetry of the bulk determines the character of the edge state. In the honeycomb materials like graphene, it is explained that the chiral symmetry is essential for the Dirac electron system and the edge state[67,70,72]. Furthermore, when considering the spin-related phenomena, the time reversal symmetry and spin-orbit

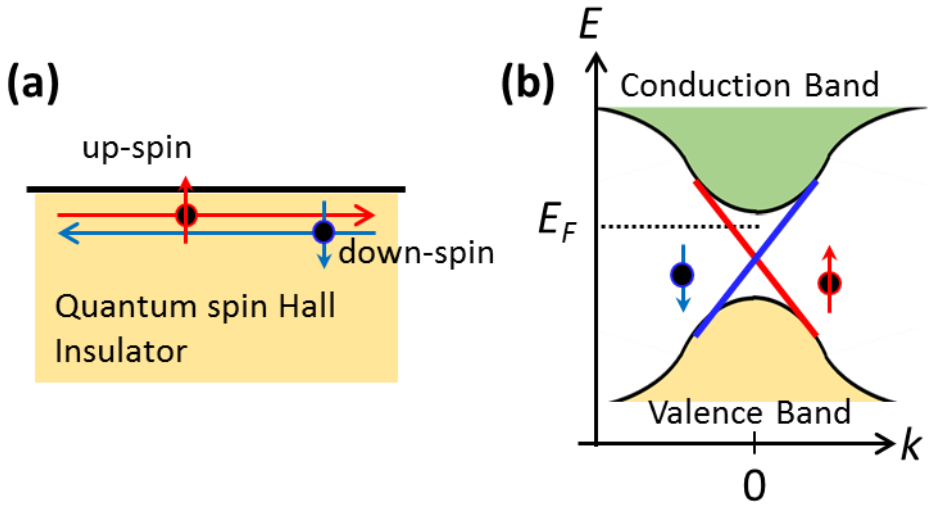

Fig. 1.16. (a) Topological edge state where up and down spins move in opposite directions (red and blue). (b) Schematic band structure of the topological edge state (red and blue).

interaction becomes important. In the theories on topological insulators, the time reversal symmetry and the spin-orbit interaction together with the bulk topology produces the so-called topological edge state, where the spin current flows along the edge and the quantum spin Hall effect occurs. Fig. 1.16 shows the typical feature of the topological edge state. The edge state shows the spin-dependent band structure. The edge state locates at the gap of the conduction and valence bands and connect the two bands. As mentioned in the previous section, Si has the stronger spin-orbit interaction compared to carbon. Hence, the 2D honeycomb lattice of Si, i.e., silicene has the potential to host the topological edge state[51,73-75].

In terms of the applications, there is another expected properties in the zigzag ribbon; the edge state provides a ballistic transport channel[49]. Figure 1.17 shows the closed-

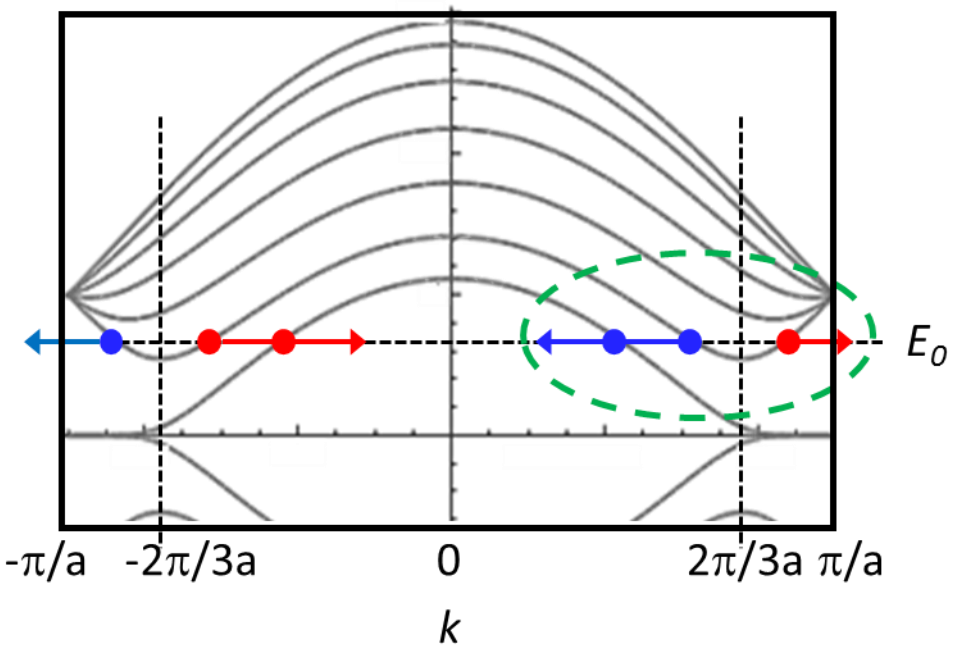

Fig. 1.17. Calculated band structure of the zigzag nano ribbon (N = 7) around the E_F. The horizontal dashed line is at the energy E_0. The vertical dashed lines correspond to the positions of the Dirac cone in graphene. The red (blue) color indicates the right (left) moving mode.

up band dispersion of the zigzag ribbon. At the energy E_0 around the E_F, there are two bands crossing the energy; the one is the edge state crossing the energy E_0 one time and the other is a conduction band crossing two times. As a whole, the total numbers of right and left moving modes are equal at this low energy region when considering the right and left valley, however, one excess left (right)-going mode exists around the right (left) valley, as shown in different colors. Suppose that the inter-valley scattering does not occurs or can be ignored, for example, there is no long range impurities potential, we can treat the right and left valley separately. It follows that the excess left (right)-going mode around the right (left) valley provides the perfect conduction channel because there is no final states for electrons of the excess mode to be scattered.

The edge state can be observable indirectly by measuring current flow across the sample such as the Hall bar. In contrast, direct observations of the edge state together with the spatial distributions of the edge state can be achieved by STM and STS. Several studies on the honeycomb materials of carbon report that the peak structure appears at the E_F in the spectra obtained at the edge, which is attributable to the edge state; HOPG[76], graphene nano ribbon (GNR) created by unzipping a carbon nano tube[77], and graphene synthesized on SiC substrate[78]. Figure 1.18 shows GNR on Au(111) and STS spectra obtained around the edge of GNR[77]. A sharp peak at around the E_F appears in the spectra obtained at the edge and the peak disappears as the position moves away from the edge. Meanwhile, there are no reports that the edge state of other honeycomb materials (Si, Ge, etc.) is experimentally observed both directly and indirectly.

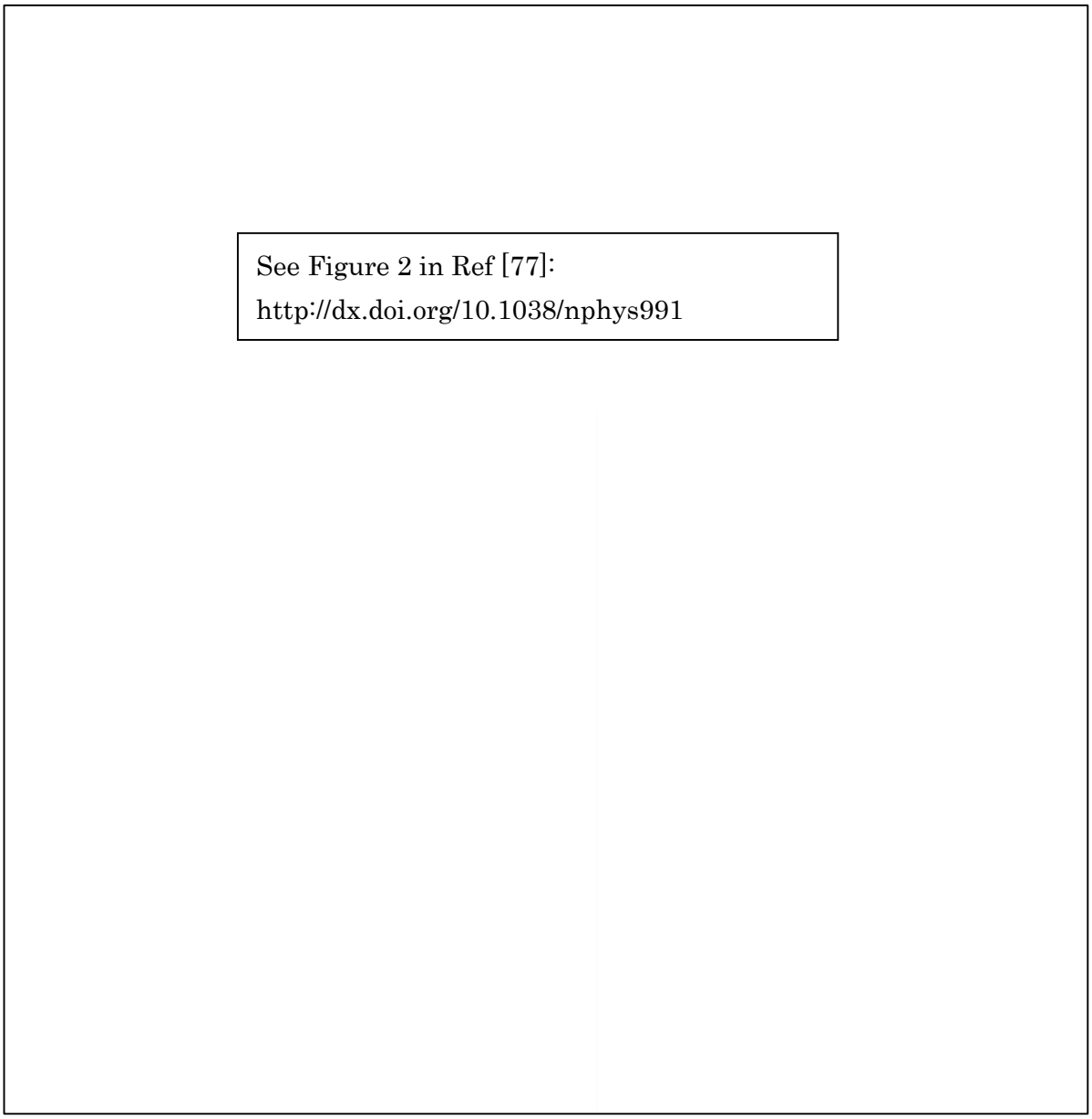

Fig. 1.18. (a) STM image of graphene nano ribbon on Au(111). (b) Structure model of the ribbon. (c) STS spectra obtained at positions along the black circles in (a). A sharp peak appears at the E_F which corresponds to the edge state (highlighted by the red circle). (Figures are adopted from Ref. [77]).

1.4.3 Purpose of the study; Silicene Nano Ribbon

Let us briefly summarize the background introduced above. The 2D honeycomb materials are intensively investigated because they provide us with the chances to both investigate the fascinating quantum physics and realize the future applications. Not only the Dirac electron system but also the edge state is one of the interesting characters in the honeycomb materials. Characterization of the electronic properties at the edge is essential in the study of honeycomb materials. In this respect, the honeycomb nano ribbon is a good sample to observe the edge properties. In addition, the nano ribbon could be an important component to achieve the future nano electronic device.

Silicene, a 2D honeycomb material made of Si, has the potential to be beyond graphene, which is the most intensively studied material; the honeycomb structure with the stronger spin-orbit interaction could realize the topological edge state and the quantum spin Hall effect. In addition, Silicene is compatible to the current semiconductor technology.

Therefore, investigating the electronic properties (especially at the edge) of silicene nano ribbon (SiNR) has a big impact on the further studies on silicene and honeycomb materials. We have one problem to overcome; according to the studies on silicene, the Ag substrate breaks the unique electronic properties of silicene. The reason is explained by the interaction between the Si and Ag substrate; the hybridization of the electronic states of Si and Ag leads the unique properties in silicene to vanish. The vanishment of the unique electronic properties is also expected in SiNR on Ag(110).

Here we propose one solution by the STM contact measurement. STM tip can selectively contact to the single SiNR on the Ag(110) substrate and then lift up the SiNR from the substrate. The interaction between Si and Ag can be reduced in this way.

Figure 1.19 shows the schematic image of the contact measurement, which was performed to the graphene nano ribbon on Au(111)[79]. We can obtain the *I-V* spectra when the STM tip lifts up SiNR. If the interaction is successfully reduced and the edge revives, the *I-V* spectra is expected to contain the character of the edge state, which has the sharp peak at the E_F in the DOS.

In this thesis, we report the results of STM contact measurements on SiNR on Ag(110). STS spectra obtained on the edge of SiNR shows no peak structure at around the E_F, which is attributable to the edge state. We have constructed the single SiNR junction and lifted up the SiNR. In the *dI/dV* spectra obtained when the STM tip lifted the SiNR, a sharp peak appears at the E_F, which is attributable to the edge state.

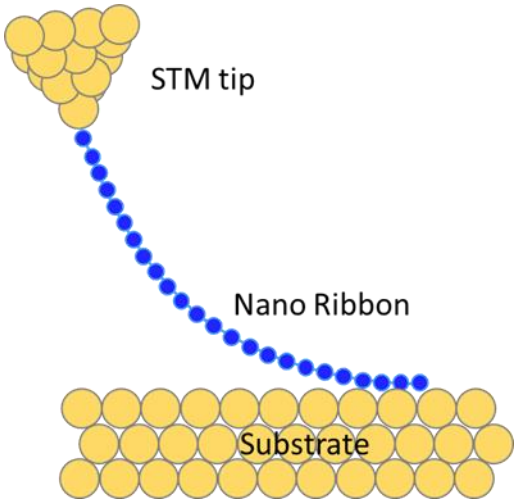

Fig. 1.19. Schematic picture of STM contact measurement, where the STM tip lifts up the ribbon.

1.5 Kondo Effect in Single Molecule

1.5.1 Kondo Effect

Kondo effect, which is a many-body effect and relates to the magnetic (spin) phenomena, is one of the attracting topics. It is because the many-body effect, i.e., the electron correlation is essential in various fields of the condensed matter physics such as the Mott insulators, the heavy Fermion system, high-temperature superconductivity and so on.

Historically, the Kondo effect was observed as an unusual behavior of the electrical resistance in some paramagnetic metals[80] in 1920s~1930s. Figure 1.20 shows an example: the temperature dependence of the resistance in Au wires. At very low

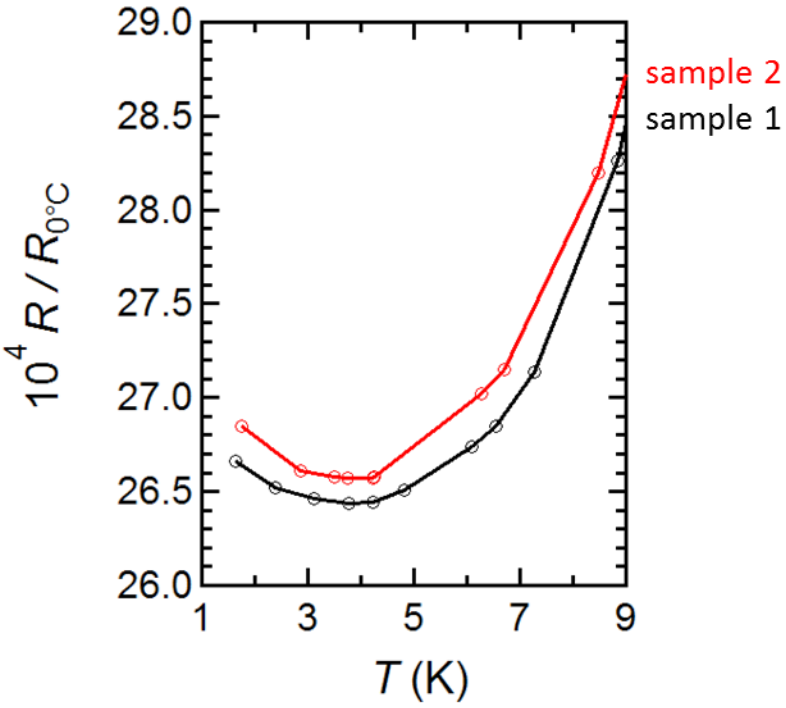

Fig. 1.20. Electric resistance of gold wires (two samples) between T = 1 and 9 K. Data points are obtained from Tables 1 and 2 in Ref. [80]. The vertical axis is presented as the normalized resistance (normalized at the resistance at 0 ^{o}C).

temperature, the resistance have the minimal point and increase as the temperature decreases. This minimal of the resistance cannot be explained by the conventional formulation known as Matthiessen law; in the ordinal metals, the resistance mainly arises from the scattering of electrons by phonons. The temperature dependence of the resistance is described as $R = R_{imp} + \alpha T^5$, where α is a factor and R_{imp} is the residual resistance at zero temperature arising from impurity scattering.

Further researches revealed that magnetic impurities in paramagnetic metals are responsible for this unusual behavior of the resistance. This phenomenon, Kondo effect, is theoretically explained by J. Kondo in 1964[81]. We briefly explain the mechanism below. Consider a nonmagnetic host metal with a magnetic impurity. The conduction electrons of a host metal are scattered at a magnetic impurity site, as schematically illustrated in Fig. 1.21(a). In the scattering process, the spin of the impurity site is flipped. This is the s-d exchange interaction. The Hamiltonian of this s-d exchange model is expressed as follows:

$$H = \sum_{k,\sigma} \varepsilon_k c^{\dagger}_{k\sigma} c_{k\sigma} - \frac{J_{ex}}{2N} \sum_{k,k',\sigma,\sigma'} c^{\dagger}_{k'\sigma'} \, \boldsymbol{\sigma}_{\sigma\sigma'} \, c_{k\sigma} \, S \,, \tag{1.11}$$

where k and k' are the wave number of the conduction electrons, σ and σ' represent the up and down spins, ε_k is the energy of the conduction electrons with the wave number k and spin σ, $c_{k\sigma}^{\dagger}$ and $c_{k\sigma}$ are the creation and annihilation operator of the conduction electrons, J_{ex} is the exchange coupling parameter, N is the number of atoms per volume of the host metal, $\boldsymbol{\sigma}$ is the Pauli's matrices and S is the spin of the impurity site. J_{ex} is expressed as

$$J_{ex} = \frac{\Delta}{\pi \rho} \left(\left| \frac{1}{\varepsilon_i} \right| + \left| \frac{1}{\varepsilon_i + U} \right| \right), \tag{1.12}$$

where, ρ is the DOS of the host metal at the E_F, the U is the on-sight Coulomb repulsion between the spin-up and spin-down state of the impurity site, Δ is the broadening of the

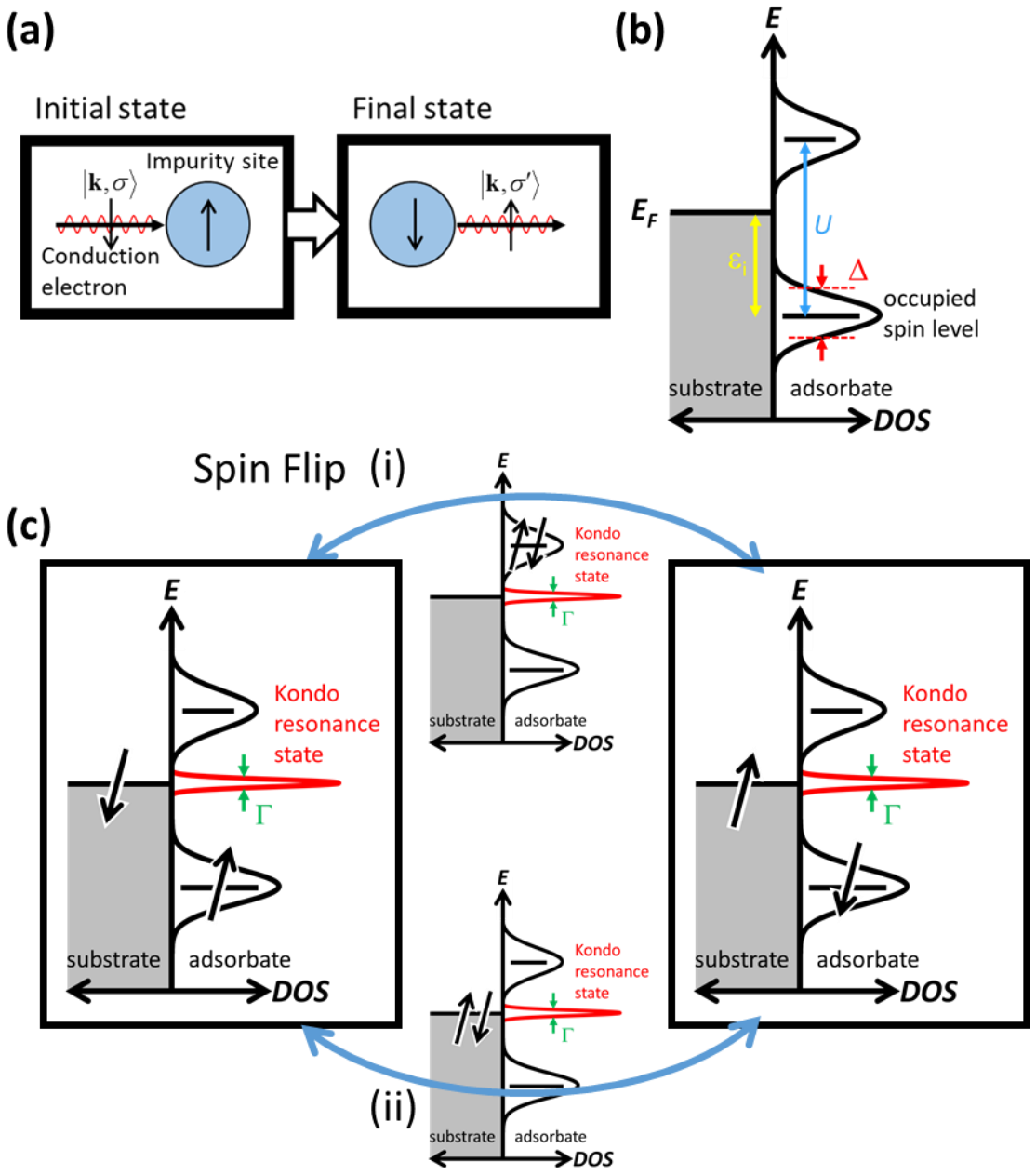

Fig. 1.21. (a) Schematic image of the spin flip scattering occurring in the Kondo effect. The blue circles represent the impurity sites and the waves with arrows represent the conduction electrons. (b) Energy diagram of the host metal (substrate) and magnetic impurity (adsorbate). (c) Schematic image of the two spin flip processes in the Kondo effect.

occupied impurity state and ε_i is the energy difference of the occupied spin state of the impurity site from the E_F[82].

The first term of the Hamiltonian represents the energy of the conduction electrons and the second term represents the s-d exchange interaction. The continuous spin flipping produces a many-body ground state called Kondo resonance state at around the E_F [Fig. 1.21(c)]. The Kondo resonance state is a non-magnetic singlet state (so-called Kondo singlet)[83], where the spin of the impurity site coupled with the many conduction electrons of the host metal. Since the singlet state is formed, the Kondo effect can be described as the screening phenomenon of the local spin (often referred to as the Kondo screening).

The formation energy of the Kondo resonance state is represented as the Kondo temperature T_K; when the temperature of the system decreases below T_K, the Kondo resonance state is formed against the thermal energy. The Kondo temperature is given by the half-width at half maximum (HWHM) Γ of the Kondo resonance state at the zero temperature[82]:

$$T_K = \Gamma / k_B , \tag{1.13}$$

where k_B is the Boltzmann constant. Γ has the relation to the parameters of the system as below:

$$\Gamma \approx \sqrt{2\Delta \frac{U}{\pi}} \exp\left[-\frac{\pi}{2\Delta} J_{ex}^{-1} \right]. \tag{1.14}$$

At finite temperature T, Γ is given in the form;

$$\Gamma = \sqrt{(\alpha k_B T)^2 + (2 k_B T_K)^2} , \tag{1.15}$$

where α is a constant[82,84].

1.5.2 Kondo Effect in Single Adsorbate

The developments of STM and low-temperature techniques have enabled us to investigate the single magnetic adsorbate on the metal substrate; magnetic atoms such as Ti, Ce, Co, [84-86] and magnetic metal-organic complexes such as metal phthalocyanines and porphyrins[87]. The spectroscopic observations of the single adsorbate by STM and STS have contributed greatly to the understandings of the Kondo effect. As well as the advantage in single adsorbate characterization, STM manipulation technique provides us the method to control local conditions of the magnetic adsorbates via the adsorption site control. Owing to these advantages, STM and STS measurements have been performed to investigate various character of the Kondo effect; the effect of the adsorption site difference[88,89], the magnetic anisotropy[90,91], the interactions between more than one magnetic adsorbate such as 2D molecular assembly[87,92].

In the STS spectra, the Kondo resonance state is observed as the Fano resonance shape[93,94]. The Fano resonance arises from the interference of two tunneling paths, schematically illustrated in Fig. 1.22; one is the tunneling via the Kondo resonance state (channel 1) and the other is the direct tunneling through the metal substrate (channel 2). The Fano function is described as;

$$f_{Fano}(E) = \frac{(\varepsilon + q)^2}{1+\varepsilon^2}, \qquad \varepsilon = \frac{E-\varepsilon_0}{\Gamma_F} \tag{1.16}$$

where q is the Fano parameter, which determines the asymmetricity, ε_0 is the energy of the resonance and Γ_F is the half width of the Fano resonance, which have the relation to the original width of the Kondo resonance state $\Gamma = \Gamma_F / 2$. Figure 1.23 shows the spectral shape as a function of q.

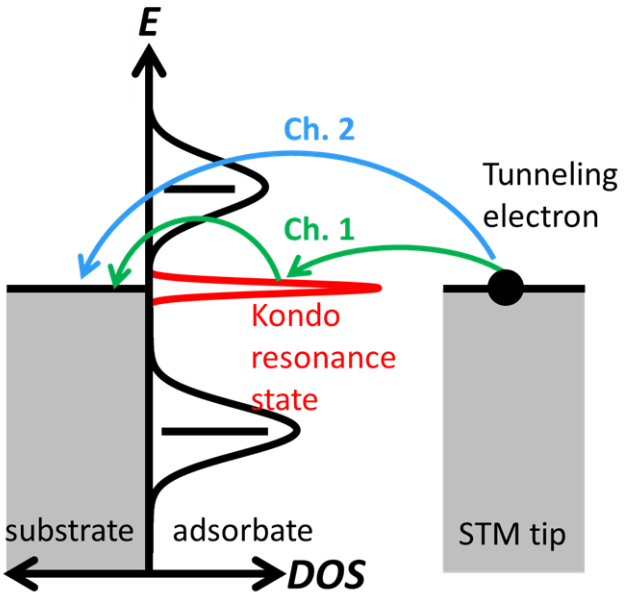

Fig. 1.22. Schematic picture of the electron tunneling from the STM tip. The spin of the tunneling electrons in the process 1 and 2 are identical in the final states.

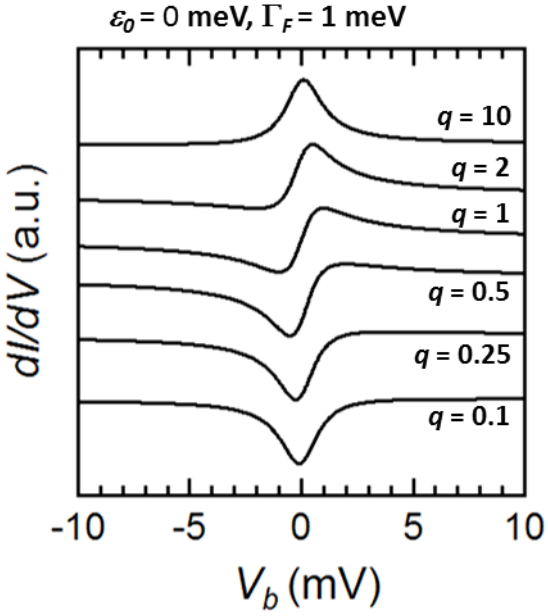

Fig. 1.23. Fano functions with different q parameters, described in the form of STS spectra. The resonance width (HWHM) Γ_F is set to 1 meV and the position of the resonance ε_0 is set to 0 meV.

As the absolute value of q decreases down to zero, the line shape of the Fano function comes to a symmetric dip structure, while it comes to a symmetric peak structure as $|q|$ increases. The dip structure (small $|q|$) indicates that the direct tunneling process is dominant, while the peak structure (large $|q|$) indicates that the tunneling process via the Kondo resonance state is dominant.

Experimentally, most compelling evidence of the Kondo resonance state is showing the temperature dependence of Γ_F (and Γ) as described in Eq. (1.15). The quenching of the Fano resonance shape by the applied magnetic fields is also the basic character of the Kondo resonance. It is because the magnetic field breaks the energetic degeneracy of the up and down spin states, which suppresses the spin flip scattering process and stabilizes the one spin, resulting in the suppression of the Kondo effect. Note that when the Kondo resonance state has a high T_K, characterization of the single adsorbate by STM and STS measurements come to be difficult because we need the high temperature and high magnetic field to observe the spectral changes, i.e., both thermal energy and magnetic field cannot perturb the Kondo resonance state.

1.5.3 Two-stage Kondo Effect

When there is a single spin (S= 1/2) at the impurity site, whether the Kondo resonance state is formed or not depends on the electronic structure (and resulting interactions) of the impurity and the host metals. In contrast, when there is a multiple spin (S> 1/2) at the impurity site, the situation becomes complicated. Let us suppose a spin S= 1 (Fig. 1.24). Two spins are in different orbitals of the impurity site (for example, different d-orbitals). Generally, the different orbitals hybridize with the conduction band of the host

metal with different strength. Consequently, different Kondo temperatures exist for different spins ($T_{K1} > T_{K2}$) and the spins are screened in a stepwise way as the temperature decreases. This is the two-stage Kondo effect. When T_{K2} is lower than the experimental temperature T and T_{K1} is higher than T, the one spin is screened and the other spin remains unscreened.

Then let us introduce the Hund's rule coupling. Since Hund coupling stabilizes the spins (ferromagnetically or antiferromagnetically), the Kondo effect, where the spin is screened via the continuous spin flipping, competes with the Hund coupling. According to the theoretical studies, the Hund coupling suppresses the Kondo screening. In the case of the spin $S = 1$, both Kondo temperatures (T_{K1}, T_{K2}) are suppressed as the strength of the Hund coupling increases[95].

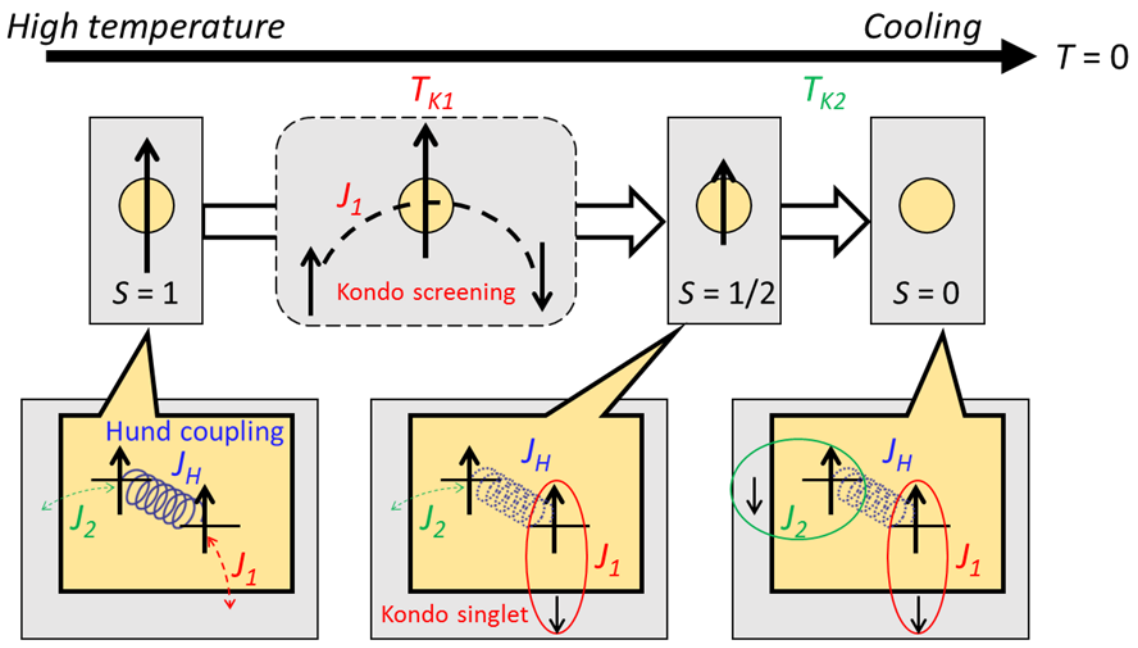

Fig. 1.24. Schematic illustration of the multi-stage Kondo effect (the spin $S = 1$ case). The host metal is drawn as the gray color and the magnetic impurity as the orange color. The $S = 1$ spin is screened in a stepwise manner.

1.5.4 Competition of Kondo Effect and Spin-orbit Coupling

The spin-orbit coupling (SOC) (or the spin-orbit interaction: SOI) is an essential interaction in the magnetic phenomenon. The SOC is the interaction between the orbital magnetic moment and the spin, which is described as the simple Hamiltonian:

$$H_{SO} = \lambda \mathbf{L}\mathbf{S}. \tag{1.17}$$

Here, λ is the SOC constant, $\mathbf{L}$ is the angular momentum operator and $\mathbf{S}$ is the spin operator. The SOC lifts up the spin degeneracy in a similar way of the external magnetic field. Hence, the SOC as well as the Hund coupling competes with the Kondo effect.

Recently, several examples on this competition have been demonstrated: for example, 3d magnetic adatoms on Cu_2N substrate[90]. In order to introduce the recent studies below, we introduce the effective spin Hamiltonian, which contains the SOC and the Zeeman effect[96]:

$$H_{spin} = H_{SO} + H_{Zeeman} = \lambda \mathbf{L}\mathbf{S} + \mu_B(\mathbf{L} + g_e\mathbf{S})\mathbf{H}, \tag{1.18}$$

where $\mathbf{H}$ is the magnetic fields (B_x, B_y, B_z), g_e is the Landé factor (approximately equal to 2) and μ_B is the Bohr magneton. We take the quantization axis along the z-direction. When the orbital degeneracy is lifted, the orbital magnetic moment can be ignored; it is known that S is a good quantum number in describing magnetic properties of 3d metals and we do not use $J = L + S$ in these cases. Under this condition, we obtain the spin anisotropy Hamiltonian from the second-order perturbation treatment:

$$H_{aniso} = DS_z^{\,2} + E\left(S_x^{\,2} - S_y^{\,2}\right) + g\mu_B \mathbf{H}\mathbf{S}, \tag{1.19}$$

where D is the axial anisotropy parameter, E is the transverse anisotropy parameter, $S_{x,y,z}$ are the magnetic moment of each axis. In this model, the z-axis is selected where $|D|$ is maximized and x,y-axes are determined for E to be positive ($E > 0$).

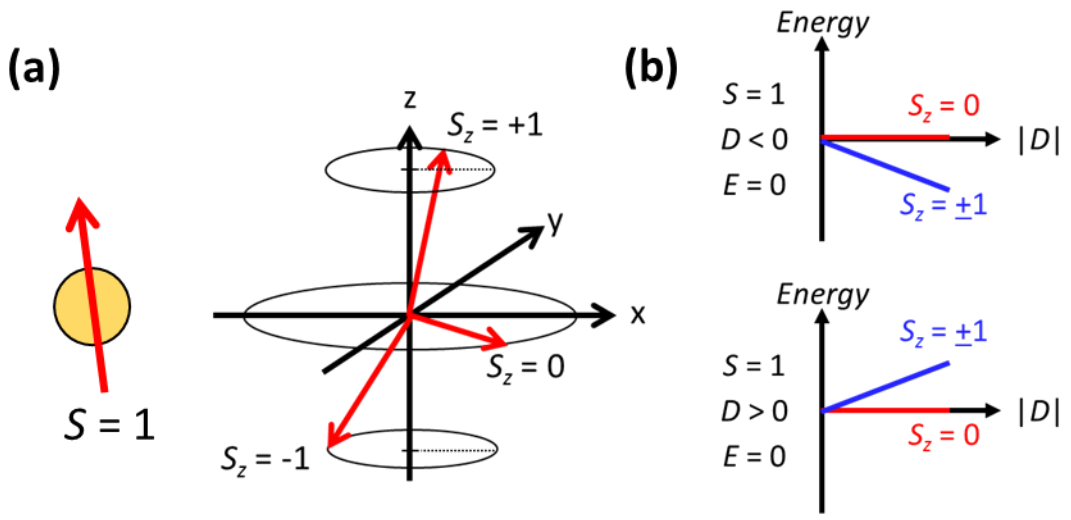

Fig. 1.25. (a) Schematic picture of the degenerated states in the $S = 1$ spin (S_z = +1, 0, -1). (b) Energy diagram of the spin states under the magnetic anisotropy. The vertical axis represents the energy and the horizontal axis represents the absolute value of the axial anisotropy parameter D. The transverse anisotropy parameter E is zero in this figure.

Figure 1.25 shows the schematic illustration of a magnetic atom and the energy diagram of $S = 1$ spin. Here we assume that $E = 0$. When $D > 0$, the energy is stable when the magnetic moment directs to the in-plane direction. In this case, the z-axis is called hard-axis and the anisotropy is called the easy-plane anisotropy. The spin state $S_z = 0$ is the ground state and $S_z = \pm 1$ are the excited states. Meanwhile, in the $D < 0$ case, the magnetic moment directs to the z-axis. In this case, the z-axis is easy-axis and the anisotropy is the easy-axis anisotropy. The energy diagram is opposite to the hard-axis ($D > 0$) case.

The magnetic anisotropy has crucial influence on the Kondo effect[97]. Due to the selection rules, direct transition between $S_z = \pm 1$ states is prohibited. In the easy-axis anisotropy case ($D < 0$), the transition between $S_z = \pm 1$ occurs via the excited $S_z = 0$ state. This energy diagram suppresses the Kondo effect, in the same way of the magnetic fields, schematically illustrated Fig. 1.26. In contrast, spin flip process occurs without the energy excitation process in the easy-plane anisotropy case ($D > 0$).

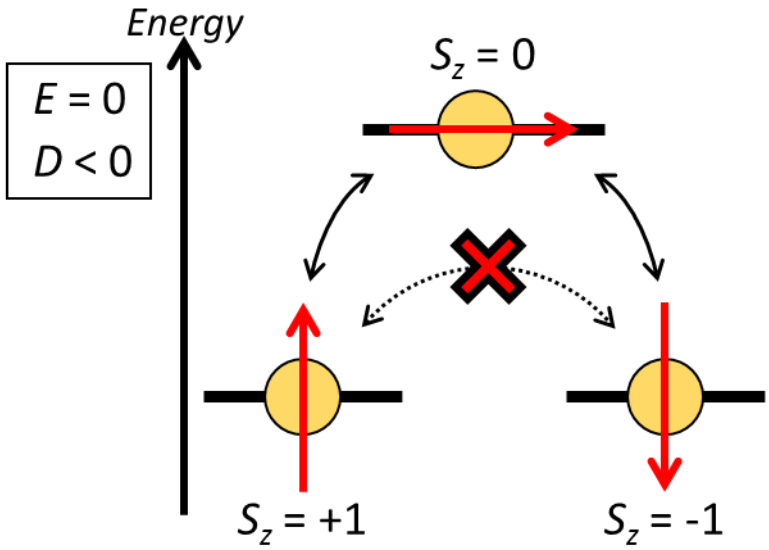

Fig. 1.26. Energy diagram of spin $S = 1$ with $D < 0$ and $E = 0$. The ground states $S_z = \pm 1$ are degenerated under the zero magnetic field. The spin flip process of the Kondo effect cannot take place at the low temperature, where the thermal energy prohibits the transition via the excited $S_z = 0$ state.

$$H_{Kondo} = -\frac{J_{ex}}{2N} \sum_{k,k',\sigma,\sigma'} c^{\dagger}_{k'\sigma'} \boldsymbol{\sigma}_{\sigma\sigma'} c_{k\sigma} \mathbf{S}$$

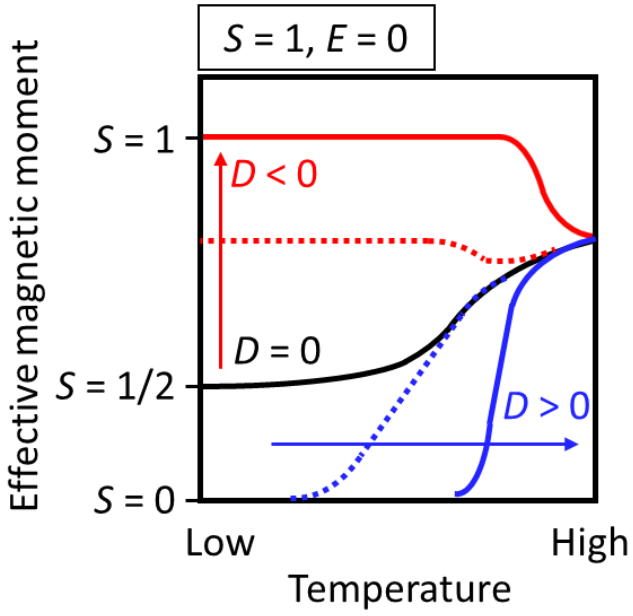

Fig. 1.27. Schematic image of the effective magnetic moment (vertical axis) as a function of temperature (horizontal axis) with different magnetic anisotropy (see Ref. [97]). When $D > 0$, the spin $S = 1$ is screened as the temperature decreases (blue lines). While the magnetic moment remains at very low temperature when $D < 0$ (red lines). The black solid line indicates the isotropic case ($D = 0$).

Figure 1.27 schematically shows the effect of the anisotropy on the Kondo effect under the simple Kondo Hamiltonian[97]. The horizontal axis is the temperature and the vertical axis represents the effective magnetic moment. The magnetic moment remains at the very low temperature in the easy-axis anisotropy case ($D < 0$), while the magnetic moment is perfectly screened in the easy-plane anisotropy case ($D > 0$). The solid black line in the Fig. 1.27 is the result of $D = 0$ (isotropic magnetism). Note that this model does not consider the spin $S = 1$ as being consisted of two spins in two different orbitals. Hence, the two-stage Kondo effect is not taken into account and the magnetic moment remains at the low temperature in the isotropic case.

The effect of the magnetic anisotropy on the Kondo effect has been experimentally observed in several systems[90,98]. Fe ($S = 2$) and Mn ($S = 5/2$) atoms on a single layer film of Cu_2N on Cu(100) show no Kondo effect, which have the easy-axis magnetic anisotropy[98]. In contrast, Co on Cu_2N/Cu(100) shows the Kondo effect[90]. Figure 1.28 shows STS spectra of single Co atoms on Cu_2N/Cu(100). In the STS spectra, a sharp peak appears at the E_F and a symmetric step structure with respect to the E_F is observed. The peak structure is assigned to the Fano resonance of the Kondo resonance state and the symmetric step structure is an inelastic excitation process (magnetic excitation). The spin state of the Co atom is $S = 3/2$ and the magnetic anisotropy is $D > 0$ (easy-plane) with the quantization axis (z-axis) perpendicular to the nitrogen low (named as the hollow direction in the paper), schematically shown in Fig. 1.29(a) and Fig. 1.30. The magnetic anisotropy produces the magnetic excitation process between $S_z = 1/2$ (-1/2) and 3/2 (-3/2), observed as the symmetric step structure. The positive D sets $S_z = \pm 1/2$ states as the ground states, which are degenerated under the zero magnetic field and hence allow the effective Kondo screening [Figs. 1.29(b),(c) and Fig. 1.30(c)].

When the magnetic field is applied along the z-axis (named as $B_{//hollow}$), large Zeeman shifts occurs both between $S_z = \pm 1/2$ and $S_z = \pm 3/2$ states, as shown in Fig. 1.29(b) and Fig. 1.30(d). Meanwhile when the magnetic field is applied perpendicularly to the *z*-axis along the nitrogen low (named as $B_{//nitrogen}$), the Zeeman shifts appear in a different way shown in Figs. 1.29(c) and Fig. 1.30(e). The splitting of $S_z = \pm 1/2$ states causes the suppression and splitting of the Kondo resonance peak [Figs. 1.29(d),(e)]. The splitting of the Kondo resonance peak and the step position of the inelastic magnetic are well explained in the model above, as shown in Fig. 1.30.

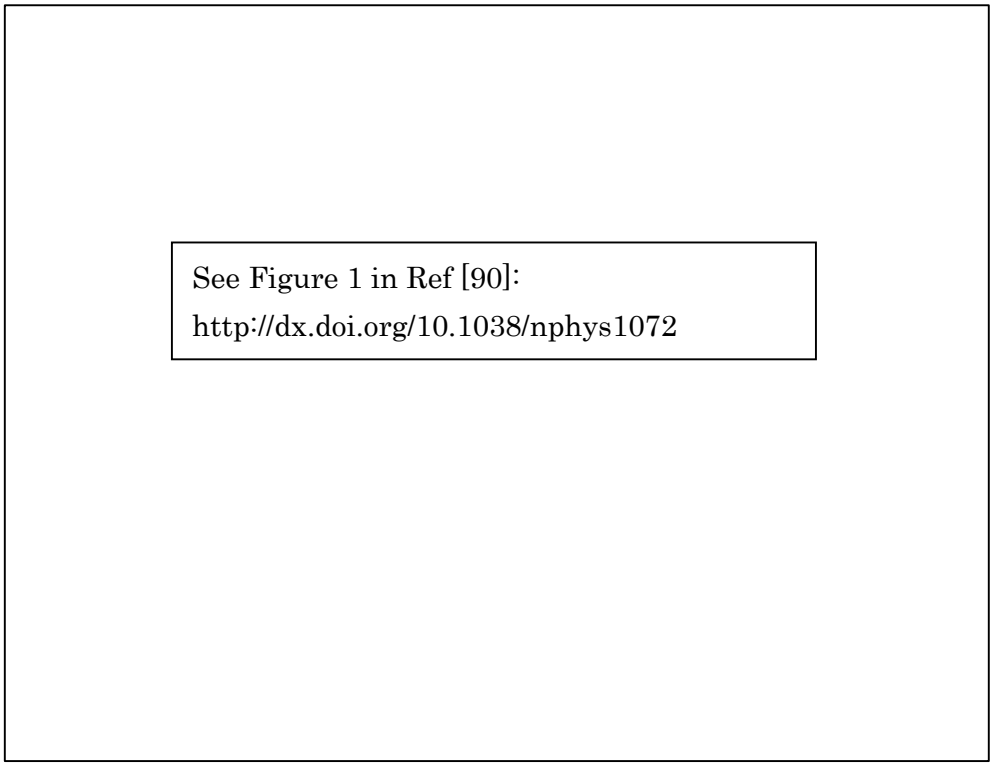

Fig. 1.28. STS spectra obtained at the Co atom. The peaks at the E_F fitted by the red curves are the signature of the Kondo resonance state. A symmetric step structure is also observed at $V = \pm 5$ mV. (Figures are adopted from Ref. [90]).

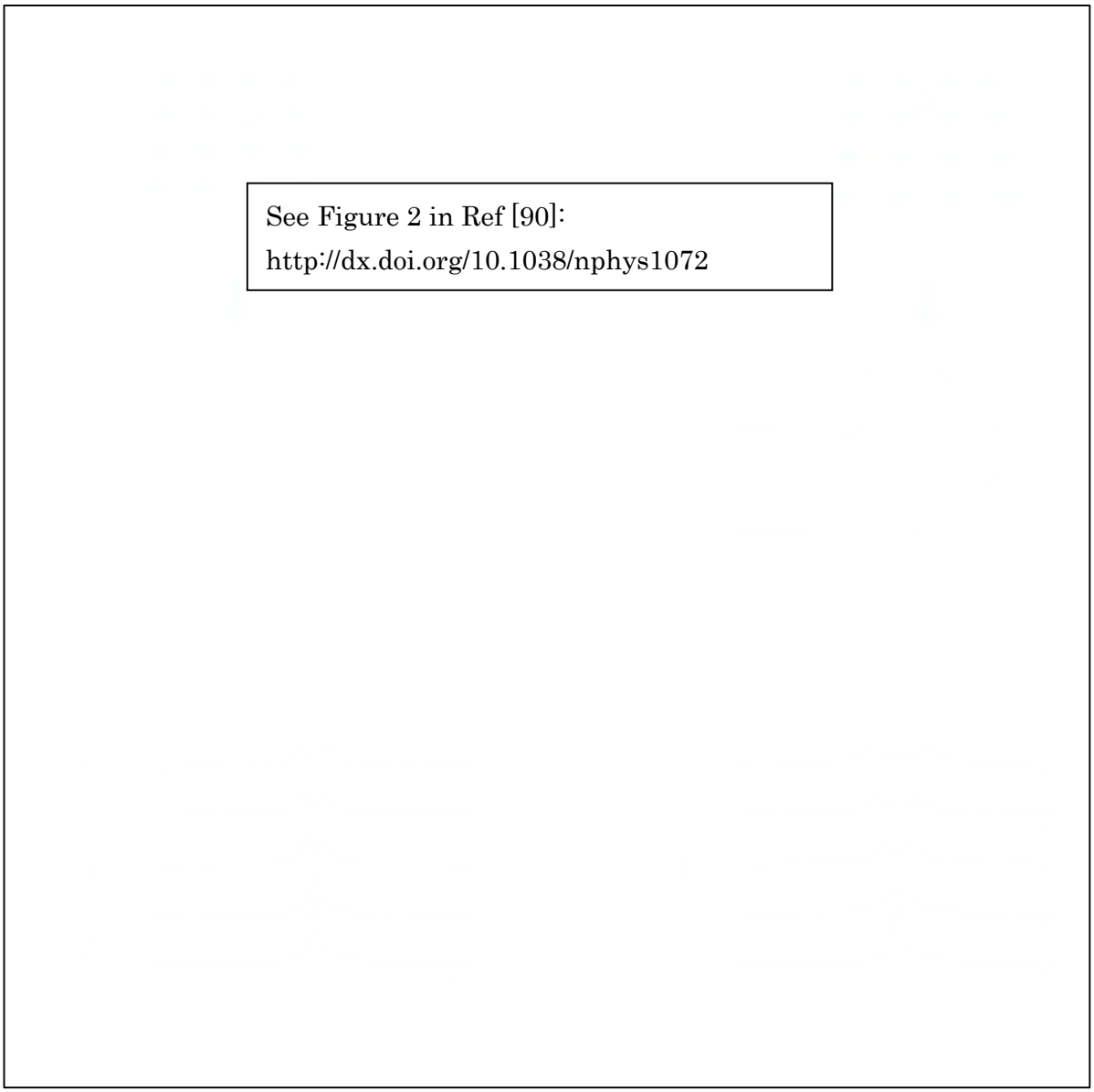

Fig. 1.29. (a) STM image and schematic model structure of Co atom on Cu_2N. The direction of the applied magnetic field is shown as black arrows below the model structures. The Co atoms in the left and right side figure are in a different symmetry under the magnetic field. (b),(c) Spectral evolution under the magnetic field. The orange curves represent the calculated spectra of the IETS signals. (d),(e) STS spectra which show the contributions from the Kondo resonance, i.e., obtained by subtracting the orange spectra from the black (experimental result) spectra in (b) and (c). (Figures are adopted from Ref. [90]).

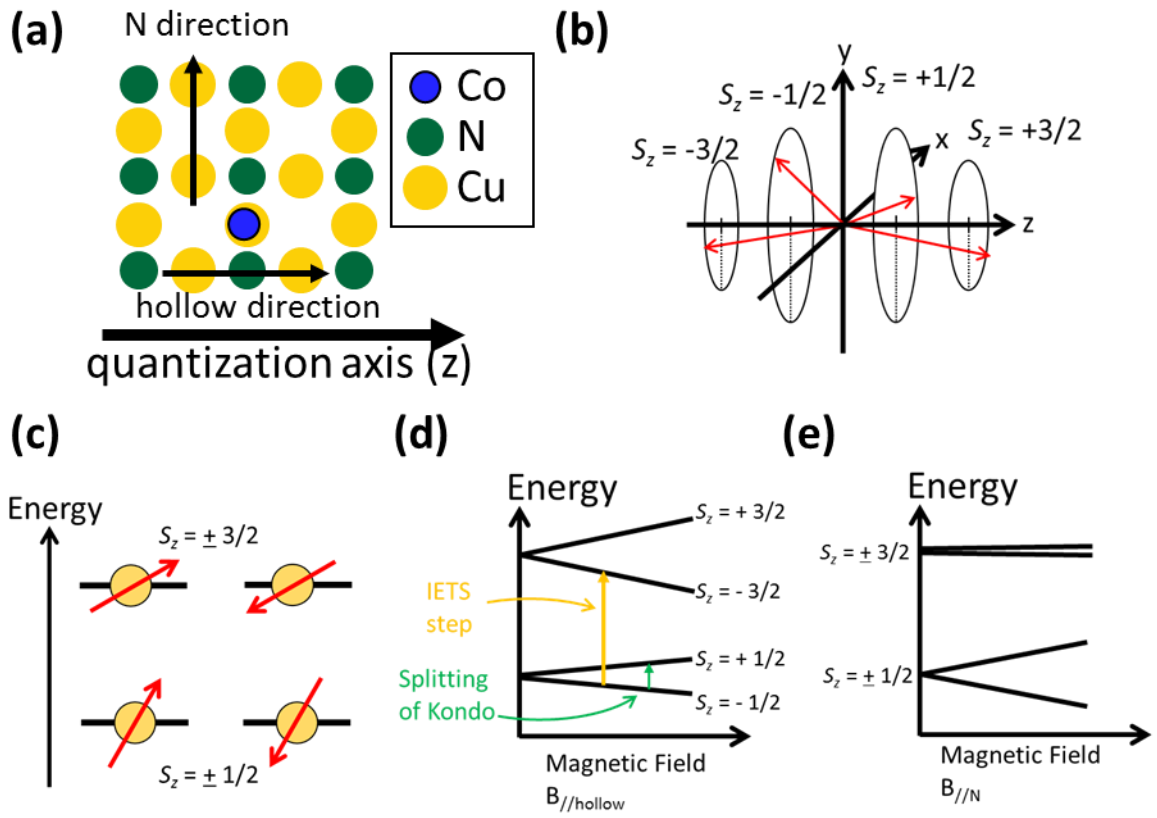

Fig. 1.30. (a) Schematic model of the system: Co on Cu_2N/Cu(100). The quantization axis is the hollow direction according to Ref. 90. (b) Schematic image of the spin S = 3/2 in this system. (c) Energy diagram of S = 3/2 spin under D > 0. (d) Magnetic field dependence of the spin states. The magnetic field is applied to the hollow direction. (e) Magnetic field dependence of the spin states. The magnetic field is applied to the N direction.

They also observed Ti atoms on the same substrate and found the Kondo resonance in Ti atoms. Although the Kondo resonance is observed, anisotropic behavior is not observed in the Ti atoms, in contrast to Co. They conclude that such behavior is because the spin state of Ti is expected to be S= 1/2, where the anisotropic character will not appear.

These results clearly show that the magnetic anisotropy plays a decisive role in the appearance and the behavior against the magnetic field of the Kondo effect.

1.5.5 Purpose of the study: FePc on Au(111)

In the examples explained above (Fe, Mn, Co, Ti/Cu_2N), the Kondo effect is not observed in Fe and Mn due to the SOC (magnetic anisotropy). While, the Kondo effect is observed in the magnetic impurities which have the non-integer spin (Co: S = 3/2 and Ti: S = 1/2), where the degeneracy of the ground state still remains depending on the energy alignment of the spin state under the SOC. The competitions between the Kondo effect and the SOC (magnetic anisotropy) and the Hund coupling in the integer spin system are not still explored yet.

Iron(II)-phthalocyanine (FePc) on Au(111) is an ideal test system to investigate such competitions. Figure 1.31 shows the STM image of FePc on Au(111) and STS spectra obtained at the Fe site. Each four-leaf clover shape represents the single FePc molecule. At present, several important properties of FePc on Au(111) has been revealed; the spin state of Fe is expected to S = 1[99]. The experimental results together with the theoretical investigations revealed that the two-stage Kondo effect appears in the FePc molecules adsorbed at the on-top site in the low-temperature measurements (T = 0.4 K)[89,92]. The Kondo temperatures are evaluated as T_{K1} ~ 150 K and T_{K2} = 2.6 K. In contrast, the FePc molecules adsorbed at the bridge site show one Kondo resonance T_K ~ 200 K in the measurements at T = 0.4 K. This difference is explained by the local symmetry around the Fe site. The local symmetry of FePc at the on-top is the fourfold symmetry while FePc at the bridge site is twofold. This result indicates that the Kondo resonance states of FePc on Au(111) is a result of the competitions, i.e., competing couplings coexist so that the Kondo resonance states are vulnerable to the external perturbation, such as the local symmetry.

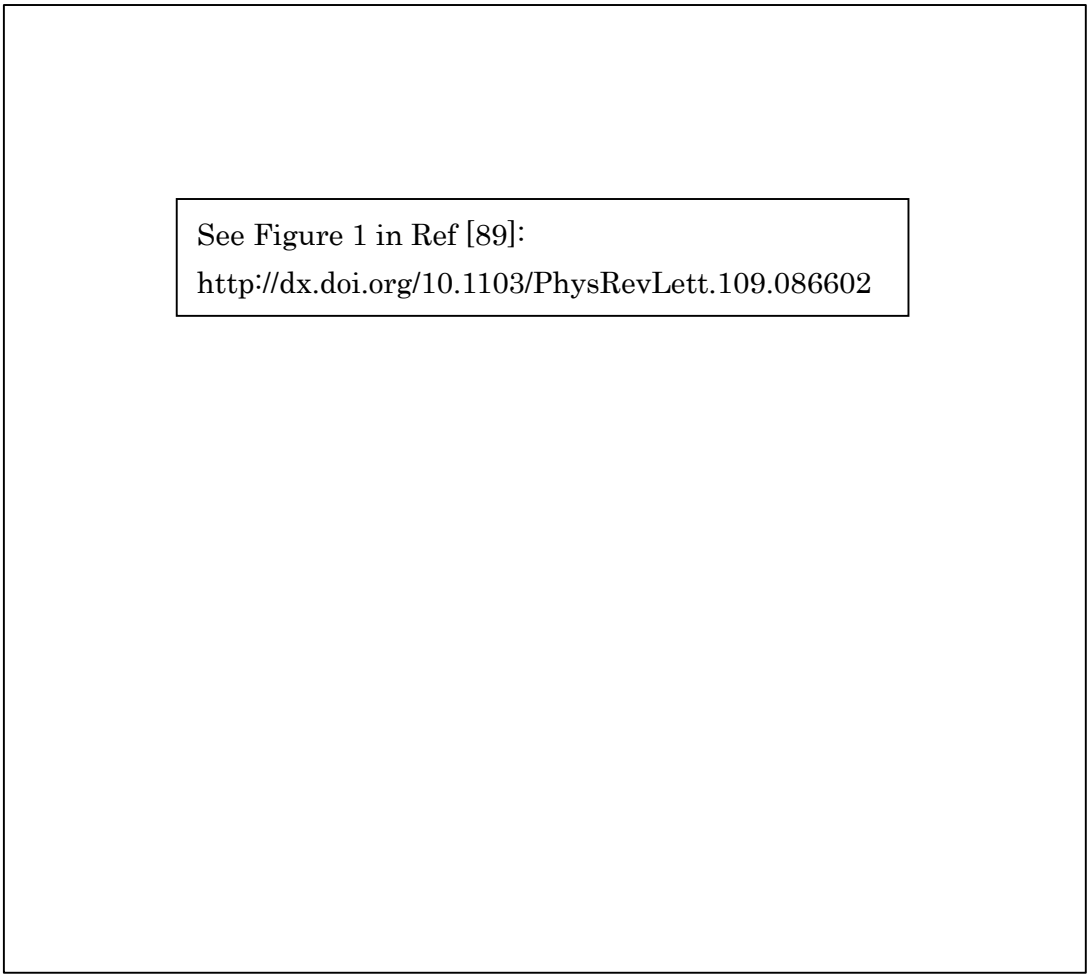

Fig. 1.31. (a) STM image of FePc on Au(111). Characters "o" and "b" represent the adsorption site: on-top and bridge. (b) STS spectra (wide range). In the spectra of the on-top FePc, broad peak and narrow dip structures are observed. (c) Close-up spectra of the on-top FePc. The red solid curve represents the fitting of the two Fano functions (green and blue). (Figures are adopted from Ref. [89]). Reprinted with permission from [E. Minamitani, N. Tsukahara, D. Matsunaka, Y. Kim, N. Takagi, and M. Kawai, Physical Review Letters **109,** 086602 (2012)]. Copyright (2012) by the American Physical Society.

Let us briefly summarize the background of the study. The Kondo effect in a single magnetic atom/molecule on a surface is one of the attracting topics in condensed matter physics. Further experimental investigations on the Kondo effect of a multiple spin system and the competitions between the Kondo effect and the SOC and Hund coupling are required for the better understanding of the Kondo effect. The two-stage Kondo effect in the single magnetic molecule was experimentally observed in FePc/Au(111), whose spin state is the integer spin $S = 1$. It is worth trying to apply external perturbations to the Kondo resonance states and observing the change of the Kondo resonance states. At present, the spectral evolutions under applying magnetic fields and increasing the temperature were already measured, and the dissipation of the second Kondo resonance state ($T_{K2} = 2.6$ K) was clearly observed[89]. However, it is obvious that breaking the first Kondo resonance state ($T_{K1} \sim 150$ K) by the magnetic fields and temperature is difficult simultaneously measuring STS spectra.

We have applied the STM contact measurement to this system. The STM tip can induce a perturbation to the Kondo effect via modifying the interaction of the electronic states of the adsorbate. Figure 1.32 schematically shows the STM contact measurement on Co/Cu(111)[100]. As the STM tip comes close to a Co atom, the Kondo temperature increases due to the additional interaction between the electronic states of the STM tip and Co. In this system, the Co atom on Cu(111) has the $S = 1/2$ spin, where the anisotropy does not affect the Kondo effect. According to theoretical calculations, the change of the Kondo temperature is explained by the shift of DOS of Co 3d states.

Although the STM tip may make the system totally different from the original states (such as the spin S changes into $S \pm 1/2$), we can obtain further insights into the Kondo effect of the system if the perturbation by the STM tip does not change the system totally. In this thesis, we report the results of STM contact measurements on FePc/Au(111).

Spectral evolutions as a function of the STM tip-Fe distance clearly show the transition of the ground states. When the STM tip contact to the Fe, STS spectra show the symmetric step structure with respect to the E_F, which indicates an inelastic excitation process.

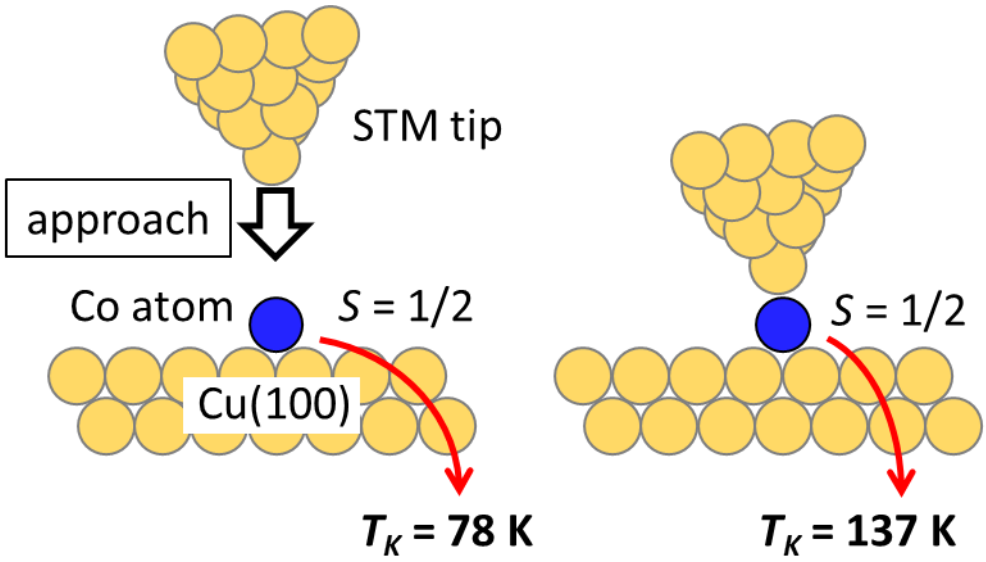

Fig. 1.32. Schematic images of the STM contact measurement on the Co atom on Cu(100). The left and right images represent when the STM tip is far from the Co atom and when the STM tip contacts the Co atom. According to the *dI/dV* spectra of the junction, the Kondo temperatures of both configurations are obtained as 78 and 137 K, respectively (these values are obtained from Ref. [100]).

References

[1] G. Binnig, H. Rohrer, Ch. Gerber, and E. Weibel, "Tunneling through a controllable vacuum gap", Appl. Phys. Lett. **40,** 178 (1982).

[2] G. Binnig, H. Rohrer, Ch. Gerber, and E. Weibel, "Surfae Studies by Scanning Tunneling Microscopy", Phys. Rev. Lett. **49**, 57 (1982).

[3] J. A. Stroscio, R. M. Feenstra, and A. P. Fein, "Electronic Structure of the Si(111)2 x I Surface by Scanning Tunneling Microscopy", Phys. Rev. Lett. **57**, 5 (1986).

[4] R. M. Feenstra, J. A. Stroscio, and A. P. Fein, "Tunneling Spectroscopy of the Si(111)2 x 1 Surface", Surface Science **181,** 295 (1987).

[5] N. Holonyak Jr., I. A. Lesk, R. N. Hall, J. J. Tiemann, and H. Ehrenreich, "Direct Observation of Phonons During Tunneling in Narrow Junction Diodes", Phys. Rev. Lett. **3**, 167 (1959).

[6] J. Lambe, and R. C. Jaklevic, "Molecular Vibration Spectra by Inelastic Electron Tunneling", Phys. Rev. **165,** 821 (1968).

[7] B. C. Stipe, M. A. Rezaei, and W. Ho, "Single-Molecule Vibrational Spectroscopy and Microscopy", Science **280,** 1732 (1998).

[8] B. C. Stipe, M. A. Rezaei, and W. Ho, "Coupling of Vibrational Excitation to the Rotational Motion of a Single Adsorbed Molecule", Phys. Rev. Lett. **81,** 1263 (1998).

[9] D. M. Eigler, and E. K. Scheweizer, "Positioning single atoms with a scanning tunneling microscope", Nature, **344**, 524 (1990).

[10] M. F. Crommie, C. P. Lutz, D. M. Eigler, and E. J. Heller, "Waves on a Metal Surface and Quantum Corrals", Surface Review and Letters **2,** 127 (1995).

[11] Y. Kim, T. Komeda, and M. Kawai, “Single-Molecule Reaction and Characterization by Vibrational Excitation”, Phys. Rev. Lett. **89,** 126104 (2002).

[12] S. Katano, Y. Kim, M. Hori, M. Trenary, and M. Kawai “Reversible control of hydrogenation of a single molecule”, Science **316,** 1883 (2007).

[13] C. -J. Xia, D. -S. Liu, C. -F. Fang, and P. Zhao “The I-V characteristics of the butadienimine-based optical molecular switch: An ab initio study”, Physica E **42,** 1763 (2010).

[14] Y. Y. Liang, F. Jiang, Y. X. Zhou, H. Chena, R. Note, H. Mizuseki, and Y. Kawazoe, “Ab initio study of single-molecule rotation switch based on nonequilibrium Green's function theory” The Journal of Chemical Physics **127,** 084107 (2007).

[15] L. Bogani, and W. Wernsdorfer, “Molecular spintronics using single-molecule magnets”, Nature Materials **7,** 179 (2008).

[16] H. Hao, X. H. Zheng, Z. X. Dai, and Z. Zeng, “Spin-filtering transport and switching effect of MnCu single-molecule magnet”, Appl. Phys. Lett. **96,** 192112 (2010).

[17] A. Aviram, and M. A. Ratner, “Molecular Rectifiers”, Chem. Phys. Lett. **29,** 277 (1974).

[18] L. B. Coleman, M. J. Cohen, D. J. Sandman, F. G. Yamagishi, A. F. Garito, and A. J. Heeger, “Superconducting fluctuations and the peierls instability in an organic solid”, Solid State Communications **12,** 1125 (1973).

[19] R. Landauer, “Spatial Variation of Currents and Fields Due to Localized Scatterers in Metallic Conduction”, IBM Journal of Research and Development **1,** 223 (1957).

[20] R. Landauer, “Conductance determined by transmission: probes and quantized constriction resistance”, J. Phys.: Condens. Matter **1,** 8099 (1989).

[21] Y. Imry, and R. Landauer, “Conductance viewed as transmission”, Reviews of Modern Physics **71,** S306 (1999).

[22] B. J. van Wees, H. van Houten, C. W. J. Beenakker, J. G. Williamson, L. P. Kouwenhoven, D. van der Marel, and C. T. Foxon, “Quantized conductance of point contacts in a two-dimensional electron gas”, Phys. Rev. Lett. **60,** 848 (1988).

[23] C. J. Muller, J. M. van Ruitenbeek, and L. J. de Jongh; “Experimental observation of the transition from weak link to tunnel junction”, Physica C **191,** 485 (1992).

[24] A. Nitzan, and M. A. Ratner, “Electron Transport in Molecular Wire Junctions”, Science **300,** 1384 (2003).

[25] C. J. Muller, B. J. Vleeming, M. A. Reed, J. J. S. Lamba, R. Hara, L. Jones, and J. M. Tour; “Atomic probes: a search for conduction through a single molecule”, Nanotechnology **7,** 409 (1996).

[26] M. A. Reed, C. Zhou, C. J. Muller, T. P. Burgin, and J. M. Tour; “Conductance of a Molecular Junction”, Science **278,** 252 (1997).

[27] T. Nishino, and P. T. Bui, “Direct electrical single-molecule detection of DNA through electron transfer induced by hybridization” Chem. Commun. **49,** 3437 (2013).

[28] M. Kiguchi, and S. Kaneko, “Electron transport through single π-conjugated molecules bridging between metal electrodes”, Chem. Phys. Chem. **13,** 1116 (2012).

[29] E. Lörtscher, B. Gotsmann, Y. Lee, L. Yu, C. Rettner, and H. Riel, “Transport Properties of a Single-Molecule Diode”, ACS Nano **6,** 4931 (2012).

[30] E. Scheer, P. Joyez, D. Esteve, C. Urbina, and M. H. Devoret, “Conduction Channel Transmissions of Atomic-Size Aluminum Contacts”, Phys. Rev. Lett. **78,** 3535 (1997).

[31] E. Scheer, N. Agrait, J. C. Cuevas, A. L. Yeyati, B. Ludoph, A. M. Rodero, G. R. Bollinger, J. M. van Ruitenbeek, and C. Urbina, "The signature of chemical valence in the electrical conduction through a single-atom contact", Nature **394,** 154 (1998).

[32] B. Ludoph, N. van der Post, E. N. Bratus, E. V. Bezuglyi, V. S. Shumeiko, G. Wendin, and J. M. van Ruitenbeek, "Multiple Andreev reflection in single-atom niobium junctions", Phys. Rev. B **61,** 8561 (2000).

[33] C. J. Muller, J. M. van Ruitenbeek, and L. J. de Jongh, "Conductance and supercurrent discontinuities in atomic-scale metallic constrictions of variable width", Phys. Rev. Lett. **69,** 140 (1992).

[34] D. Djukic, and J. M. van Ruitenbeek, "Shot noise measurements on a single molecule", Nano Letters **6,** 789 (2006).

[35] M. Kiguchi, O. Tal, S. Wohlthat, F. Pauly, M. Krieger, D. Djukic, J. C. Cuevas, and J. M. van Ruitenbeek, "Highly Conductive Molecular Junctions Based on Direct Binding of Benzene to Platinum Electrodes", Phys. Rev. Lett. **101,** 046801 (2008).

[36] O. Tal, M. Krieger, B. Leerink, and J. M. van Ruitenbeek, "Electron-Vibration Interaction in Single-Molecule Junctions: From Contact to Tunneling Regimes", Phys. Rev. Lett. **100,** 196804 (2008).

[37] E. N. Bratus, V. S. Shumeiko, and G. Wendin, "Theory of Subharmonic Gap Structure in Superconducting Mesoscopic Tunnel Contacts", Phys. Rev. Lett. **74,** 2110 (1995).

[38] J. J. Riquelme, L. de la Vega, A. Levy Yeyati, N. Agraït, A. Martin-Rodero, and G. Rubio-Bollinger, "Distribution of conduction channels in nanoscale contacts: Evolution towards the diffusive limit", Europhys. Lett. **70,** 663 (2005).

[39] A. Yu. Kasumov, K. Tsukagoshi, M. Kawamura, T. Kobayashi, Y. Aoyagi, K. Senba, T. Kodama, H. Nishikawa, I. Ikemoto, K. Kikuchi, V. T. Volkov, Yu. A. Kasumov, R. Deblock, S. Guéron, and H. Bouchiat, "Proximity effect in a superconductor-metallofullerene-superconductor molecular junction", Phys. Rev. B **72,** 033414 (2005).

[40] H. W. Kroto, J. R. Heath, S. C. O'Brien, R. F. Curl, and R. E. Smalley, "C_{60}: Buckminsterfullerene", Nature **318,** 162 (1985).

[41] S. Iijima, "Helical microtubules of graphitic carbon", Nature **354,** 56 (1991).

[42] K. S. Novoselov, A. K. Geim, S. V. Morozov, D. Jiang, Y. Zhang, S. V. Dubonos, I. V. Grigorieva, and A. A. Firsov, "Electric field effect in atomically thin carbon films", Science **306,** 666 (2004).

[43] K. S. Novoselov, A. K. Geim, S. V. Morozov, D. Jiang, M. I. Katsnelson, I. V. Grigorieva, S. V. Dubonos, and A. A. Firsov, "Two-dimensional gas of massless Dirac fermions in graphene", Nature **438,** 197 (2005).

[44] K. F. Mak, M. Y. Sfeir, Y. Wu, C. H. Lui, J. A. Misewich, and T. F. Heinz, "Measurement of the Optical Conductivity of Graphene", Phys. Rev. Lett. **101,** 196405 (2008).

[45] C. Lee, X. Wei, J. W. Kysar, and J. Hone, "Measurement of the Elastic Properties and Intrinsic Strength of Monolayer Graphene", Science **321,** 385 (2008).

[46] T. J. Booth, P. Blake, R. R. Nair, D. Jiang,E. W. Hill, U. Bangert, A. Bleloch, M. Gass, K. S. Novoselov, M. I. Katsnelson, and A. K. Geim, "Macroscopic Graphene Membranes and Their Extraordinary Stiffness", Nano Lett. **8,** 2442 (2008).

[47] L. L. Zhang, R. Zhou, and X. S. Zhao, "Graphene-based materials as supercapacitor electrodes", J. Mater. Chem. **20,** 5983 (2010).

[48] J. Balakrishnan, G. K. W. Koon, M. Jaiswal, A. H. Castro Neto, and B. Özyilmaz, "Colossal enhancement of spin–orbit coupling in weakly hydrogenated graphene", Nature Physics **9,** 284 (2013).

[49] K. Wakabayashi, Y. Takane, M. Yamamoto, and M. Sigrist, "Electronic transport properties of graphene nanoribbons", New Journal of Physics **11,** 095016 (2009).

[50] S. Cahangirov, M. Topsakal, E. Aktürk, H. Sahin, and S. Ciraci, "Two- and One-Dimensional Honeycomb Structures of Silicon and Germanium", Phys. Rev. Lett. **102,** 236804 (2009).

[51] C. -C. Liu, W.Feng, and Y. Yao, "Quantum Spin Hall Effect in Silicene and Two-Dimensional Germanium", Phys. Rev. Lett. **107,** 076802 (2011).

[52] R. Hoffmann, "Interaction of Orbitals through Space and through Bonds", Accounts of Chemical Research **4,** 1 (1971).

[53] C. Leandri, G. L. Lay, B. Aufray, C. Girardeaux, J. Avila, M. E. Dávila, M. C. Asensio, C. Ottaviani, and A. Cricenti, "Self-aligned silicon quantum wires on Ag(110)", Surface Science **574,** L9 (2005).

[54] B. Lalmi, H. Oughaddou, H. Enriquez, A. Kara, S. Vizzini, B. Ealet, and B. Aufray, "Epitaxial growth of a silicene sheet", Appl. Phys. Lett. **97,** 223109 (2010).

[55] C. Lin, R. Arafune, K. Kawahara, M. Kanno, N. Tsukahara, E. Minamitani, Y. Kim, M. Kawai, and N. Takagi, "Substrate-Induced Symmetry Breaking in Silicene", Phys. Rev. Lett. **110,** 076801 (2013).

[56] Z. -X. Guo, S. Furuya, J. Iwata, and A. Oshiyama, "Absence of Dirac Electrons in Silicene on Ag(111) Surfaces", J. Phys. Soc. Jpn **82,** 063714 (2013).

[57] Y. -P. Wang, and H. –P. Cheng, “Absence of a Dirac cone in silicene on Ag(111): First-principles density functional calculations with a modified effective band structure technique”, Phys. Rev. B **87,** 245430 (2013).

[58] X. Li, S. Wu, S. Zhou, and Z. Zhu, “Structural and electronic properties of germanene/MoS2 monolayer and silicene/MoS2 monolayer superlattices”, Nanoscale Research Letters **9,** 110 (2014).

[59] L. Li, X. Wang, X. Zhao, and M. Zhao, “Moiré superstructures of silicene on hexagonal boron nitride: A first-principles study”, Physics Letters A **377,** 2628 (2013).

[60] M. Fujita, K. Wakabayashi, K. Nakada, and K. Kusakabe, “Peculiar Localized State at Zigzag Graphite Edge”, J. Phys. Soc. Jpn. **65,** 1920 (1996).

[61] K. Nakada, M. Fujita, G. Dresselhaus, and M. S. Dresselhaus, “Edge state in graphene ribbons: Nanometer size effect and edge shape dependence”, Phys. Rev. B **54,** 17954 (1996)

[62] M. Fujita, M. Igami, and K. Nakada, “Lattice Distortion in Nanographite Ribbons”, J. Phys. Soc. Jpn. **66,** 1864 (1997).

[63] K. v. Klitzing, G. Dorda, and M. Pepper, “New method for High-Accuracy Determination of the Fine-Structure Constant Based on Quantized Hall Resistance”, Phys. Rev. Lett. 45, 494 (1980).

[64] R, B. Laughlin, “Quantized Hall conductivity in tqo dimensions”, Phys. Rev. B **23,** 5632 (1981).

[65] B. I. Halperin, "Quantized Hall conductance, current-carrying edge states, and the existence of extended states in a two-dimensional disordered potential", Phys. Rev. B **25,** 2185 (1982).

[66] D. C. Tsui, H. L. Stormer, and A. C. Gossard, "Two-Dimensional Magnetotransport in the Extreme Quantum Limit", Phys. Rev. Lett. **48,** 1559 (1982).

[67] C. L. Kane, and E. J. Mele, "Quantum Spin Hall Effect in Graphene", Phys. Rev. Lett. **95,** 226801 (2005).

[68] A. F. Young, J. D. Sanchez-Yamagishi, B.Hunt, S. H. Choi, K.Watanabe, T. Taniguchi, R. C. Ashoori, and P. Jarillo-Herrero, "Tunable symmetry breaking and helical edge transport in a graphene quantum spin Hall state", Nature **505,** 528 (2014).

[69] M. König, S. Wiedmann, C. Brüne, A. Roth, H. Buhmann, L. W. Molenkamp, X. –L. Qi, and S. –C. Zhang, "Quantum Spin Hall Insulator State in HgTe Quantum Wells", Science **318,** 766 (2007).

[70] M. Z. Hasan, and C. L. Kane, "Colloquium: Topological insulators", Rev. Mod. Phys. **82,** 3045 (2010).

[71] B. J. Lawson, G. Li, F. Yu, T. Asaba, C. Tinsman, T. Gao, W. Wang, Y. S. Hor, and Lu Li, "Quantum oscillations in $Cu_xBi_2Se_3$ in high magnetic fields", Phys. Rev. B **90,** 195141 (2014).

[72] Y. Hatsugai, "Chern Number and Edge States in the Integer Quantum Hall Effect", Phys. Rev. Lett. **71,** 3697 (1993).

[73] M. Ezawa, "Quantized conductance and field-effect topological quantum transistor in silicene nanoribbons", Appl. Phys. Lett. **102,** 172103 (2013).

[74] M. Ezawa, and N. Nagaosa, “Interference of topologically protected edge states in silicene nanoribbons”, Phys. Rev. B **88,** 121401 (2013).

[75] J. L. Lado, and J. Fernández-Rossier, “Magnetic Edge Anisotropy in Graphenelike Honeycomb Crystals”, Phys. Rev. Lett. **113,** 027203 (2014).

[76] Y. Niimi, T. Matsui, H. Kambara, K. Tagami, M. Tsukada, and H. Fukuyama, “Scanning tunneling microscopy and spectroscopy of the electronic local density of states of graphite surfaces near monoatomic step edges”, Phys. Rev. B **73,** 085421 (2006).

[77] C. Tao, L. Jiao, O. V. Yazyev, Y. -C. Chen, J. Feng, X. Zhang, R. B. Capaz, J. M. Tour, A. Zettl, S. G. Louie, H. Dai, and M. F. Crommie, “Spatially resolving edge states of chiral graphene nanoribbons”, Nature Physics **7,** 616 (2011).

[78] J. Baringhaus, F. Edler, and C. Tegenkamp, “Edge-states in graphene nanoribbons: a combined spectroscopy and transport Study”, J. Phys.: Condens. Matter **25,** 392001 (2013).

[79] M. Koch, F. Ample, C. Joachim, and L. Grill, “Voltage-dependent conductance of a single graphene nanoribbon”, Nature nanotechnology **7,** 713 (2012).

[80] W. J. de Haas, J. de Boer, and G. J. van den Berg, “The electrical resistance of gold, copper and lead at low temperatures”, Physica **1,** 1115 (1934).

[81] J. Kondo, “Resistance minimum in dilute magnetic alloys”, Progr. Theoret. Phys. **32,** 37 (1964).

[82] M. Ternes, A. J. Heinrich, and W. D. Schneider, “Spectroscopic manifestations of the Kondo effect on single adatoms”, J. Phys.: Condens. Matter **21,** 053001 (2009).

[83] K. Yosida, “Bound State Due to the s-d Exchange Interaction”, Phys. Rev. **147,** 223 (1966).

[84] K. Nagaoka, T. Jamneala, M. Grobis, and M. F. Crommie, “Temperature Dependence of a Single Kondo Impurity”, Phys. Rev. Lett. **88,** 077205 (2002).

[85] J. Li, W. D. Schneider, R. Berndt, and B. Delley, “Kondo Scattering Observed at a Single Magnetic Impurity”, Phys. Rev. Lett. **80,** 2894 (1998).

[86] V. Madhavan, W. Chen, T. Jamneala, M. F. Crommie, and N. S. Wingreen, “Tunneling into a Single Magnetic Atom: Spectroscopic Evidence of the Kondo Resonance”, Science **280,** 567 (1998).

[87] V. Iancu, A. Deshpande, and S. –W. Hla, “Manipulation of the Kondo Effect via Two-Dimensional Molecular Assembly”, Phys. Rev. Lett. **97,** 266603 (2006).

[88] L. Gao, W. Ji, Y. B. Hu, Z. H. Cheng, Z. T. Deng, Q. Liu, N. Jiang, X. Lin, W. Guo, S. X. Du, W. A. Hofer, X. C. Xie, and H. -J. Gao, “Site-Specific Kondo Effect at Ambient Temperatures in Iron-Based Molecules”, Phys. Rev. Lett. **99,** 106402 (2007).

[89] E. Minamitani, N. Tsukahara, D. Matsunaka, Y. Kim, N. Takagi, and M. Kawai, “Symmetry-Driven Novel Kondo Effect in a Molecule”, Phys. Rev. Lett. **109,** 086602 (2012).

[90] A. F. Otte, M. Ternes, K. von Bergmann, S. Loth, H. Brune, C. P. Lutz, C. F. Hirjibehedin, and A. J. Heinrich, “The role of magnetic anisotropy in the Kondo effect”, Nature Physics **4,** 847 (2008).

[91] J. C. Oberg, M. R. Calvo, F. Delgado, M. Moro-Lagares, D. Serrate, D. Jacob, J. Fernández-Rossier, and C. F. Hirjibehedin, "Control of single-spin magnetic anisotropy by exchange coupling", Nature Nanotechnology **9,** 64 (2014).

[92] N. Tsukahara, S. Shiraki, S. Itou, N. Ohta, N. Takagi, and M. Kawai, "Evolution of Kondo Resonance from a Single Impurity Molecule to the Two-Dimensional Lattice", Phys. Rev. Lett. **106,** 187201 (2011).

[93] U. Fano, "Effects of Configuration Interaction on Intensities and Phase Shifts", Phys. Rev. **124,** 1866 (1961).

[94] O. Újsághy, J. Kroha, L. Szunyogh, and A. Zawadowski, "Theory of the Fano Resonance in the STM Tunneling Density of States due to a Single Kondo Impurity", Phys. Rev. Lett. **85,** 2557 (2000).

[95] S. Yotsuhashi, H. Kusunose, and K. Miyake, "Orbital Dependence in Kondo Effect Enlarged by Hund's-Rule Coupling", J. Phys. Soc. Jpn. **70,** 186 (2001).

[96] M. H. L. Pryce, "A Modified Perturbation Procedure for a Problem in Paramagnetism", Proc. Phys. Soc. A **63,** 25 (1950).

[97] R. Žitko, R. Peters, and Th. Pruschke, "Properties of anisotropic magnetic impurities on surfaces", Phys. Rev. B **78,** 224404 (2008).

[98] C. F. Hirjibehedin, C. -Y. Lin, A. F. Otte, M. Ternes, C. P. Lutz, B. A. Jones, and A. J. Heinrich, "Large magnetic anisotropy of a single atomic spin embedded in a surface molecular network", Science **317,** 1199 (2007).

[99] S. Stepanow, P. S. Miedema, A. Mugarza, G. Ceballos, P. Moras, J. C. Cezar, C. Carbone, F. M. F. de Groot, and P. Gambardella, “Mixed-valence behavior and strong correlation effects of metal phthalocyanines adsorbed on metals”, Phys. Rev. B **83,** 220401 (2011).

[100] N. Néel, J. Kröger, L. Limot, K. Palotas, W. A. Hofer, and R. Berndt; “Conductance and Kondo Effect in a Controlled Single-Atom Contact”, Phys. Rev. Lett. **98,** 016801 (2007).

Chapter 2
Experimental Methods

In this chapter, we will describe the experimental methods; the principles of scanning tunneling microscope (STM) and scanning tunneling spectroscopy (STS) are introduced in sections 2.1 and 2.2. In section 2.3, we show the set-up of STM apparatus used in this study and the practical procedures of experiments.

2.1 Principle of Scanning Tunneling Microscope (STM)

2.1.1 Quantum Tunneling

Scanning tunneling microscope (STM) is a kind of probe microscopes and provides real-space observations of a surface with the atomic resolution. In the following sections, we explain the principle of STM.

STM is based on the quantum tunneling phenomenon, where an incident particle passes through a potential barrier which is higher than the potential energy of the particle. The important character of the tunneling, i.e., the relationship between the tunneling probability and the barrier width, is given by a simple one dimensional model. In quantum mechanics, a traveling plane wave will be reflected at the barrier or transmitted the barrier as illustrated in Fig. 2.1(a). By solving the Schrödinger equations under the boundary conditions, the transmission probability T is obtained in this form:

$$T = \frac{1}{1 + \dfrac{(k^2 + \kappa^2)^2}{4k^2\kappa^2}\sinh^2(d\kappa)} . \tag{2.1}$$

Here, d is the width of the barrier, k is the wave number ($=\sqrt{2mE_0/\hbar^2}$), κ is the inverse

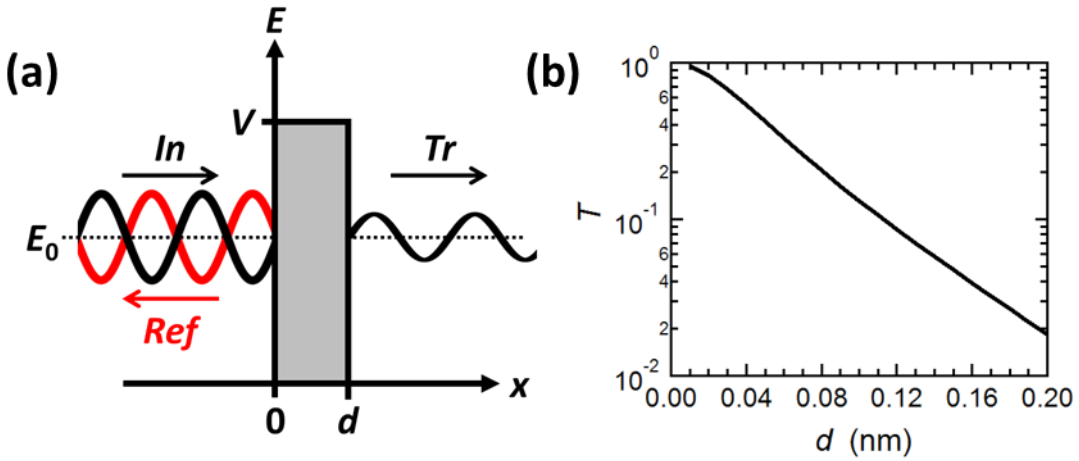

Fig. 2.1. (a) One-dimensional model of the quantum tunneling. The horizontal axis is the x-coordinate and the vertical axis represents the energy. The potential barrier is described as the gray region at $x = 0 \sim d$. The black and red waves in the left side represent the incident and reflected waves, and the black wave in the right side is the transmission wave. (b) Calculated transmission probability T under the conditions $m = 9.11 \times 10^{-31}$ kg (electron), $E_0 = 0.2$ eV and $V = 5.0$ eV.

decay length ($=\sqrt{2m(V-E_0)/\hbar^2}$), m is the mass of the particle, E_0 is the potential energy, V is the barrier energy and $\hbar$ is the Plank constant divided by 2π. Since κ and d are positive and the hyperbolic sine function [sinh(x)] exponentially increases when $x > 0$, it follows that the transmission probability T decreases exponentially as the barrier width d increases. Figure 2.1(b) shows the numerical calculation results of the transmission probability T versus the barrier width d (nm), where the parameters are selected for a free electron ($m_e \approx 9.11\times10^{-31}$ kg) with the energy $E_0 = 0.2$ eV and the barrier energy $V = 5.0$ eV. When $d\kappa >> 1$, Eq. (2.1) is transformed to simple form;

$$T = \frac{1}{1 + A\{\exp(2d\kappa) - \exp(2d\kappa) - 2\}} \approx \frac{1}{A\exp(2d\kappa)} = \frac{1}{A}\exp(-2d\kappa), \qquad (2.2)$$

where A is $\frac{(k^2+\kappa^2)^2}{16k^2\kappa^2}$. Due to the exponential dependence of T on d, the number of tunneling electrons per unit time (= the tunneling current I_t) depends also exponentially on the barrier width d.

2.1.2 Metal-Vacuum-Metal Tunnel Junction

To consider a tunnel junction of actual materials, the simplest model is employed as illustrated in Fig. 2.2, where two flat metal electrodes separated by the vacuum gap under a small bias voltage V_b. The potential barrier is expressed as

$$V(x) = E_F + \phi + eV_b\left(1 - \frac{x}{d}\right), \tag{2.3}$$

where ϕ is the work functions of the metal and E_F is the Fermi energy. According to the Wentzel-Kramers-Brillouin (WBK) approximation[1,2], the tunneling probability is given by the similar form of Eq. (2.2), where $\kappa = \sqrt{2m(V - E_0)/\hbar^2} \rightarrow \int_0^d \sqrt{2m(V(x) - E_x)/\hbar^2}\, dx$:

$$T(E_x) \approx \exp\left[-2\int_0^d \sqrt{2m(V(x) - E_x)/\hbar^2}\, dx\right]. \tag{2.4}$$

Here, E_x is the energy in the x-direction of the electron. Under the model of the free

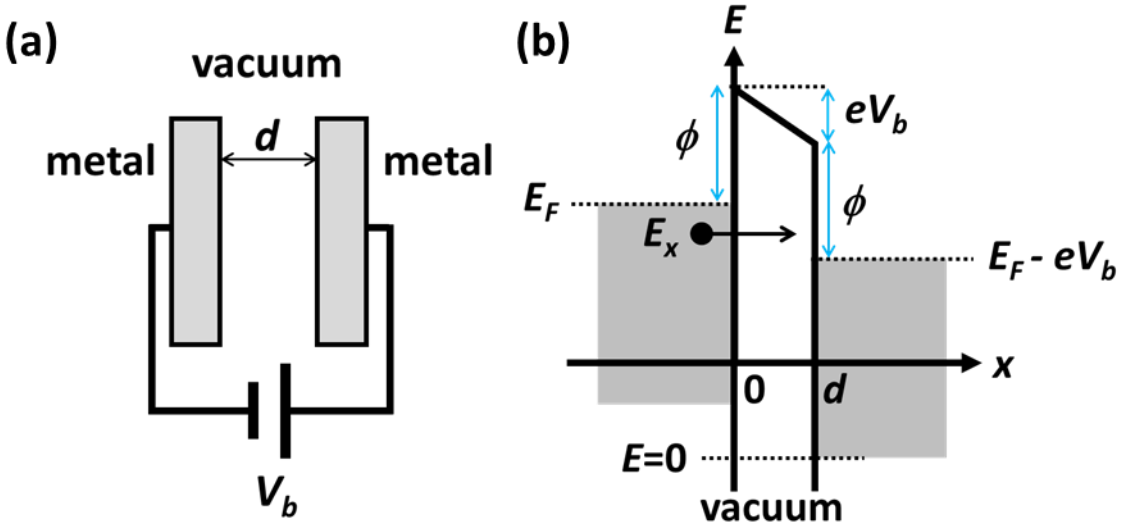

Fig. 2.2. (a) Schematic model of a metal-vacuum-metal junction (cross sectional view). The metals are flat plates separated by the vacuum region with the distance d. (b) Schematic energy diagram of the junction under the small bias voltage V_b. The black circle represents an electron with the kinetic energy E_x. ϕ is the work function of metals.

electrons in the metals, i.e., $E = E_x + E_y + E_z = \frac{1}{2m}\left(p_x^2 + p_y^2 + p_z^2\right)$, where p is the momentum of the electron, the tunnel current density J_t across the junction is described in this form;

$$J_t = \frac{2\pi e}{m^2}\int_0^\infty T(E_x)Y(E_x)\,dE_x \tag{2.5}$$

$$Y(E_x) = \frac{2m^3}{h^3}\int_{E_x}^\infty \left[f(E) - f(E + eV_b)\right]dE, \tag{2.6}$$

where $f(E)$ is the Fermi Dirac function and $Y(E)$ represents the density of states (DOS) at the energy E_x which contributes the electron tunneling.

When the bias voltage V_b is low, the potential barrier is approximated to the flat shape

$$V(x) \approx V(\frac{d}{2}) = E_F + \phi - \frac{1}{2}eV_b \equiv V_0 . \tag{2.7}$$

Since V(x) becomes constant, the tunneling probability in Eq. (2.4) is expressed in the same form of Eq. (2.2): exp[-2$d\kappa$], where $\kappa = \sqrt{2m(V_0 - E_x)/\hbar^2}$. The bias voltage V_b is small compared to ϕ, E_F - E_x is approximately zero and V_0 - E_x becomes approximately equal to ϕ. Therefore, $T(E_x) \approx \sqrt{2m\phi/\hbar^2}$. In addition, when the temperature is assumed to be absolute zero, the Fermi Dirac function is the Heaviside step function and the integration range is $E_x = E_F \sim E_F + eV_b$, yielding the current density in the simple form[1,2]:

$$J_t \approx \frac{e^2 V_b}{4\pi^2 \hbar d}\sqrt{2m\phi}\cdot\exp\left[-2d\sqrt{2m\phi/\hbar^2}\right]. \tag{2.8}$$

Equation (2.8) shows that the tunnel current is proportional to the bias voltage V_b.

2.1.3 STM Tunnel Junction

To express the tunnel current in STM in detail, the electron tunneling is modeled by transitions of electrons from the initial to the final states (ψ_μ and ψ_ν), which corresponds

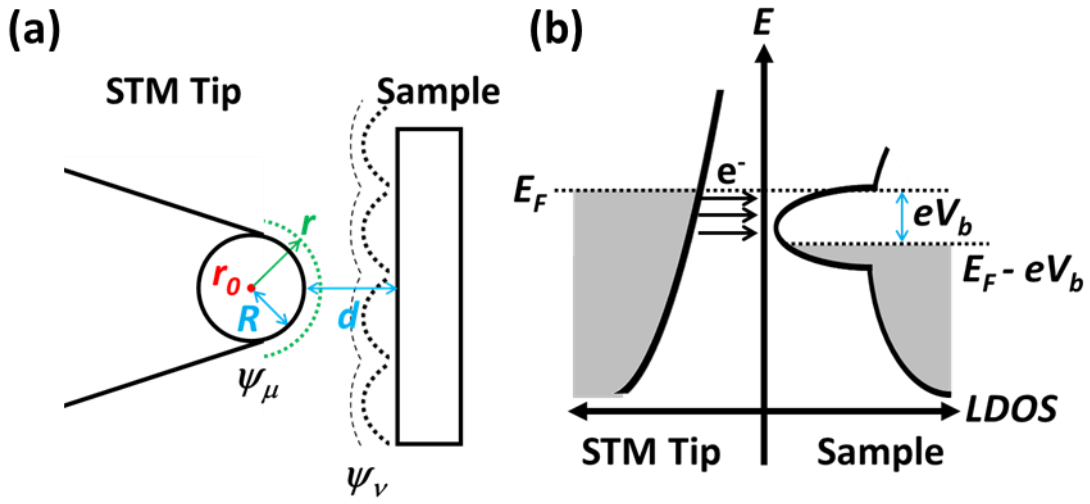

Fig. 2.3. (a) Schematic model of the STM tip / vacuum / substrate junction. The local radius of the curvature at the tip apex is R, and the center of the curvature is r_0. The STM tip-sample distance is d. The dotted lines illustrate the isosurfaces of the wave functions of the STM tip y_m and sample y_n. (b) Schematic energy diagram of the STM junction. The LDOS of the STM tip is illustrated as a simple parabolic shape.

to the expansion of the theoretical formalism in the previous section. Considering the electron tunneling from the STM tip ψ_μ to the sample ψ_ν under the bias voltage V_b, Bardeen[] showed the theoretical representation of the tunneling currents[3];

$$I_t = \frac{2\pi e}{\hbar}\sum_{\mu,\nu}\cdot\left|M_{\mu\nu}\right|^2\left[f(E_\mu)-f(E_\nu+eV_b)\right]\cdot\delta(E_\mu-E_\nu), \tag{2.9}$$

$$M_{\mu\nu} = \frac{-\hbar^2}{2m}\int_S\left(\psi_\mu^*\nabla\psi_\nu-\psi_\nu^*\nabla\psi_\mu\right)\cdot d\mathbf{S} \tag{2.10}$$

where E_μ and E_ν are the energies of the wave functions ψ_μ and ψ_ν measured from the E_F of the STM tip, $M_{\mu\nu}$ is the transition matrix element and $\delta(x)$ is the delta function.

Tersoff and Hamann[4,5] construct the model STM tunnel junction and calculated the tunnel current, as illustrated in Fig. 2.3. The radius of the curvature at the tip apex is R and its center is r_0. In this model, they assumed the wave functions of the tip and the sample consisting of s-type spherical wave functions; the wave function of the tip ψ_μ is expressed as

$$\psi_\mu(r) = A\frac{1}{|r-r_0|}\exp\left(-\kappa|r-r_0|\right) \tag{2.11}$$

and the wave function of the sample ψ_ν is expressed by the product of the decay term towards the vacuum (vertical to the surface) and the periodic wave function parallel to the sample surface. Here, the inverse decay length $\kappa = \sqrt{2mE_0/\hbar^2}$, the work functions of both the STM tip and sample are considered to be identical: ϕ. By these assumptions, the transition matrix element $M_{\mu\nu}$ can be calculated in a detail form.

In the same way of the previous section, when the temperature is low, the Fermi Dirac function can be replaced to the Heaviside step function and the summation about μ and ν is restricted to the energies $E_\mu = E_\nu = E_F - eV_b \sim E_F$. In addition, the bias voltage V_b is assumed to be low, which does not cause the change of the wave functions. The tunneling current is then transformed to

$$I_t = \frac{2\pi e}{\hbar}\cdot\int_{E_F-eV_b}^{E_F}\rho_\mu(E)\cdot\left|M_{\mu\nu}\right|^2\delta(E_\mu-E)\,\delta(E_\nu-E)\,dE\,. \tag{2.12}$$

Substituting the calculated $M_{\mu\nu}$ in Eq. (2.11), the tunnel current I_t is obtained as

$$I_t \propto \frac{h^3 e}{m^2}R^2\cdot\Omega^{-1}\int_{E_F-eV_b}^{E_F}\rho_\mu(E)\cdot\rho_\nu(r_0,E)\,dE \tag{2.13}$$

$$\rho_\nu(r_0,E) = \sum_\nu|\psi_\nu(r_0)|^2\,\delta(E_\nu-E)\,, \tag{2.14}$$

where Ω is the volume of the STM tip and $\rho_\nu(r_0,E)$ is the local density of states (LDOS) of the sample at the position r_0 and at the energy E. In addition, due to the simple decaying character of the wave function of the sample ψ_ν towards the vacuum, the LDOS is expressed by the product of the LDOS at the surface $\rho_\nu(E)$ and the decay term $\exp\left[-2\kappa(d+R)\right]$:

$$\rho_\nu(r_0,E)\propto\rho_\nu(E)\cdot\exp\left[-2\kappa(d+R)\right]. \tag{2.15}$$

The difference of the work functions of the STM tip and the sample and the effect of small bias voltage can be introduced by replacing κ in the same developments of Eqs. (2.3), (2.4) and (2.7),

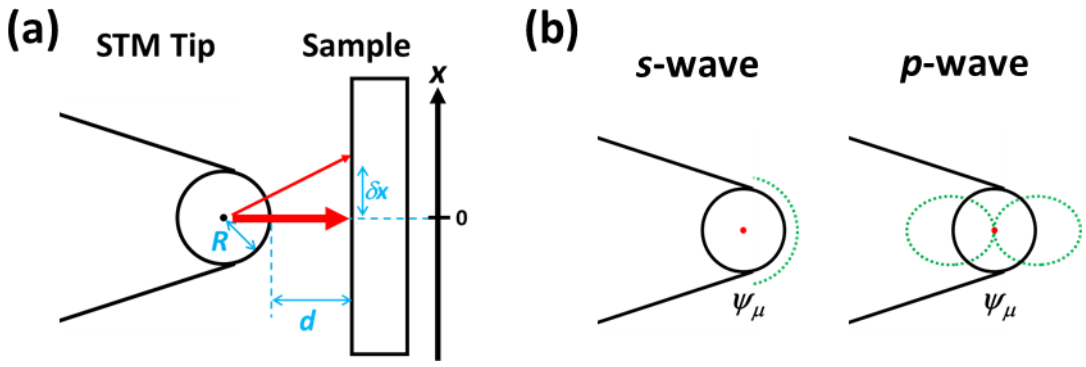

Fig. 2.4. (a) Electron tunneling processes from the STM tip to the different position of the sample. The red arrows indicate the tunneling paths and the size of arrows indicates the magnitudes of the tunneling probability. (b) Schematic illustrations of *s*-type wave and *p*-type wave at the STM tip.

$$\kappa = \sqrt{\frac{2m}{\hbar^2}\left(E_F + \frac{\phi_\mu + \phi_\nu}{2} - \frac{eV_b}{2} - E\right)}, \tag{2.16}$$

and the tunneling probability is obtained as

$$T(d, E, V_b) = \exp\left[-2(d+R)\kappa\right], \tag{2.17}$$

where κ is that of Eq. (2.16). Finally, the tunneling current I_t is expressed as

$$I_t \propto R^2 \int_{E_F - eV_b}^{E_F} \rho_\mu(E) \cdot \rho_\nu(E) \cdot T(d, E, V_b)\, dE\,. \tag{2.18}$$

The tunnel current I_t is described by the LDOS of the STM tip and sample and the tunneling probability.

The vertical resolution of STM is realized by the exponential dependence of the tunneling probability T on the distance d. The lateral resolution is also estimated from the tunneling probability T. As shown in Fig. 2.4(a), the electron tunneling from the STM tip to the sample at just beneath the STM tip ($x = 0$) dominantly contributes to the tunnel current It and the contribution from the position ($x = \delta x$) is lower because the tunneling probability decays ($d + R \rightarrow \sqrt{(d+R)^2 + (\delta x)^2}$). Note that the electronic states of the tip is approximated by the *s*-type wave function in the model presented above. Considering the *p*- and *d*-type wave functions at the STM tip apex produces a higher lateral resolution due

to the orbital angular momentum and the spatial distribution of the orbitals[6-8], as shown in Fig. 2.4(b). In fact, STM can observe each atom of the surface (for example atoms at the surface of metal single crystals) and this lateral resolution is attributable to the p- and d-type wave functions at the STM tip. The vertical and lateral resolutions are well higher than the sub-atomic size.

2.2 Principle of Scanning Tunneling Spectroscopy (STS)

2.2.1 Scanning Tunneling Spectroscopy

Since the tunneling current I_t in Eq. (2.18) has an integration term which is a product of LDOS of the STM tip and the sample, it is expected that the differential conductance dI_t/dV_b gives the integrand term when the tunneling probability T is regarded as a constant in this small energy range:

$$\frac{dI_t}{dV_b} \propto \rho_\mu(eV_b)\cdot\rho_\nu(eV_b). \tag{2.19}$$

When the LDOS of the STM tip can be assumed to be constant, the differential conductance dI_t/dV_b is proportional to the LDOS of the sample. Hence, an energy spectrum dI_t/dV_b versus V_b reflects the LDOS shape of the sample (Fig. 2.5). This tunnel spectroscopy by means of STM is called scanning tunneling spectroscopy (STS) and the spectra obtained by STS are called STS spectra. Although many assumptions are included in the formalism above, it is widely accepted that the STS spectrum gives a good approximation of the sample LDOS. More detail consideration for the differential conductance are given by several works[9-11], and it has shown that the normalized conductance $(dI_t/dV_b)/(I_t/V_b)$ provides better estimation of the LDOS.

The schematic pictures of the procedure in STS measurements are shown later in Fig. 2.13.

2.2.2 Inelastic Electron Tunneling Spectroscopy (IETS)

The electron tunneling itself is an elastic event, however, the inelastic process can

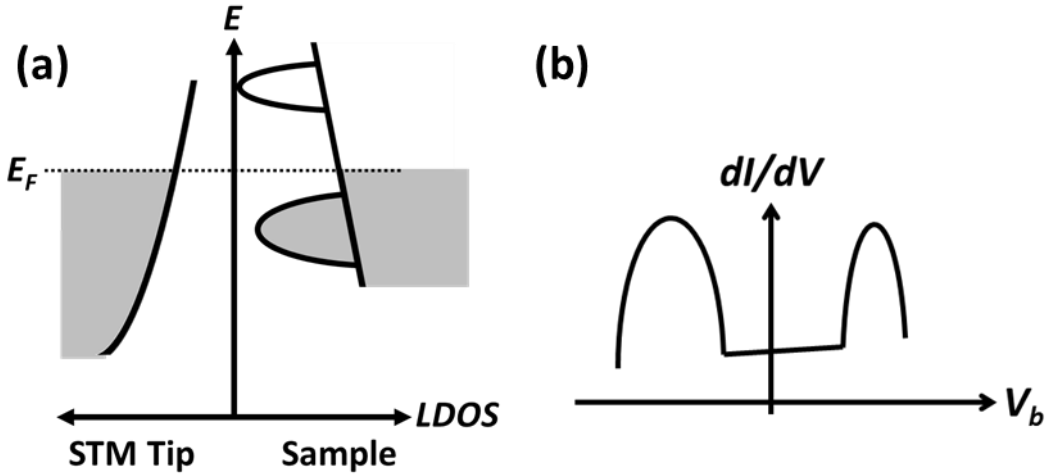

Fig. 2.5. (a) Schematic LDOS of the STM tip and sample. (b) Schematic image of a STS spectrum for the sample in (a).

accompany the electron tunnel phenomenon. Figure 2.6(a) shows the schematic model of the inelastic tunneling, where an energy loss process with the energy ε exists and the energy of the bias voltage eV_b is equal to ε. When eV_b is lower than ε, the inelastic tunnel process cannot occur because there is no unoccupied state at the energy of the final state of the tunnel electron. In contrast, when eV_b is equal to or more than ε, the inelastic tunnel process becomes available. In IETS, we can observe inelastic processes such as vibrational excitations of the adsorbate or the surface phonon[12,13], and magnetic excitations of the adsorbates[14].

As shown in Eq. (2.8), the tunnel current I_t linearly increases with V_b under the condition that V_b is very low. A same expression can be obtained from Eq. (2.18) assuming the LDOS of the STM tip to be constant near the E_F; the integration in Eq. (2.18) can be

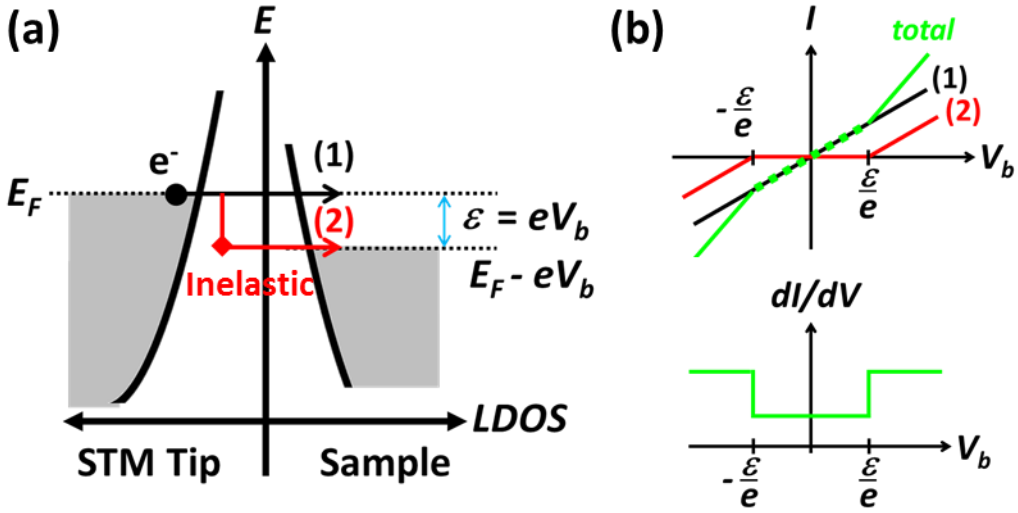

simplified to

$$I_t \propto R^2 \cdot eV_b \cdot \rho_\mu(E_F) \cdot \int_{E_F - eV_b}^{E_F} \rho_\nu(E) \cdot T(d, E, V_b)\, dE\,. \tag{2.20}$$

Hence, the current-voltage (I-V) spectra is approximated to be the linear shape as shown in Fig. 2.6(b). The black and red lines are the tunnel current from the contributions of the elastic and inelastic path shown in Fig. 2.6(a). The total current is shown as a green line and its gradient changes at $V_b = \varepsilon/e$ due to the opening of the inelastic path. The lower panel of Fig. 2.6(b) represents a differential conductance (dI/dV) spectrum of the upper panel, which shows a symmetric step function shape with respect to $V_b = 0$.

Fig. 2.6. (a) Schematic energy diagram of the STM tip and sample. The black arrow with the number (1) is the path of the elastic tunnel process and the red arrow with the number (2) is the inelastic path where the energy loss is ε. (b) Schematic STS spectra of the situation shown in (a). The upper and lower figures are the current-voltage and differential spectra. In the upper figure, the black and red lines with the numbers (1) and (2) correspond to the elastic and inelastic path shown in (a).

The increase magnitude of I and dI/dV at the excitation energy can roughly be regarded as a transition probability of the inelastic process, considering that the inelastic process is basically a transition between the initial and final state of the tunnel electron. Typically, the increase magnitude of dI/dV for the vibrational excitations is a few percent. In contrast, in the magnetic excitation process, the increase magnitude of dI/dV is commonly large.

The thermal broadening and other experimental broadening also appear in the IETS spectra. It is known that the effect of the finite temperature T appears as a broadening by Gaussian with the full width at half maximum (FWHM) equal to $5.4k_bT$[15]. It is important to measure at a sufficiently low temperature to obtain the IETS spectra, i.e., the thermal energy should be lower than the excitation energy and the intrinsic life time of the excitation process. The energy of the magnetic excitation is typically in the range from few meV to several tens meV. Hence, it requires at liquid He temperature to observe

the magnetic excitations such as the spin flip, Zeeman effect and magnetic anisotropy.

2.3 Experimental Apparatus and Practical Techniques

2.3.1 Outlines

In the following sections, we will describe the apparatus low-temperature STM (LT-STM) used in this study and the detail procedures of experiments; the STM observations, the STS spectra and the STM contact measurements.

Figures 2.7 and 2.8 show pictures and schematic figures of the apparatus and equipment used in this work. The apparatus consists of four vacuum chambers separated by gate valves; the load-lock chamber, the preparation chamber, the stock chamber and the STM head. The STM head is located inside a cryostat, which is filled with liquid helium. The cryostat equips a superconducting magnet. The whole system is mounted on the air suspension anti-vibration table.

I used two similar STM systems; the one is operated around the liquid He temperature (6.2 K) and the other is a very low-temperature STM (0.4 K) equipped with the ^{3}He cooling system, which we call milli-kelvin STM. The milli-kelvin STM is located in a soundproof

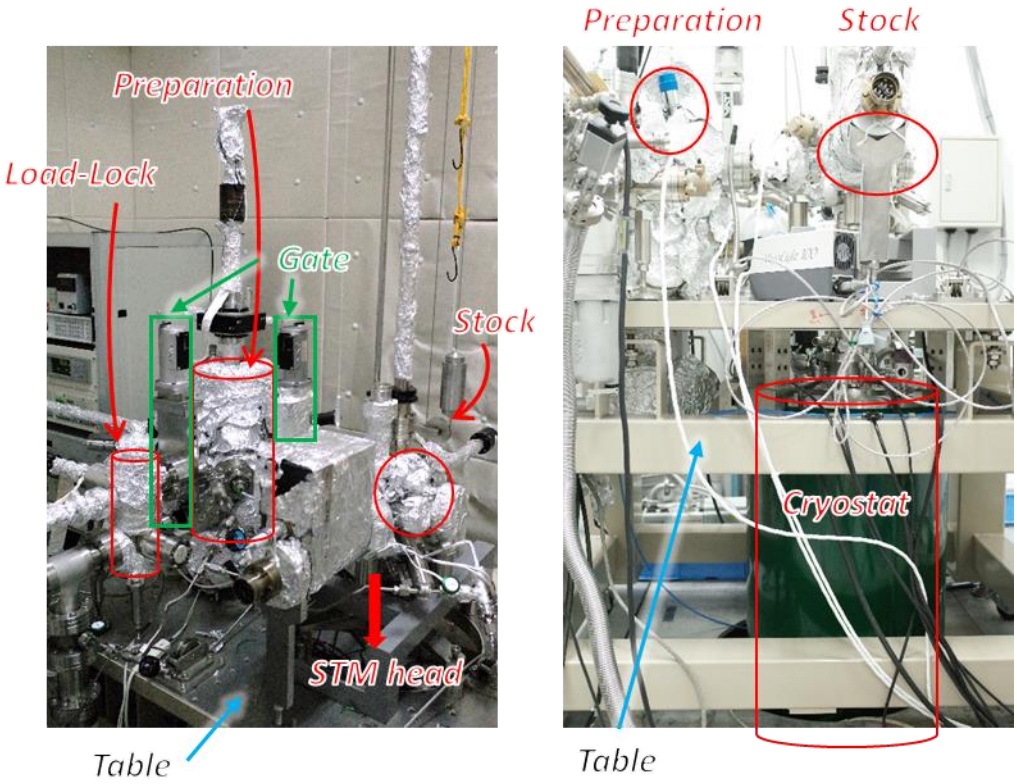

Fig. 2.7. Photos of STM apparatus. The left picture shows a bird's-eye view and the right picture shows the side view.

room for reducing the acoustic noise. The controllers and operators of STM are located outside the soundproof room during STM operation.

Except for the lord-lock chamber, the vacuum system is basically in an ultra-high vacuum (UHV) condition, where the base pressure is below 5 x 10^{-11} Torr (the detection limit of a vacuum gauge).

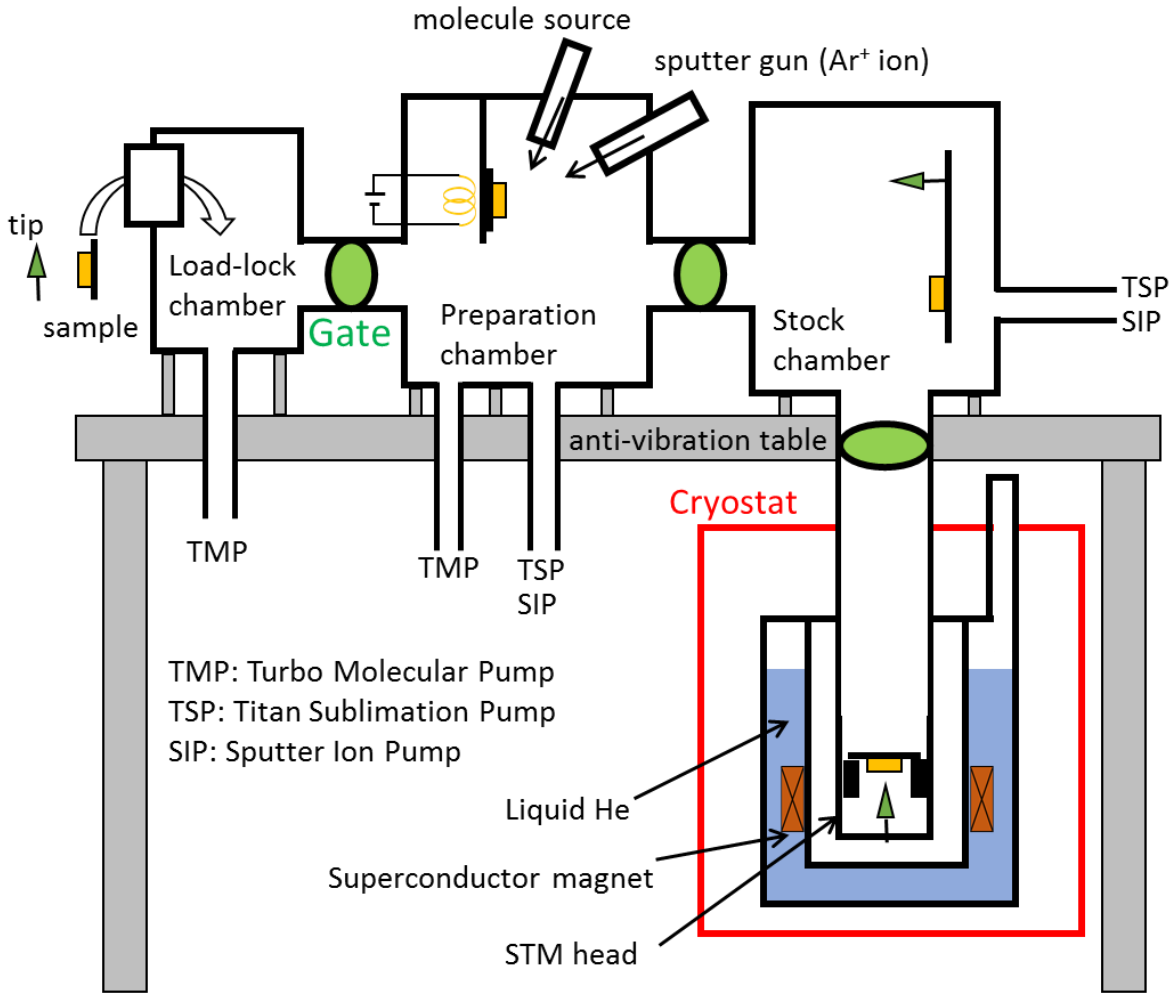

Fig. 2.8. Schematic illustration of the STM apparatus.

2.3.2 Vacuum System and Cryogenic System

The load-lock, preparation and stock chambers are equipped with several combination of the vacuum pumps: turbo molecular pump (TMP), sputter ion pump (SIP) and Ti sublimation pump (TSP). The TMP pump requires roughing pump to keep the backing pressure low. We use the rotary pump as the roughing pump. Although we can achieve the UHV condition in the chamber by only the TMP with the rotary pump, both the TMP and the rotary pump cause fatal vibration noise to the STM observation because they are

mechanical pumps. Meanwhile, the SIP and TSP are getter pumps, where the residual gases in the chamber are trapped in the pump, and available during the STM observation. In our system, the SIP runs almost all time during the experiments except for the sample preparation process. Additionally, when we measure STS spectra in high resolution, all pumps, thermometers, and vacuum gauges are turned off to avoid the noise from the electric circuits. The STM head has no vacuum pump such as TMP and SIP. Since the STM head is installed in the cryostat filled with liquid He (the base temperature is around 6 K), the chamber itself works as the cryopump and the base pressure of the STM head is expected to be lower than the stock chamber. The combination of these pumps achieves the UHV condition (base pressure is below 10^{-11} Torr).

The sample and STM tip are installed at the load-lock chamber. The sample preparation is performed in the preparation chamber, equipped with a sputter gun and various evaporation source. All installed samples and STM tips are stocked in the stock chamber.

The cryostat equipped with the superconducting magnets is a commercial one (Cryogenic. Ltd.). The milli-kelvin STM has the ^{3}He cooling system. The base temperature of the STM head is around 6 K and the temperature can be decreased to 2.7 K and 400 mK during the operation. In this study, the magnetic field is applied vertical to the sample surface up to 11 Tesla (T).

2.3.3 STM

The STM system is a commercial one (UNISOKU Co., Ltd.) designed for the operation under the UHV-LT conditions and under a high magnetic field by the superconducting magnets. Figure 2.9 shows a schematic image of the STM head and Fig. 2.10 shows a picture of the STM tip holder and the sample holder. To operate under the magnetic field, the STM head consists of non-magnetic materials. The STM tip and sample holders we used are also made of non-magnetic parts.

The STM head hangs from the chamber by the spring suspension. In this STM system, the STM tip moves to scan the sample. The scanner piezo and the coarse piezo are under the STM tip mounting position. The scanner piezo provides the precise motion of the STM tip in the *xyz* directions during the STM measurements (up to a few tens of nanometers long in the *z* direction and several hundred nanometers in the horizontal

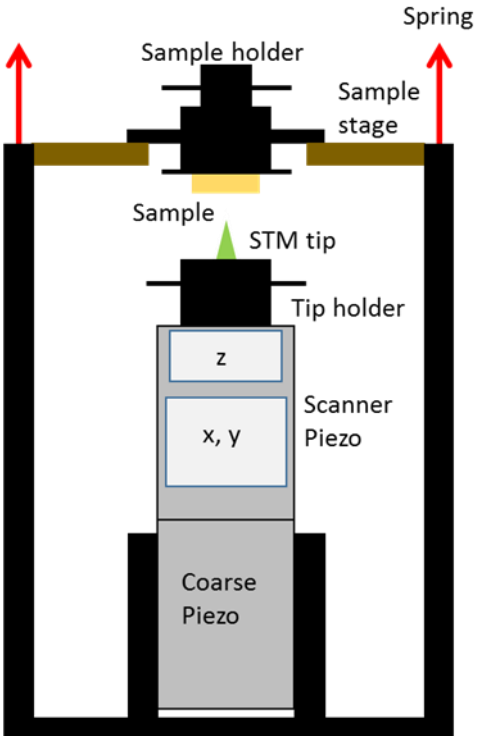

Fig. 2.9. Schematic illustration of the STM head.

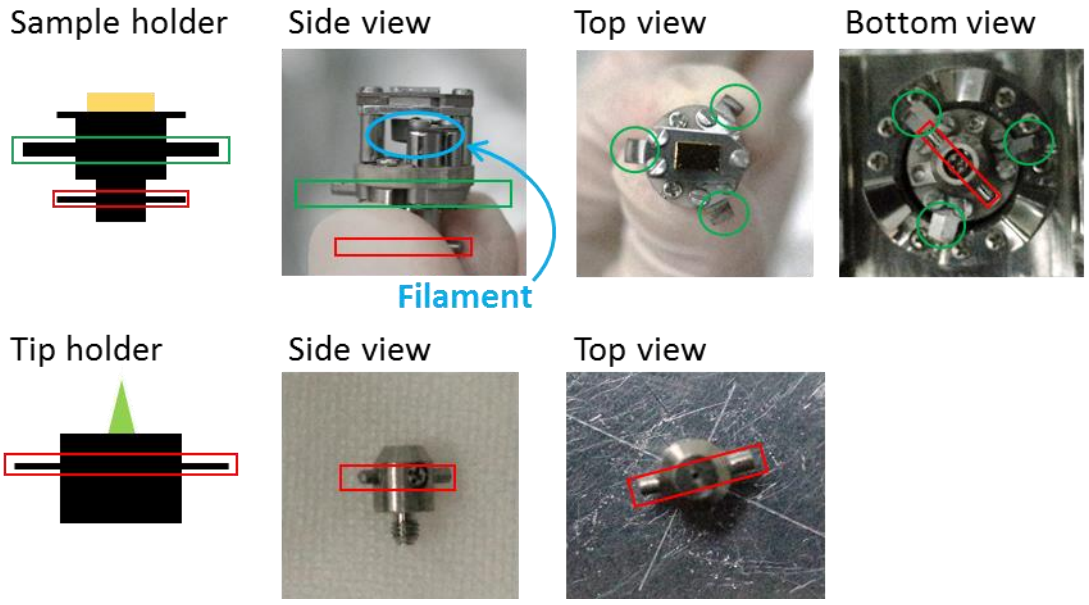

Fig. 2.10. Photos of the sample holder and tip holder. The red squares show the bars for the manipulator to catch and transfer the holders in the vacuum system. The green squares and circles shows the plates for mounting the sample holder on the stage. The sample holder has a filament below the sample, denoted by the blue circle. The filament is used to anneal the sample in the cleaning process.

direction). The coarse piezo is used to approach the STM tip to the sample from the initial position (separated about few millimeters) to the tunnel regime.

2.3.4 Control System and Procedure of Measurements

In this study we use two control systems; a commercial one (RHK Technology, Inc.) operates the usual STM and STS measurements and the other one is a home-made one programmed by using the commercial software "LabVIEW" (National Instruments Co.) for the STM contact measurements. In this section, we will briefly introduce the practical procedure to perform the (1) STM (2) STS and (3) STM contact measurements by these control systems.

Figure 2.11 shows a brief image of the electric circuits between the STM and

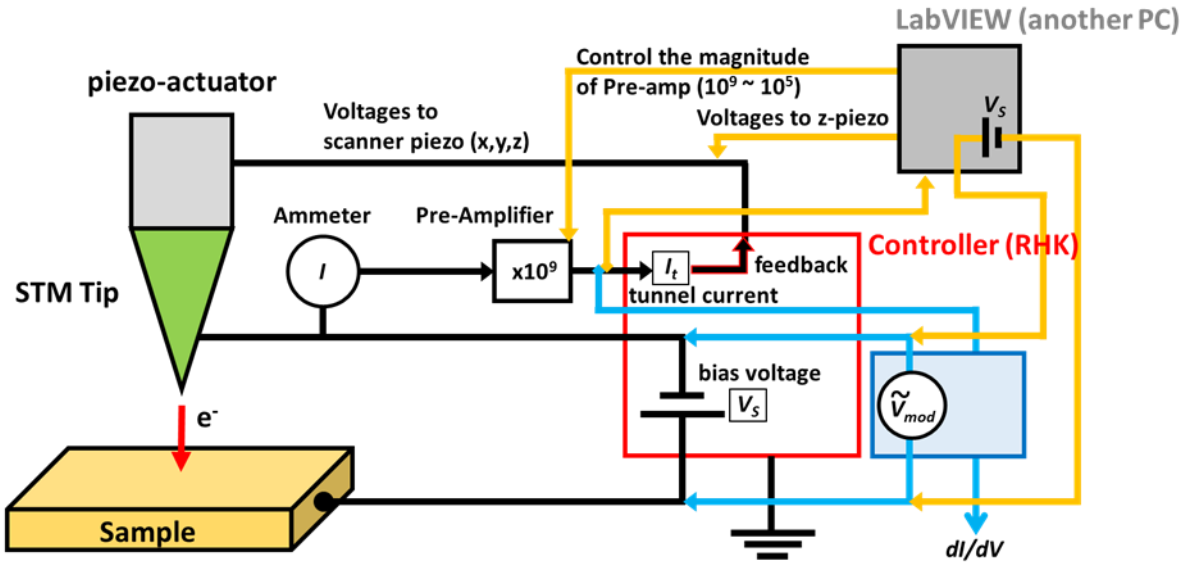

Fig. 2.11. Schematic image of STM and the controller. The lines indicate the electric circuits to control devices, apply voltages and read signals. The atomically sharp tip is controlled by the piezo-actuator. The controller (RHK) controls the piezo-actuator and the bias voltage applied between the tip and sample, and measures the tunneling currents. The blue and orange lines represent circuits for the lock-in amplifier and the control program made of LabVIEW, respectively. The Lock-in amplifier is used to obtain the differential conductance (*dI/dV*) in STS measurements. The LabVIEW program is used in the STM contact measurement.

controllers. The pre-amplifier amplifies the tunnel current (typically in nA range) to the DC voltage signal to be read by the controller and computers (in the range of ± 10 V DC). In this study, the magnification is set at 10^9 during the STM and STS measurements.

(1) STM observation and STM image

The results of the scanning tunneling microscopy is presented as the STM image. We firstly explain the STM current image obtained by the constant height mode. Here, we assume the sample as a single crystal of a metal element. The STM current image is obtained by recording I_t as a function of the horizontal position of the STM tip controlled by the piezo-electric device. The STM tip scans the sample surface by moving in the horizontal direction (the *x*-*y* plane) while keeping the vertical position (the *z* direction), as

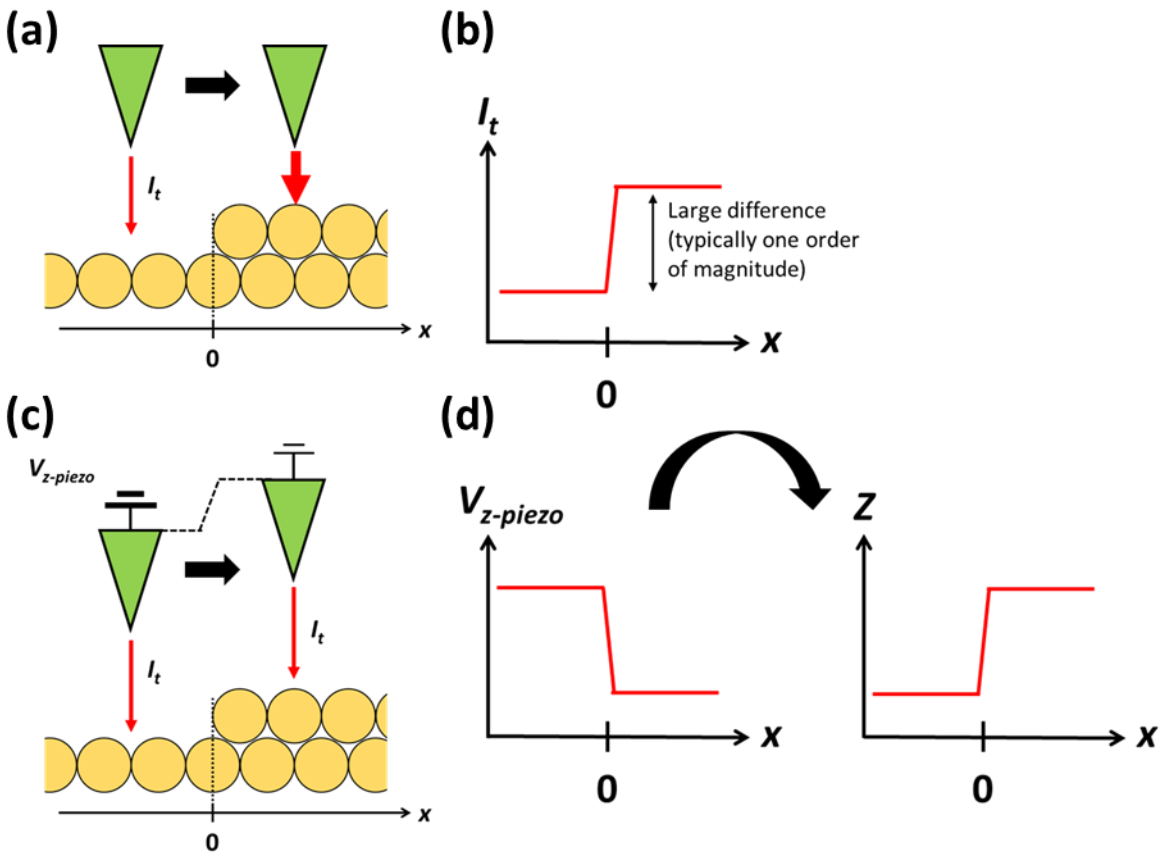

Fig. 2.12. Schematic pictures of the STM observations. (a) Constant height mode. (b) Tunnel current versus horizontal position x obtained by the constant height mode in (a). (c) Feedback mode. In the picture, the voltage applied to the z-piezo $V_{z\text{-}piezo}$ is reduced to shorten the z-piezo when the STM tip moves away from the sample. (d) Obtained graph $V_{z\text{-}piezo}$ versus x. We can obtain the real-space length z from $V_{z\text{-}piezo}$.

schematically illustrated in Fig. 2.12(a). It can be straightforwardly understood that the amplitude of I_t reflects the surface structure [Fig. 2.12(b)]. Although the STM current imaging by the constant height mode is very simple, there are some practical problems in this mode; there exist atomic steps at the sample surface, which may cause the STM tip crashing. The tunneling current drastically changes when there are atomic steps. For example, when several atomic steps exist in one scan area, we have to measure the tunneling current in the three digit (for instance, from 100 pA to 100 nA).

Instead, the so-called STM topographic image is generally provided by using the

feedback mode. In this mode, we set the tunneling current and the bias voltage (set points). The vertical position of the STM tip is controlled by the feedback method to keep the tunneling current at the value of the set points during the scan, as shown in Fig. 2.12(c). The STM topographic image is created by plotting the voltage applied to the z-piezo device in the feedback method. In the actual STM topographic images, the applied voltage to control the z-piezo is converted to the real-space length [Fig. 2.12(d)]. The acquisition of STM images by the feedback mode is more stable than the constant height mode. In this study, all STM images are the topographic image obtained by the feedback mode. The set points I_t and V_S are always shown with the STM images. In this study, we show the bias voltage V_b as the sample bias V_S, which indicates that the bias is applied to the sample with respect to the STM tip.

We control several parameters in the STM measurements. The sample bias determines the energy of the tunneling electrons contributing to the current. The set points determines the distance of the STM tip and sample. Parameters of the feedback loop (such as the time constant and loop gain) and the scan speed should be tuned to obtain clear topographic images.

(2) STS and IETS

The conventional STS measurement is performed as follows; the horizontal position of the STM tip is set at the target position (for example, above a target molecule). The vertical position of the STM tip is also determined by the set points (I_t and V_S). Then, the feedback loop is turned off and the STM tip position is held. The bias voltage sweeps and the current is recorded, as illustrated in Fig. 2.13. Since the differential conductance dI/dV reflects well the DOS of the sample, STS spectra are often provided in the form of dI/dV versus V. In this study, we provide the dI/dV spectra as the STS spectra if not otherwise specified.

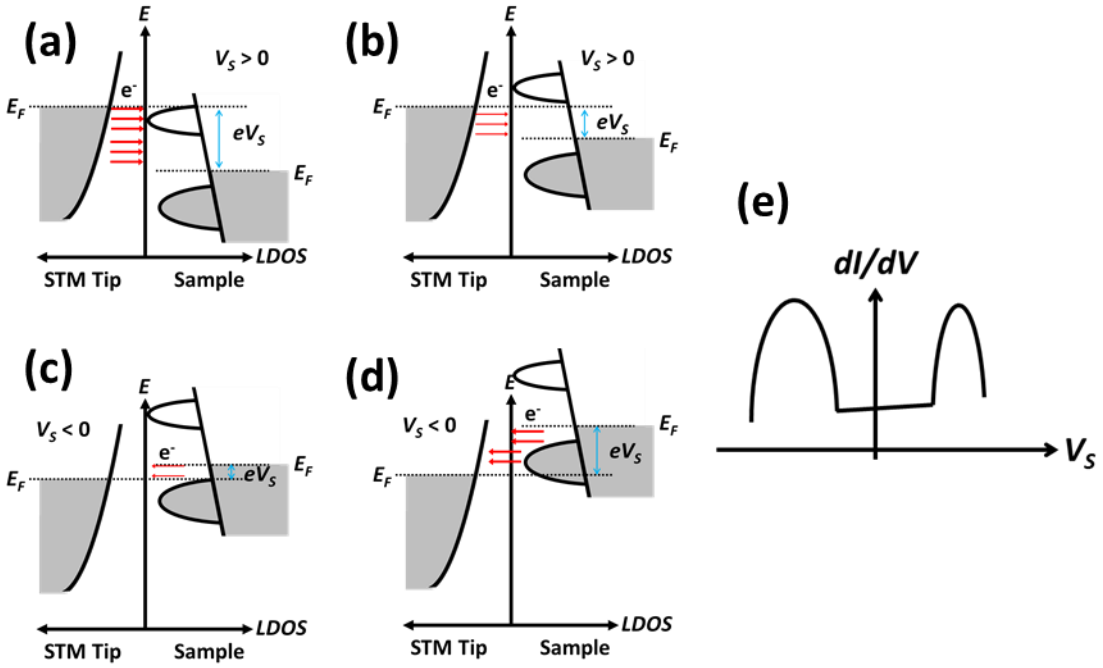

Fig. 2.13. Schematic images of the procedure in the STS measurements. (a)-(d) The LDOS of the STM tip is described as the simple parabolic shape and the LDOS of the sample shows two peaks below and above the E_F. The sample bais V_S decreases from (a) to (d). The red arrows represent the electron tunneling. (e) STS spectra obtained from this sample. The unoccupied states and occupied states of the sample are observed at negative ($V_S < 0$) and positive region ($V_S > 0$) in the spectra, respectively.

Generally, the *dI/dV* spectra are directly obtained by the lock-in detection method, not via the numerical differentiation of the *I-V* spectra, in order to obtain the spectra with good signal/noise ratio. The amplitude of the modulation voltage V_{mod} added to the sweeping voltage is always provided in this study. The frequency of the modulation voltage comes to be important when discussing the dynamics.

In the STS measurements, we have to tune the parameters about the bias voltage; the sweep range, increments and sweep speed. The modulation bias is applied by the lock-in amplifier (Oxford Instruments) (Fig. 2.11).

As mentioned, the bias voltage is presented as the sample bias in this study. Hence, the spectral shape in the negative (positive) V_S region reflects the occupied (unoccupied) states of the sample, as shown Fig. 2.13(e). In addition, the position $V_S = 0$ corresponds

to the Fermi level of the sample. We often regard the position V_S = 0 as the E_F. For example, when there is a peak at V_S = -0.5, we describe that the occupied states are observed at 0.5 eV below the E_F.

(3) STM Contact Measurement

As demonstrated in many works, STM manipulation techniques enables us to selectively access to the single adsorbate by the atomically sharp STM tip[16,17]. In the STM contact measurement, the STM tip contact to the adsorbate and forms a nano junction of the adsorbate. The process of the STM contact measurement is schematically shown in Fig. 2.14. The detail process is as follows; (i) find a target adsorbate in an STM image, (ii) settle the horizontal position of the STM tip above the target[Fig. 2.14(a)], (iii) turn off the feedback loop and change the magnitude of the pre-amplifier to measure the large current in the contact measurement, (iv) set a certain bias voltage to measure the current and conductance[Fig. 2.14(b)], (v) move the STM tip towards the sample by controlling the vertical position of the STM tip and measure the current flowing across the junction[Figs. 2.14(c),(e)], (vi) at a certain position, stop approaching the STM tip and retract the STM tip[Fig. 2.14(d)], (vii) obtain an STM of the same region to see whether there appears any changes on the target adsorbate, surface and STM tip.

The result of the contact measurement is presented as the *G-Z* curve, where the conductance $G = I/V$ is plotted as a function of the distance Z [Fig. 2.14(e)]. In the tunnel regime, G increases exponentially as Z increases. At the contact regime, G reaches a saturated value due to the formation of the junction. During the STM contact measurement, the movement of the STM tip can be stopped and *I-V* spectra can be obtained at any position. The modulation voltage from the lock-in amplifier can also be applied during the contact measurement.

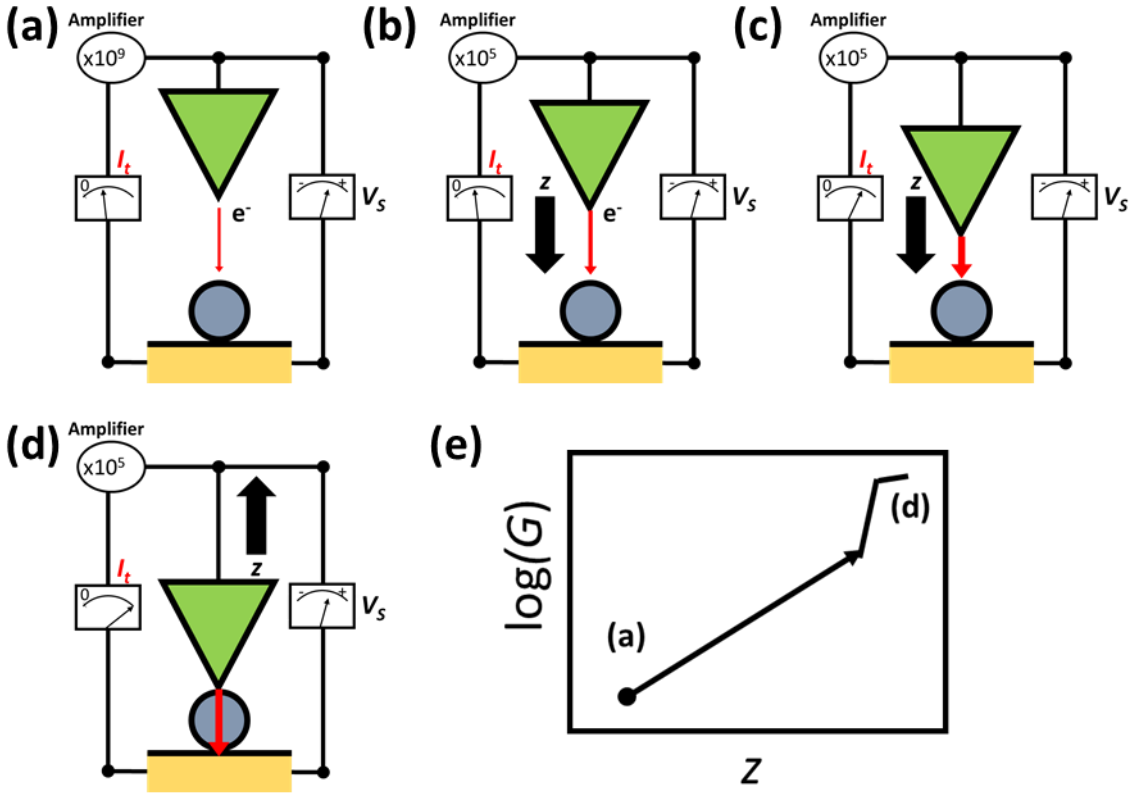

Fig. 2.14. Schematic images of the STM contact measurement. (a) The initial situation. The magnitude of the pre-amp is 10^9 (the usual condition in the STM observation). The distance between the STM tip and sample is determined by the set points. (b) The STM tip is approaching to the sample. The magnitude of the pre-amp is set to small value such as 10^5. (c) The current increases as the tip approaches. (d) The STM tip is retracted after it contacts the sample. (e) Schematic figure of the *G*-*Z* curve.

The contact measurement is controlled by the home-made program. There is two output signals and two input signals [Fig. 2.11]; output signals are the voltage to control the scanner piezo (*z*-direction) and the sample bias voltage *Vs*, while input signals are the current across the junction *I* and the output from the lock-in amplifier corresponding to *dI/dV*. After turning off the feedback loop, the voltages applied to the scanner piezo is held. Additional voltage is applied to the *z* direction of the scanner piezo to move the STM tip towards the sample. The sample bias is applied to measure the current and conductance and is controlled to obtain the *I*-*V* spectra.

2.4 Density Functional Theory (DFT)

Both the developments in quantum theory and the computers enables us to simulate the properties of materials (atomic structure, electronic states and so on) based on quantum mechanics. At present, the computational calculations are widely performed in materials science. In this study, we have the benefit of theoretical calculations based on the VASP (Vienna Ab-initio Simulation Package[18,19]) to consider our experimental results. The VASP package calculate the wave functions based on density functional theory (DFT). We briefly introduce the concept of this theoretical calculation method.

As written in every textbook of quantum theory, solving the Schrödinger equations is required in order to determine wave functions of electrons in a material such as the bulk materials, clusters and molecules. However, it is almost impossible to solve the Schrödinger equations and obtain the exact solutions in a multi-particle system (even for a He atom). Various approximations are introduced to avoid this problem such as Born-Oppenheimer approximation, one-electron approximation (mean field approximation / Hartree approximation). By introducing electron-electron correlations by several methods, these formalism such as Hartree-Fock equation have succeeded in reproducing physical properties of materials, however, there is an inevitable problem; it takes rather long time in the computationally calculations because we have to consider many wave functions.

Density functional theory (DFT) provides a different concept in the theoretical calculations. The concept of DFT is that Hamiltonian operators can be written by a functional of the electron density of the system. The electron density function n(r) determines the potential V(r) and hence the wave function Φ is determined by n(r). It is proved that the wave function Φ is uniquely determined by n(r) when the functional is

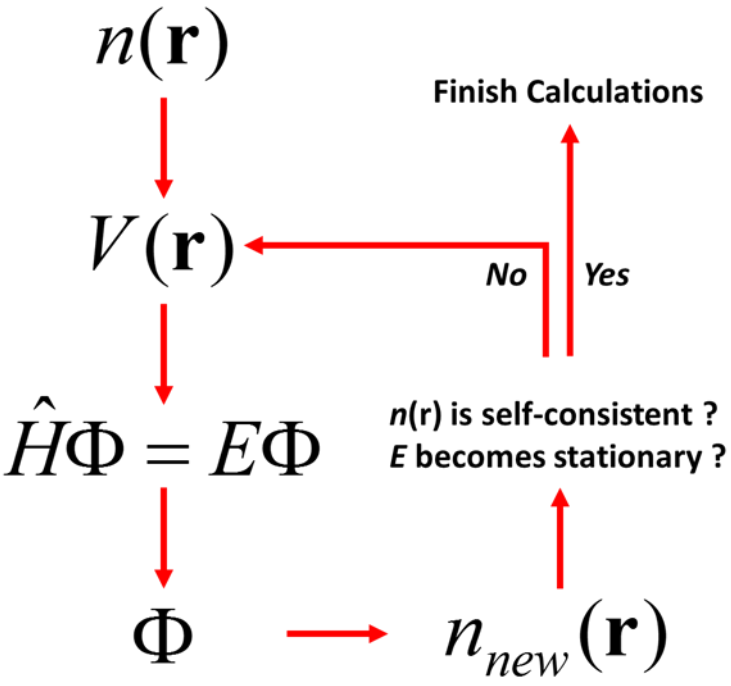

Fig. 2.15. Flow chart of DFT calculations with the self-consistent field method.

correct. Thomas-Fermi theory, Hohenberg-Kohn theory[20] and Kohn-Sham method[21] are the fundamentals of DFT and DFT calculations[22]. We briefly describe the calculation procedure in DFT with the self-consistent field method (Fig. 2.15);

(1) the initial n(r) is determined by the basis function and the initial setting of the material (position of atoms)

(2) the Hamiltonian operator is calculated by n(r)

(3) the Schrödinger equation is solved and Φ is obtained

(4) the n(r) is again calculated and the total energy of the system is calculated

(5) judge that the energy is stationary and the n(r) is self-consistent. If not, the calculation continues from step (2) by the obtained n(r).

2.5 Materials

In the following sections, we will describe the materials used in this study. As introduce, three systems were studied: C_{60} molecules on Pb(111) with the Nb tip, SiNR on Ag(110) and FePc on Au(111).

2.5.1 Preparation of Substrates

The three metal substrates used in this study are Pb(111), Ag(110) and Au(111). Figure 2.16 shows the schematic structures of these samples. The radius of the atoms are as follows: r_{Pb} = 175 pm, r_{Au} = 144 pm and r_{Ag} = 144 pm. The substrates were the polished single crystals, which are commercially available. The single crystals are

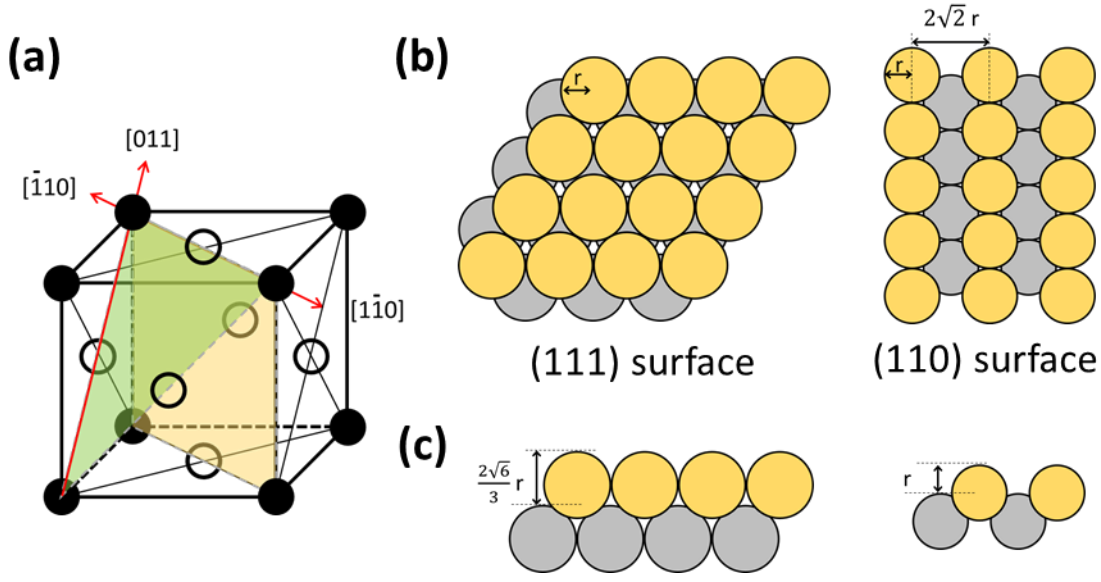

Fig. 2.16. (a) Unit cell of the fcc structure. The white and black circles represent atoms. The green and orange plane indicate the (111) and (110) surfaces, respectively. (b) Top view of atomic structures of the fcc-(111) and -(110) surfaces. The orange circles and gray circles represent the 1st and 2nd layer atoms. (c) Side view of the (111) and (110) surfaces. The lengths of the monoatomic step height are shown.

mounted on the sample holder and then installed into the chamber [Fig. 2.8].

The cleaning of the substrates is performed by the several cycles of Ar^+ ion sputtering and annealing process, as shown in Fig. 2.17. Ar atoms are introduced into the preparation chamber, ionized by the electrodes and accelerated by the electric fields. The sample surface is sputtered by the high energy Ar^+ ions. The impurity adsorbates and surface oxide layers are cleaned by the sputtering. After the sputtering, the sample is annealed to obtain the flat surface. The Ag(110) and Au(111) samples were heated by the electron bombardment method. The filament equipped with the sample holder emit thermal electrons. Positive voltage is applied to the sample with respect to the filament so that the emitted electrons are accelerated and hit the plate beneath the sample. The annealing temperature of the Ag(110) and Au(111) samples were at around 800 K. Because the melting temperature of Pb is low (about 600 K in the atmospheric pressure), the Pb(111) sample was heated by only the Joule heat from the filament at the temperature below the detection limit of the radiation thermometer. The annealing condition of the Pb(111) sample was determined in the following way; a thermocouple was connected to the

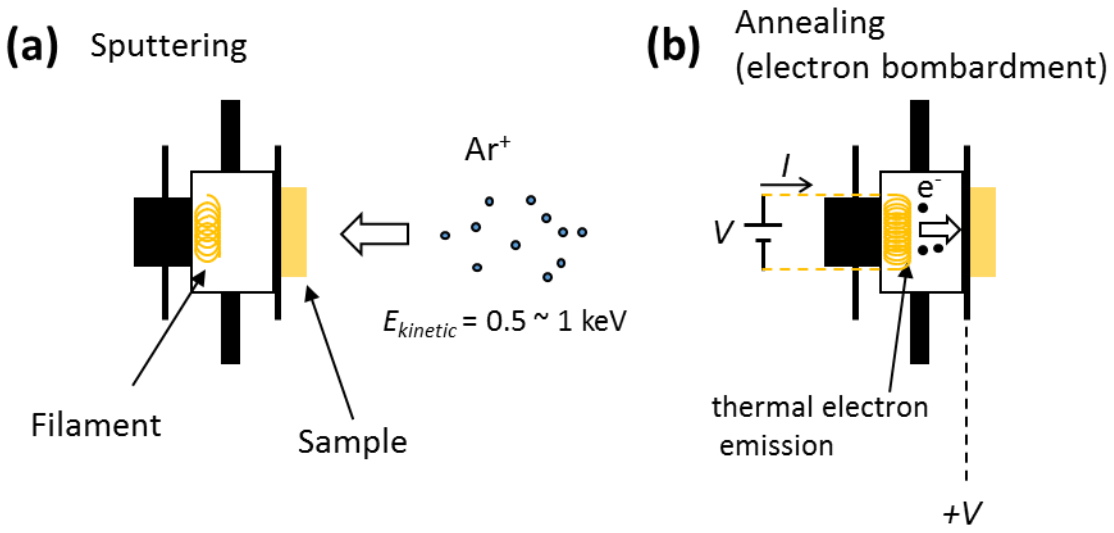

Fig. 2.17. (a) Schematic picture of the Ar^+ ion sputtering. Ionized Ar atoms are accelerated by electric fields (500 ~ 1000 V). (b) Schematic picture of the annealing by the electron bombardment. Hot electrons emitted from the filament are accelerated by the bias voltage applied at the sample.

Pb(111) sample holder. The sample holder was installed in a small vacuum chamber. The temperature near the Pb(111) single crystal was measured under a certain filament current. We determined the filament current required to the annealing, where the annealing temperature was selected at 430 K to avoid melting the sample.

2.5.2 Deposition of Molecules and Silicon Atoms

We use two molecules C_{60} and FePc. These molecules (powdery reagent) were commercially purchased. The deposition of the molecules were performed by the vacuum evaporation method, schematically shown in Fig. 2.18. The ceramic cells filled by C_{60} and FePc were heated by the filament. The molecules are evaporated and adsorb on the substrate. The K-type thermocouple is connected at the bottom of the cell. The temperature during the deposition is 600 K for C_{60} and 560 K for FePc. During the deposition, both Pb(111) and Au(111) substrates were kept at room temperature.

Silicene nano ribbons were *in-situ* synthesized on Ag(110) by depositing Si atoms from the electrically heated Si wafer. The temperature of the Si wafer is about 1500 K. The Ag(110) substrate was slightly heated (below 500 K) during the Si deposition.

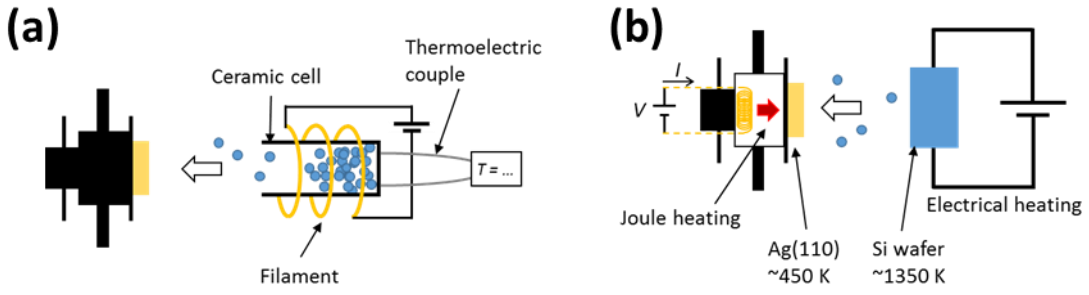

Fig. 2.18. Schematic pictures of (a) deposition of molecules and (b) deposition of silicon atoms.

2.5.3 Preparation of STM Tip

The superconducting STM tip was made by Nb. In order to avoid the oxidation of Nb, which destroys the superconductivity of Nb, the Nb tip was prepared by cutting a Nb wire mechanically in the UHV chamber[23], as shown in Fig. 2.19(a).

In the experiments on SiNR and FePc, we used a W tip. The W tip was prepared by the electrochemical etching of a W wire, as shown in Fig. 2.19(b). The W wire is dipped in NaOH aq (concentration is 2 M). A bias voltage is applied between the W wire and the loop shape Pt electrode. W atoms dissolved into the solution due to the electrochemical reaction. The electrochemical reaction occurs intensively at the liquid-air interface. As the reaction proceeds, the radius of the W wire at the liquid-air interface decreases, and the W wire is elongated by its own weight. Finally, the W wire is broken and a sharp tip is obtained. The obtained W tip is installed into the vacuum chamber.

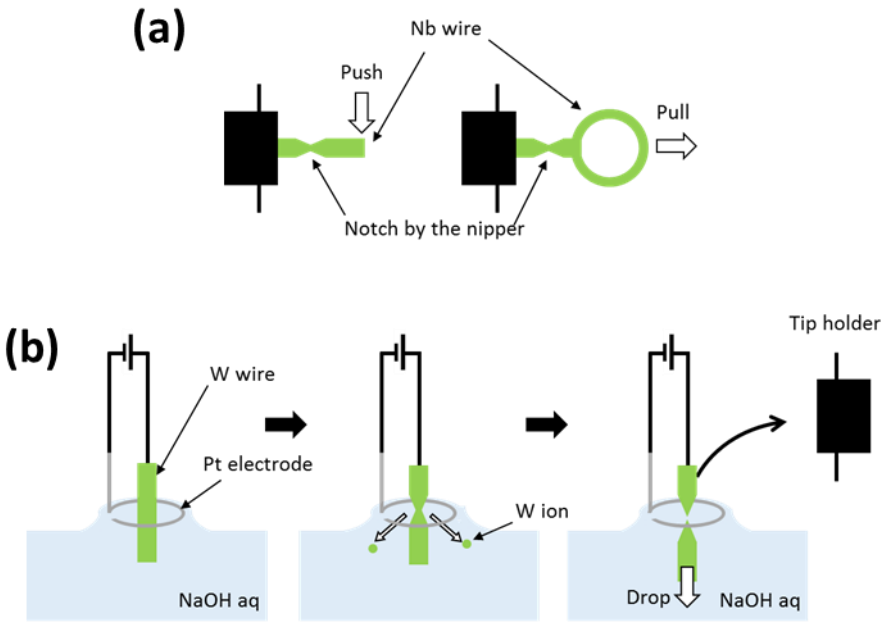

Fig. 2.19. Schematic pictures of the STM tip preparation. (a) Mechanical breaking of the Nb wire. (b) Electrochemical etching of W wire.

The spatial resolutions and the stabilities of both Nb and W tips were testified by acquiring STM images and STS spectra of the standard sample [we use Au(111)]. The oxidized layers and impurities residing at the tip surface as well as the non-ideal atomic structure of the tip apex cause the bad spatial resolution and irregular structures in the STS spectra. As mentioned around Eq. (2.19), it is preferable that the LDOS shape of the STM tip is a simple metallic shape which can be regarded as constant around the E_F because the LDOS of the STM tip also affect the STS spectra. In order to remove the contaminations and obtain the clean STM tip which has the high spatial resolution and produces reliable STS spectra, tip treatments were performed in the STM measurements on Au(111). In the tip treatment, we first applied negative bias voltage pulses to the STM tip to induce the field evaporation of the atoms at the tip apex [Fig. 2.20(b)]. After several voltage pulses were applied, we also testified the sharpness of the STM tip by softly touching the surface with the STM tip [Fig. 2.20(c)]. In this process, a metallic wire is formed between the STM tip and sample and is broken by the tip retraction, in the same way of the MCBJ method[24,25]. A protrusion formed at the surface after the STM tip contact reflects the sharpness of the STM tip apex. Note that this procedure may cause the reconstruction of the atomic structure of the tip apex. After this treatment, we checked the STM images and STS spectra to judge whether the tip treatment should be continued or finished.

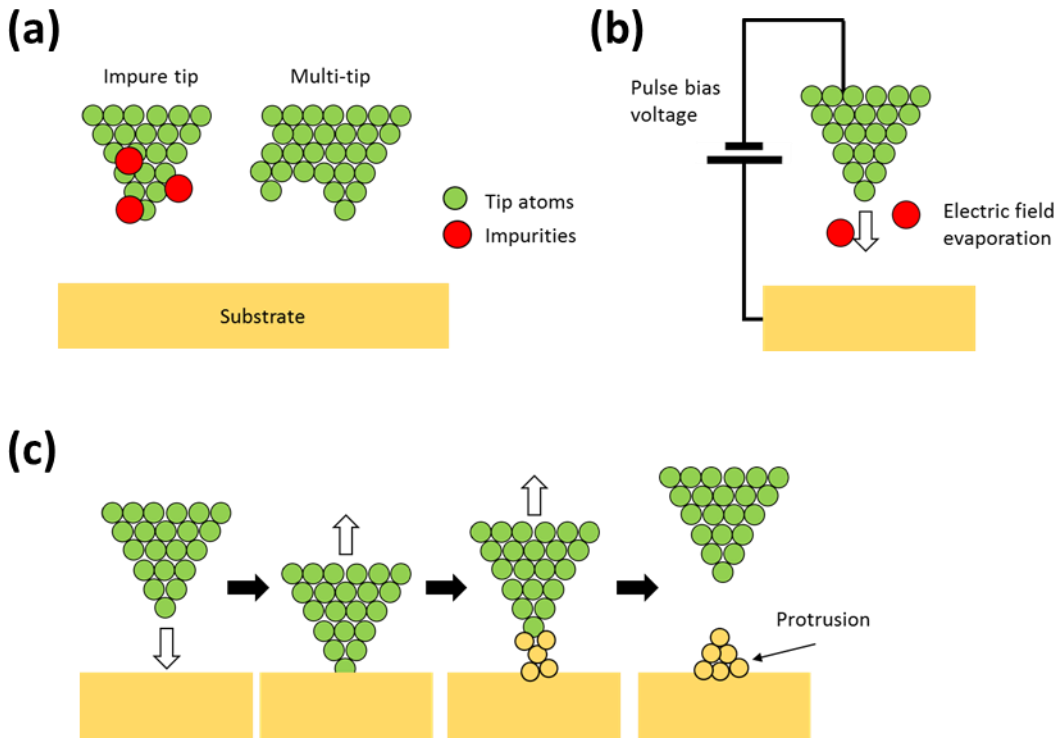

Fig. 2.20. (a) Schematic pictures of the STM tip which are not ideal for STM measurements. (b) Tip treatment by applying pulse bias voltage. (c) Tip treatment by contacting to the substrate.

References

[1] R. Holm, “The Electric Tunnel Effect across Thin Insulator Films in Contacts”, J. Appl. Phys. **22,** 569 (1951).

[2] R. Young, J. Ward, and F. Scire, “Observation of Metal-Vacuum-Metal Tunneling, Field Emission, and the Transition Region”, Phys. Rev. Lett. **27,** 922 (1971).

[3] J. Bardeen, “Tunneling From a Many-Particle Point of View”, Phys. Rev. Lett. **6,** 57 (1961).

[4] J. Tersoff, and D. R. Hamann, “Theory of the scanning tunneling microscope”, Phys. Rev. Lett. **50,** 1998 (1983).

[5] J. Tersoff, and D. R. Hamann, “Theory of the scanning tunneling microscope”, Phys. Rev. B **31,** 805 (1985).

[6] S. Ohnishi, and M. Tsukada, “Effect of the microscopic electronic states of the tip on the scanning tunneling microscopy image”, J. Vacuum Science and Technology A **8,** 174 (1990).

[7] M. Tsukada, K. Kobayashi, and S. Ohnishi, “Firstprinciples theory of the scanning tunneling microscopy simulation”, J. Vacuum Science and Technology A **8,** 160 (1990).

[8] N. Isshiki, K. Kobayashi, and M. Tsukada, “Effect of electronic states of the tip on the STM image of graphite”, Surf. Sci. Lett. **238,** L439 (1990).

[9] N. D. Lang, “Spectroscopy of single atoms in the scanning tunneling microscope”, Phys. Rev. B **34,** 5947 (1986).

[10] J. A. Stroscio, R. M. Feenstra, and A. P. Fein, “Electronic Structure of the Si(111)2 x 1 Surface by Scanning-Tunneling Microscopy”, Phys. Rev. Lett. **57,** 2579 (1986).

[11] R. M. Feenstra, J. A. Stroscio, and A. P. Fein, "Tunneling Spectroscopy of the Si(111)2 x 1 Surface", Surface Science **181,** 295 (1987).

[12] B. C. Stipe, M. A. Rezaei, and W. Ho, "Single-Molecule Vibrational Spectroscopy and Microscopy", Science **280,** 1732 (1998).

[13] L. Vitali, M. A. Schneider, K. Kern, L. Wirtz, and A. Rubio, "Phonon and plasmon excitation in inelastic electron tunneling spectroscopy of graphite", Phys. Rev. B **69,** 121414 (2004).

[14] A. J. Heinrich, J. A. Gupta, C. P. Lutz, D. M. Eigler, "Single-Atom Spin-Flip Spectroscopy", Science **306,** 466 (2004).

[15] J. Klein, A. Léger, M. Belin, D. Défourneau, and M. J. L. Sangster, "Inelastic-Electron-Tunneling Spectroscopy of Metal-Insulator-Metal Junctions", Phys. Rev. B **7,** 2336 (1973).

[16] W. Haiss, C. Wang, I. Grace, A. S. Batsanov, D. J. Schiffrin, S. J. Higgins, M. R. Bryce, C. J. Lambert, and R. J. Nichols, "Precision control of single-molecule electrical junctions", Nature materials **5,** 995 (2006).

[17] G. Schull, T. Frederiksen, A. Arnau, D. Sánchez-Portal, and R. Berndt, "Atomic-scale engineering of electrodes for single-molecule contacts", Nature Nanotechnology **6,** 23 (2011).

[18] G. Kresse, and J. Furthmüller, "Efficiency of ab-initio total energy calculations for metals and semiconductors using a plane-wave basis set", Comput. Mater. Sci. **6,** 15 (1996).

[19] G. Kresse, and J. Furthmüller, "Efficient iterative schemes for ab initio total-energy calculations using a plane-wave basis set", Phys. Rev. B **54,** 11169 (1996).

[20] P. Hohenberg, and W. Kohn, “Inhomogeneous Electron Gas”, Phys. Rev. **136,** B864 (1964).

[21] W. Kohn, and L. J. Sham, “Self-Consistent Equations Including Exchange and Correlation Effects”, Phys. Rev. **140,** A1113 (1965).

[22] T. Tsuneda, “Density Functional Theory in Quantum Chemistry”, Springer (2014), (ISBN: 978-4-431-54824-9).

[23] A. Kohen, Y. Noat, T. Proslier, E. Lacaze, M. Aprili, W. Sacks, and D. Roditchev, “Fabrication and characterization of scanning tunneling microscopy superconducting Nb tips having highly enhanced critical fields”, Physica C **419,** 18 (2005).

[24] J. I. Pascual, J. Méndez, J. Gómez-Herrero, A. M. Baró, N. García, and V. T. Binh, “Quantum contact in gold nanostructures by scanning tunneling microscopy”, Phys. Rev. Lett. **71,** 1852 (1993).

[25] L. Kuipers, M. S. Hoogeman, and J. W. M. Frenken, “Jump to contact and neck formation between Pb surfaces and a STM tip”, Surface Science **340,** 231 (1995).

Chapter 3
Electron Transport of Fullerene (C_{60})

3.1 Introduction

We briefly describe the purpose of this study again. Our purpose is that experimentally determining the electron transport characteristics (the number of transport channel n and their transmission coefficients τ) of the single molecular junction. Furthermore, we have to unveil the role of the contact state; the energy level alignment of the molecule and the geometrical configuration of the molecule.

We studied the fullerene (C_{60}) molecular junction with the superconducting Pb(111) substrate and Nb tip. We constructed the superconducting Nb tip-C_{60}-Pb(111) junction and observe the subharmonic gap structure (SGS) in the I-V spectra caused by the multiple Andreev reflection (MAR).

The contents of this chapter is published in Phys. Rev. B **90,** 241405 (2014) [R. Hiraoka *et al.*].

3.2 Clean Pb(111) substrate

Figures 3.1(a) and (b) show STM topographic images of the bare Pb(111) substrate. Atomically flat surface is obtained as shown in these STM topographic images[1]. The line profile along the purple line in Fig. 3.1(a) is shown in Fig. 3.1(c). The step height is 300 pm, which corresponds to the monoatomic step of the Pb(111) surface (the atomic

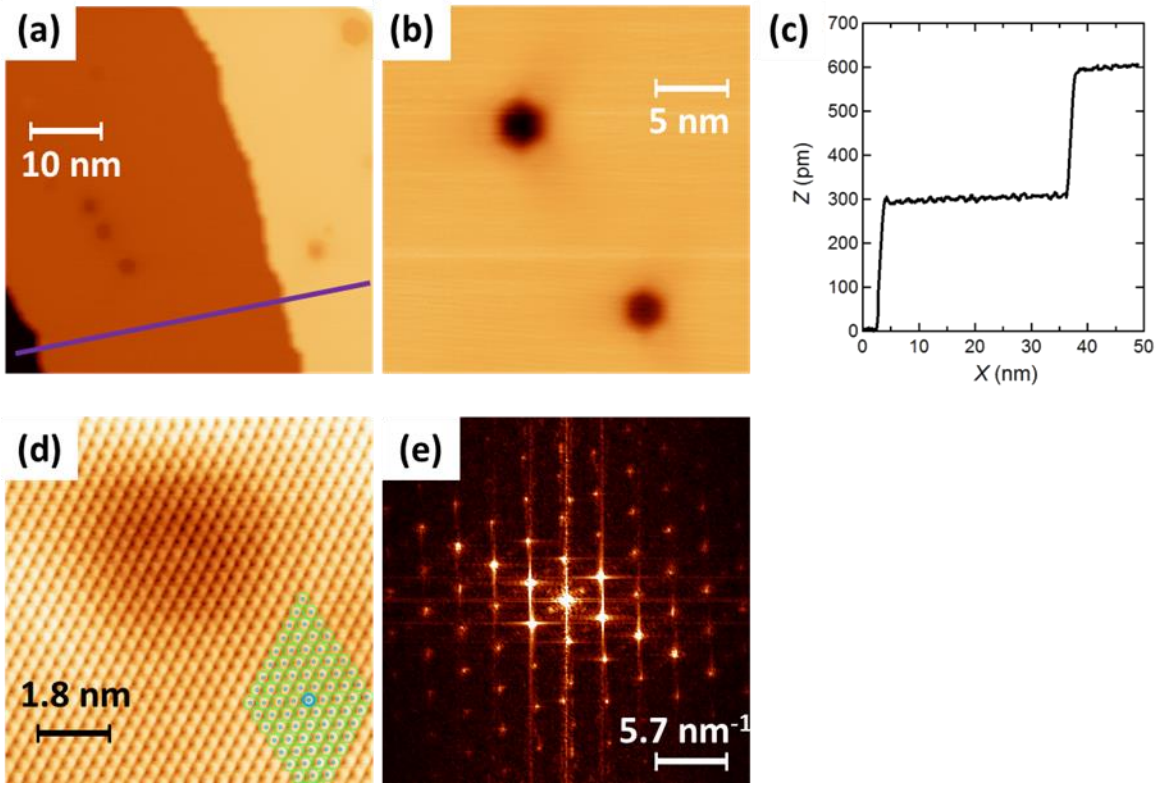

Fig. 3.1. (a) STM image of the clean Pb(111) substrate. The image size is 50 nm x 50 nm and the set points are I_t = 100 pA and V_S = -0.1 V. (b) Closed-up STM image of the bare Pb(111) substrate. The image size is 25 nm x 25 nm and the set points are I_t = 50 pA and V_S = -0.3 V. (c) Line profile across the purple line in (a). The steps with the height difference 300 pm are the single atomic steps of the Pb(111) surface. (d) STM image of Pb(111) with the atomic resolution. The set points are I_t = 1 μA and V_S = 50 mV. The green circles represent the hexagonal lattice with the lattice constant 0.353 nm. (e) 2D-FFT image of (d). The spot distance is about 3.1 nm^{-1}, which corresponds with the size of the Pb atom.

radius of Pb is 175 pm). Hexagonal defects are observed in the STM images. The depth of the defects are 160 ~ 190 pm under the sample bias V_S = 50 ~ 500 mV. Fig. 3.1(d) shows the STM image with the atomic resolution. The green circles represent a hexagonal lattice with the size 0.353 nm, which is the size of the Pb atom. Fig. 3.1(e) is the 2D-FFT image of Fig 3.1(d). The distance of the spots is about 3.1 nm^{-1}, yielding the lattice size 0.32 nm. In the atomic resolution image, there are no boundaries between the defect region (dark region) and the bright region. Hence, the defect is expected to be caused by a defect beneath the first layer.

Figures 3.2(a) and (b) show STS spectra obtained on Pb(111). The wide range spectra in Fig. 3.2(a) shows a typical featureless character of metallic samples. In the narrow range spectra [Fig. 3.2(b)], the superconducting gap structure is observed at around the E_F. The green curve is a fitting result of the Dynes function;

$$D(E,\Delta,\Gamma) = \mathrm{Re}\left[\frac{E - i\Gamma}{\sqrt{(E - i\Gamma)^2 - \Delta^2}}\right],$$

where Δ is the superconducting gap energy and Γ is the broadening parameter. The fitting parameters are Δ = 1.36 meV, Γ = 0.15 meV, which is in good agreement of the bulk value $\Delta_{\text{Pb-bulk}}$ = 1.36 meV. Step structures at $V_S = \pm$ 4.5 mV is a signature of the phonon excitation of Pb (longitudinal acoustical mode)[2].

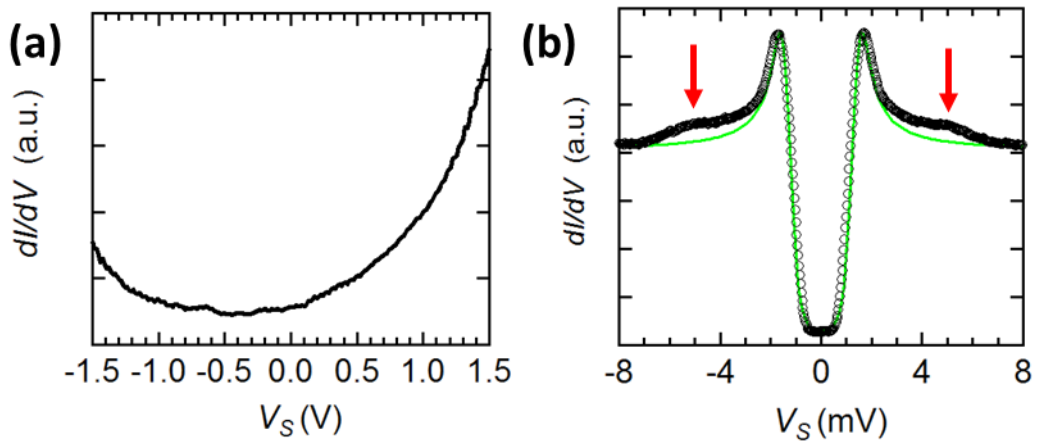

Fig. 3.2. (a) Wide range STS spectra of Pb(111) obtained at T = *6.0* K. The set points are I_t = 100 pA and V_S = -0.5 V and the lock-in modulation V_{rms} = 12 mV. (b) Narrow range STS spectra of Pb(111) obtained at T = 0.4 K. The set points are I_t = 400 pA and V_S = -50 mV and the lock-in modulation V_{rms} = 0.04 mV. The Green solid curve is the fitting of the dynes function convolved with the lock-in instrumental function: Δ = 1.36 meV and Γ = 0.15 meV.

3.3 Adsorption of C_{60} on Pb(111)

Figures 3.3(a) and (b) show an STM topographic image of C_{60} / Pb(111). Each bright round shape corresponds to the single C_{60} molecule. C_{60} molecules form hexagonal islands. The lattice constant of the hexagonal island is approximately 1.0 nm, which well accords with the previous STM work of C_{60} / Pb(111)[3,4]. In this study, we focused on the molecules at the island edge for the stable contact measurement. As indicated by white arrows in the STM image, C_{60} molecules at the edge are observed as two different shapes: round and two-lobed shapes. Hereafter, we call the round and two-lobed shape molecules as α- and β-type molecules, respectively. The intra-molecular structure reflects the spatial distribution of molecular orbitals.

The estimated adsorption configurations are schematically shown in Fig. 3.3(c). According to the previous works, the intra-molecular structure reflects the spatial distribution of LUMO states of C_{60}[5,6]. Figures 3.4(a) and (c) show the STM images of C_{60} on Ag(110)[5] and Au(111)[6]. Calculation results on free C_{60} shows that the L DOS contour surface of the LUMO states is distributed around the pentagonal rings of C_{60}. STM images in Fig. 3.4(a) and (c) clearly show that we can estimate the molecular configurations from the STM images. We estimate the molecular orientation from the STM images as follows; the α-type molecule is bonded to Pb(111) through one of the pentagonal rings and the pentagonal ring faces towards the vacuum, while the β-type molecule is adsorbed through a single carbon atom and the node appears in the image.

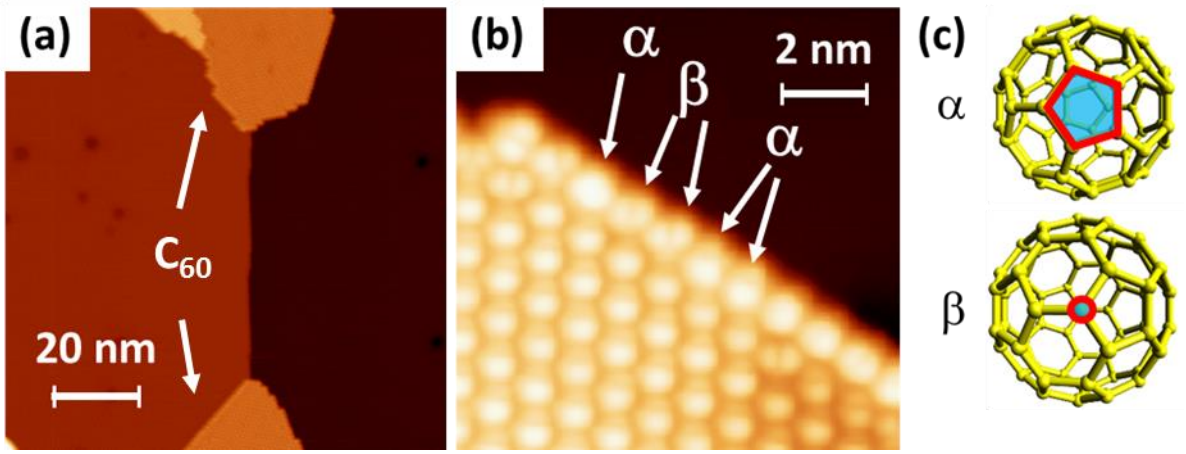

Fig. 3.3. (a) STM image of C_{60} islands on Pb(111). The image size is 100 nm x 100 nm and the set points are I_t = 50 pA and V_S = 1.0 V. (b) Closed-up STM image of the bare Pb(111) substrate. The set points are I_t = 100 pA and V_S = -50 mV. (c) Schematic picture of the molecular configurations (α and β). The red lines represent the upper face; α-molecules direct their pentagonal rings towards the vacuum (STM tip) and β-molecules direct their carbon atom.

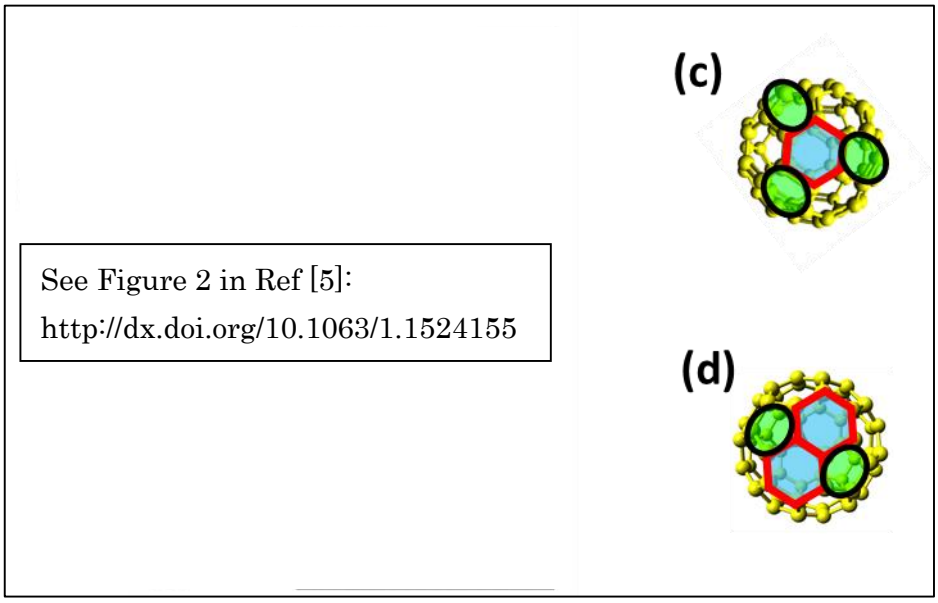

Fig. 3.4. (a) Calculated LDOS contour surface of the free C_{60} molecule with different angles (left) and STM images of C_{60} on Ag(110) (right) (adopted from ref. [5]). The top faces of the C_{60} molecules are (a) the hexagonal ring and (b) the bond between the two hexagonal rings. (c),(d) Schematic models of C_{60} molecular configurations in (a) and (b). The blue hexagons and green circles represent the hexagonal rings and pentagonal rings of C_{60}.

3.4 STM Contact Measurement of C_{60}

Figures 3.5(a) and (b) show typical conductance traces called *G-Z* curve. Both in Fig. 3.5(a) and (b), *G* increases logarithmically as the tip approaches the surface (as *Z* increases) denoted by black and blue circles, which reflects the vacuum tunneling situation. Then the slope of the *G-Z* curve gradually decreases at around $G = 0.2\ G_0$ and *G* approaches to a saturated value. In the measurement in Fig. 3.5(a), the STM tip was retracted at around $Z = 0.23$ nm and $G = 0.26\ G_0$, and the *G-Z* curve of the retracting process denoted by red circles travels almost same way of the approach process. In the measurement in Fig. 3.5(b), *G* increases at around $0.5 G_0$ in the end of the approaching process. In this case, the tip crashed into the sample surface and the molecular array are broken, as shown in the right panel of Fig. 3.5(c), which is the STM topographic images obtained after the contact measurement. The *G-Z* curve fluctuates largely during the retracting process, shown in Fig. 3.5(b) as the pink circles. This represents the formation and breaking of the atomic wire in the STM (tip-substrate) junction. In contrast, when $G < 0.5\ G_0$ during the STM contact measurement, there appeared no drastic changes in the STM topographic images obtained before and after the contact measurement, which indicates the successful formation of the molecular junction without damaging both tip and sample. In the previous studies, the conductance of a single C_{60} molecule has been measured by STM contact measurement[7-9] and also the MCBJ technique[10,11]. The conductance of the single C_{60} junction is ~ $0.2\ G_0$. We conclude that a stable C_{60} junction, where the electrodes are Nb tip and Pb(111) substrate, is constructed when $0.2\ G_0 < G < 0.5\ G_0$. Therefore, we measured *I-V* spectra of the C_{60} junction at $0.29 \sim 0.30\ G_0$.

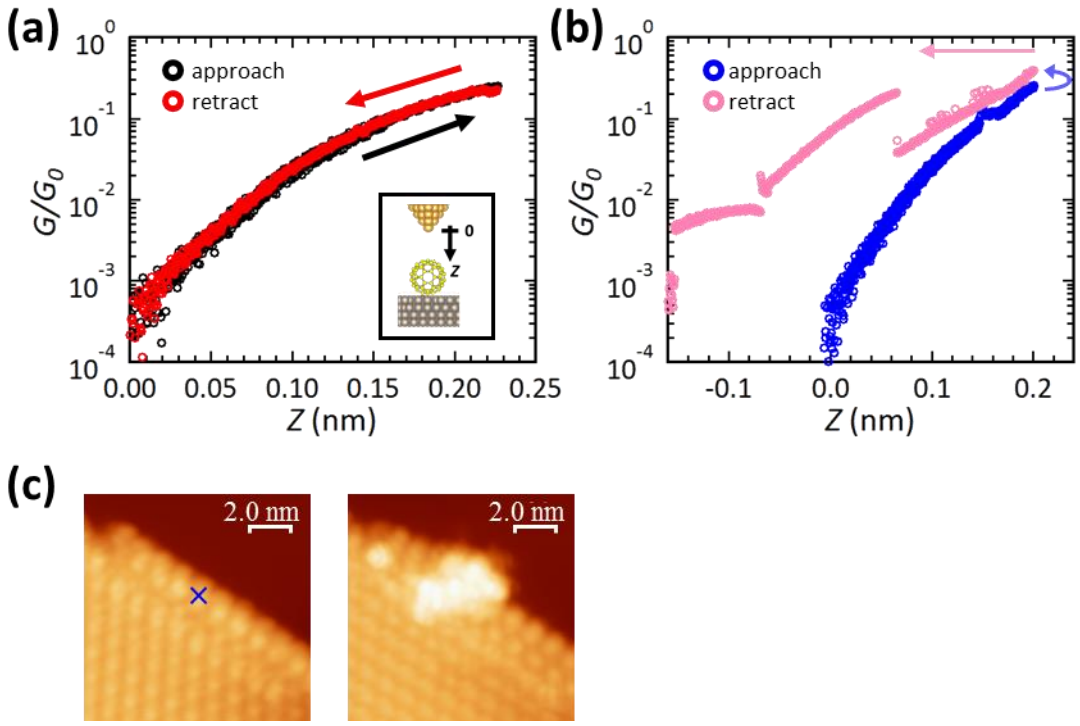

Fig. 3.5. (a) *G*-*Z* curve of the C_{60} junction. The black and red circles represent the approaching and retracting process. The inset shows a schematic picture of the junction measurement. (b) *G*-*Z* curve of the C_{60} junction when the STM tip breaks the surface. (c) STM topographic images obtained before (left) and after (right) the junction measurement in (b). The blue cross in the left image is the initial position of the STM tip.

As mentioned, we constructed the single C_{60} junction for the molecules at the molecular island edge in order to construct the stable molecular junction. It was difficult for us to manipulate the molecules to make an isolated C_{60} by the Nb tip. Strictly speaking, the electronic states of the molecule in the island should be slightly different from those of the isolated molecule. However, the effect is not serious; the LUMO and HOMO states may be shifted and broadened at a certain extent[12], yet, significant changes will not occur in this system, such as the original LUMO states move to the occupied region.

Figure 3.6 shows the STM images obtained before and after one STM contact measurement. The target molecule is denoted by the red broken circles. The molecular

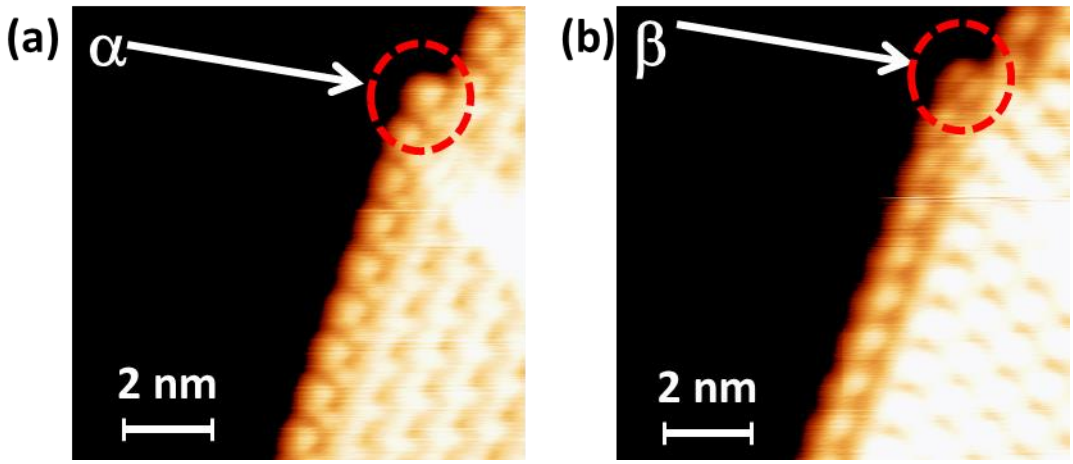

Fig. 3.6. STM images obtained (a) before and (b) after one STM contact measurement (set points are are I_t = 50 pA and V_S = -0.1 V). The red broken circles represent the target molecule of the STM contact measurement. The molecular configuration changes after the STM contact measurement.

configuration of only the target molecule changes (from α to β) after the STM contact measurement. These results demonstrate that the STM tip surely contact only the target molecule in this condition of the STM contact measurements. Hence, we conclude that the STM contact measurements probe the single molecule.

3.5 I-V Characteristic of C_{60} Junction

Figure 3.7 shows four *I*-*V* spectra of junctions obtained at T = 400 mK. The *I*-*V* spectra of the single molecular junction of the α- and β-type C_{60} are presented in Figs. 3.7(a) and (b), respectively. In Figs. 3.7(c) and (d), the *I*-*V* spectra of (c) a metal nano junction formed by contacting the Nb tip to the bare Pb(111) substrate and (d) a tip-vacuum-substrate tunnel junction (i.e., the conventional STM geometry) are shown, respective ly. In Fig. 3.7(d), the almost zero current region below V = 2 mV indicates the superconducting gap region. In contrast to Fig. 3.7(d), step-like increases marked by gray

arrows appear inside the superconducting gap region (V< 3 mV) in Figs. 3.7(a), (b), and (c). These fine structures are the SGS produced by m = 2 and m = 3 MARs. The dotted vertical lines at V= 3 mV (eV= 2Δ = Δ_{tip} + $\Delta_{substrate}$) indicates the border between the MARs region and the outside of the superconducting gap, where the current increases linearly

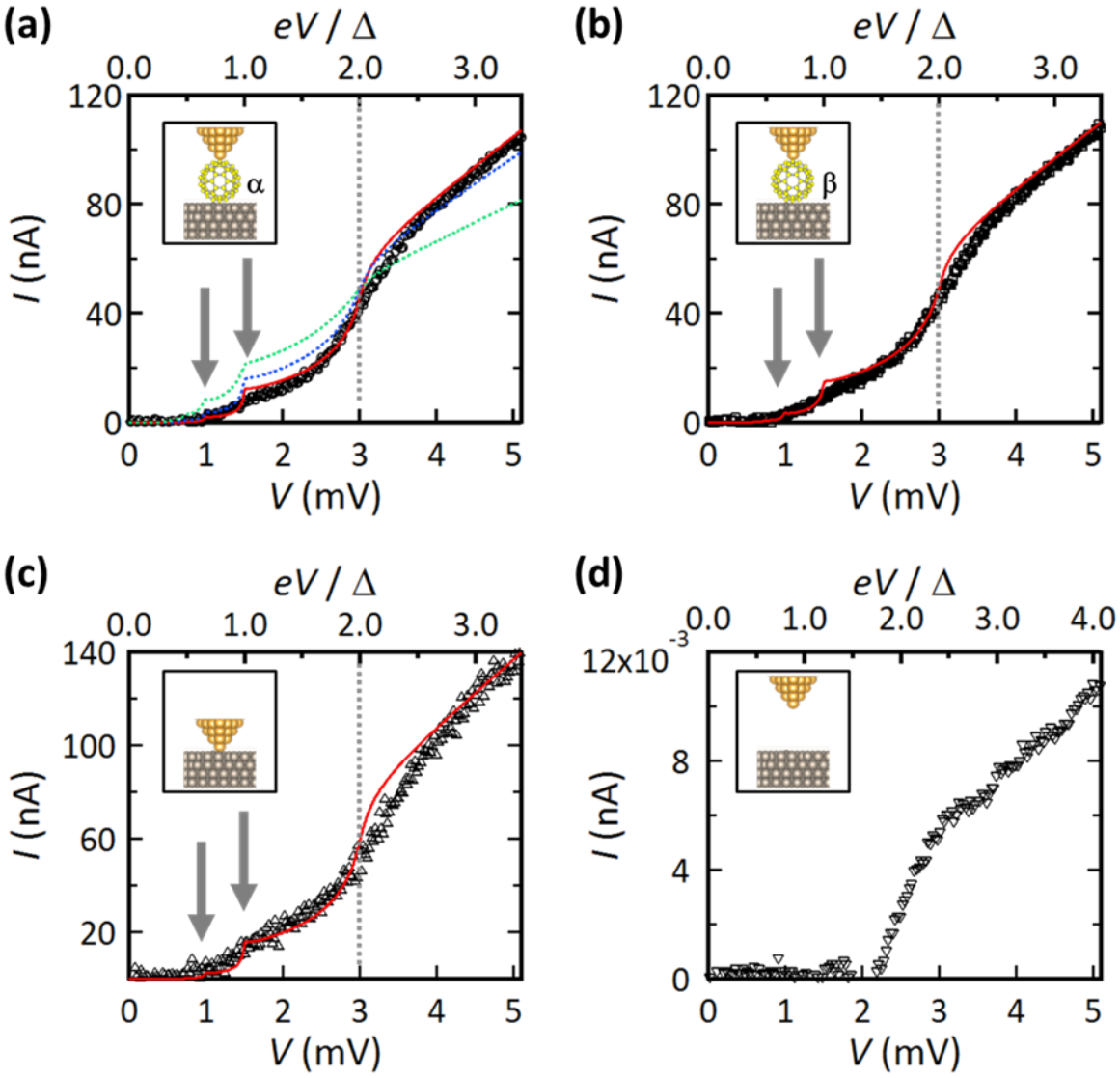

Fig. 3.7. (a) *I-V* spectra of the a-type C_{60} junction. (b) *I-V* spectra of the b-type C_{60} junction. (c) *I-V* spectra of the Nb tip - substrate metal nano junction. (d) *I-V* spectra of the tip - vacuum – substrate junction. The red curves in (a), (b) and (c) are the calculated best fit, where (a) τ_i = {0.095, 0.095, 0.095}, (b) τ_i = {0.17, 0.075, 0.06}, and (c) τ_i = {0.10, 0.09, 0.09, 0.09}. }. The green and blue dashed curves in (a) are the calculated spectra of n = 1 and n = 2 case, for reference: τ_i = {0.285} for n = 1 and τ_i = {0.1425, 0.1425} for n = 2.

with voltage.

Then, we explain the process of the analysis. Figure 3.8 shows the calculated spectra based on Eq. (1.8)[13] in Chapter 1. The total transmission coefficient of every spectrum is 0.3 and their distributions are different. Note that, the total value of the transmission coefficients are experimentally determined by the observed G [0.295 for the case of Fig. 3.7(a)] and the Landauer equation requests us to distribute the total value to several channels. In Fig. 3.8(a), we distribute the transmission coefficient equivalently to several channels (one to five channels), i.e., τ_i = (0.3), (0.15, 0.15), (0.1, 0.1, 0.1), (0.075, 0.075, 0.075, 0.075) and (0.06, 0.06, 0.06, 0.06, 0.06). As the number of the channel increases, the current of the SGS decreases and the current outside the superconducting gap region ($eV/\Delta > 2$) increases. In Fig. 3.8(b), we show the spectra with two channel case together with the one channel case. The black and red spectra show almost same curve. This is because the red spectrum can be regarded as the single channel case; the distribution of τ_i

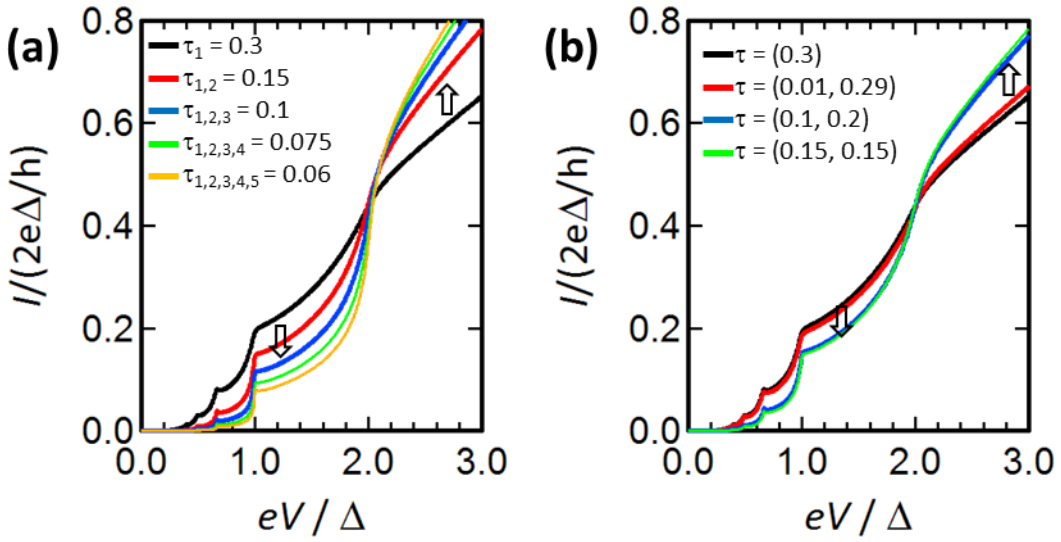

Fig. 3.8. (a) Calculated *I-V* spectra of the SGS. The total τ of all spectra is 0.3. The number of channels are one, two, three, four and five for the black, red, blue green and orange spectra, respectively. τ are distributed equivalently to the channels, i.e., the black spectrum is the result of one channel case with τ = 0.3, the red spectrum is two channels with τ = (0.15, 0.15), and so on. (b) Calculated *I-V* spectra of the SGS with various distributions of τ.

for the red spectrum is (0.29, 0.01), where there are one dominant channel and small second channel. As the distribution of τ into two channels becomes equivalent, the current of the SGS decreases and the current outside the superconducting gap region increases. According to these spectral characters of SGS, we can evaluate the number of channels *n* and the transmission coefficients τ_i by reproducing the current of both the SGS and the outside the superconducting gap region.

The red curves in Figs. 3.7(a)-(c) are the calculated best fittings. For reference, the curves calculated for $n = 1$ and $n = 2$ are also shown in Fig. 3.7(a). We determine *n* and τ_i uniquely as follows: $n = 3$ and $\tau_i = \{0.095 \pm 0.03, 0.095 \pm 0.03, 0.095 \pm 0.03\}$ for the α-type C_{60} junction, $n = 3$ and $\tau_i = \{0.17 \pm 0.02. 0.075 \pm 0.02, 0.06 \pm 0.02\}$ for the β-type C_{60} junction; $n = 4$ and $\tau_i = \{0.10 \pm 0.03, 0.09 \pm 0.03, 0.09 \pm 0.03, 0.09 \pm 0.03\}$ for the metal nano junction in Fig. 3.7(c). We show only the $n = 1 \sim 3$ case in Fig. 3.7(a). In order to fit the result by four channels, τ of the 4^{th} channels should be very small value, as shown by the black and red spectra in Fig. 3.8(b); we can reproduce the curve of the one channel case by the two channel case when we distribute τ into the dominant τ_1 and small τ_2.

We ignored the asymmetry of the electrodes and the broadening effects in the analysis. In the theoretical representation in Eq. (1.8), both electrodes are assumed to be identical. We used an averaged superconducting gap in the analysis: $\Delta = [\Delta_{tip} + \Delta_{substrate}] / 2 = 1.5$ meV. We also assumed a BCS-type DOS for the superconducting electrodes without considering the lifetime smearing of the electronic structure. We have investigated the broadening effect by artificially introducing the broadening as shown in Fig. 3.9. In Fig. 3.9, we show the spectrum identical to that of Fig. 3.7(a). The black circles are the experimental result and the red solid curve is the best fit result with three channels. We introduce a nominal broadening into the red solid curve by convolving the Gaussian whose peak width is set such that the broadening energy is 2.0 meV. The green curve is the result of the convolution. The green curve shows better reproducibility than the red solid curve. As

stated, the origins of the broadening are the smearing of the superconductivity of the electrodes, the fact that we used the same superconducting gap parameter for both tip and substrate. Although the better fitting result is obtained, we have analyzed without broadening effects for the sake of brevity, rather than artificially introducing the broadening. We believe that the fitting calculations well reproduced the experimental results with a sufficient accuracy. The transport characteristics n and τ_i of the C_{60} molecular junction are determined by these results.

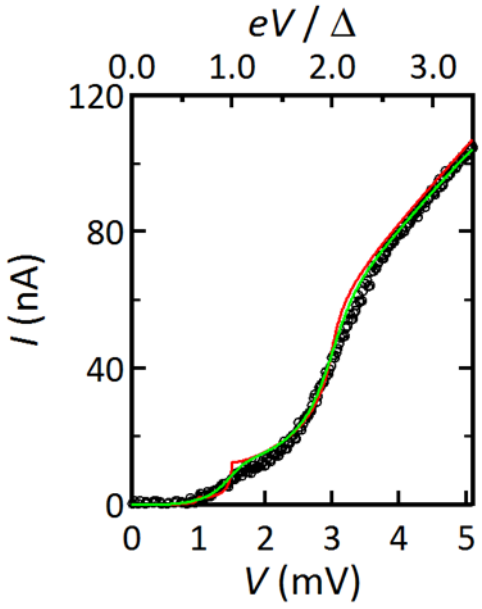

Fig. 3.9. *I-V* spectra of the α-type C_{60} junction (black circles) and the best fitting result (red curve), which are identical to those of Fig. 3.7(a). The green solid curve is calculated from the red curve by convolving Gaussian function of the broadening energy 2.0 meV.

3.6 Electronic States of C_{60} on Pb(111)

From STS spectra of the α- and β-type C_{60} molecules, we can understand the origin of the transport channels and the number of the transport channels. Figure 3.10 shows STS spectra of the α- and β-type C_{60} molecules. The peak structures around 100 ~ 200 meV are the LUMO derived resonances of the C_{60} molecule which are triply-degenerate in the gas phase[14]. In the STS, there seems two peaks at the LUMO derived resonances, which indicates that the degeneracy is partially lifted by the molecule-substrate interactions[3]. In contrast to the LUMO derived resonances, the peaks corresponding to the occupied MOs do not appear in the measured energy range (-1.5 to 0 V) and the increase of the spectral intensity observed at -1.5 V reflects the tails of the molecular resonances. We can conclude that, as far as the bias voltage is low, the LUMOs of C_{60} are responsible for the electronic transport through the C_{60} molecule because the electronic

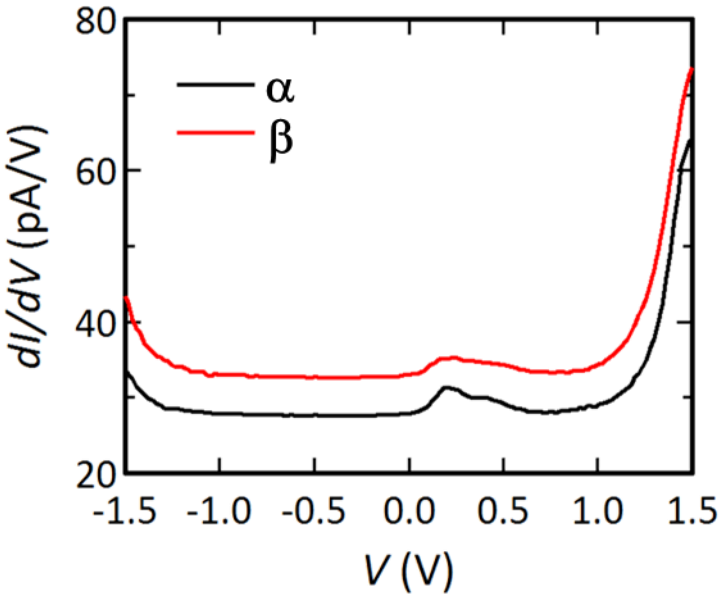

Fig. 3.10. STS spectra of the α- and β-type C_{60} molecules on Pb(111) obtained at T = 2.7 K: the set points V_b = 0.5 V and I_t = 70 pA. An ac modulation voltage V_{mod} = 16 mV(rms) was applied for the lock-in measurement. The spectrum of β-type C_{60} is vertically offset for clarity.

states near the E_F is important in this bias voltage region and the contributions from the occupied MOs are negligible. The number of transport channels (n = 3) is in good accordance with the number of the LUMOs of C_{60}. In addition, this result justifies the theoretical studies reporting that the LUMOs of C_{60} provide the dominant channel for electronic transport of the C_{60} junction[15,16]. Figure 3.11 shows the model structure of the Al-C_{60}-Al junction. The electronic states of this system is calculated in the framework of DFT and the transmission coefficients are calculated by the Green's function in Ref [16]. It has revealed that three channels derived from three LUMO states of C_{60} contribute to the electron transport at around the E_F, not five channels arising from the HOMO states of C_{60}. Although STS spectra do not strictly represent the electronic structure of the single molecular junction because STS spectra are measured in the conventional vacuum tunneling regime (the STM tip does not in contact with the molecule), the electronic structure is expected not to be significantly change by the tip contact, as calculation results indicate. Therefore, we conclude that the determined number of transport channels is valid and our results fully justify the theoretical prediction that the number of MOs near the E_F determines the number of dominant transport channels[17,18].

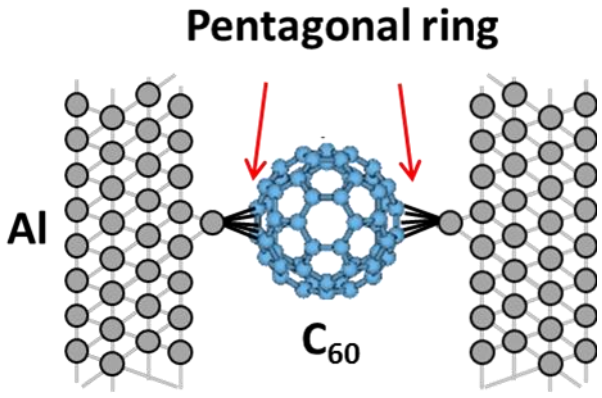

Fig. 3.11. (a) Model structure of the C_{60} molecular junction with Al electrodes. The single Al atoms of both electrodes connect with the pentagonal rings of the C_{60} molecule. (see Ref. [16].)

Finally, we will examine the relation between transmission coefficients and the molecular configuration. The transmission coefficients of the α-type C_{60} junction are different from those of the β-type C_{60} junction, though the STS spectra are very similar. Each transmission coefficient of the α-type C_{60} junction is almost same, i.e., the three channels equally contribute to the total conductance. In contrast, the β-type C_{60} junction shows one channel larger than the others. At present, we do not have a definitive and quantitative explanation for this difference, however, we can provide a reasonable guess for the origin of this difference in terms of the molecular orientations. The tip contact position for the α-type C_{60} junction is the pentagonal ring, where three LUMO states spread uniformly. Meanwhile, the position for the β-type C_{60} junction is the C atom, where a node of the LUMO is located. We believe that the spatial distribution of the MO relative to the electrode is the origin of the different electronic transport characteristics, i.e., the molecular configuration with respect to the electrodes determines the magnitude of the contributions from each channel.

3.7 Conclusion

We determined the number of the transport channels (n) and the transmission coefficients (τ) of the C_{60} junction by measuring the current signal (subharmonic gap structure) of the multiple Andreev reflection (MAR) in the I-V spectra with STM. We found that three different channels exist in the C_{60} junction (n = 3) and that the transmission coefficients depend on the molecular orientation. According to STS spectra, the LOMOs of C_{60} are responsible for the dominant electron transport channels, providing the three transport channels. This result supports the theoretical studies. We also

conclude that the spatial distributions of the molecular orbitals are responsible for the different electron transport characteristics (different τ) in the different molecular orientations.

References

[1] S. Speller, W. Heiland, A. Biedermann, E. Platzgummer, C. Nagl, M. Schmid, and R. Varga, "An STM study of the step structure of Pb (110) and Pb (111)", Surface Science **331-333,** 1056 (1995).

[2] O. Naaman, W. Teizer, and R. C. Dynes, "The fabrication of reproducible superconducting scanning tunneling microscope tips", Review of Scientific Instruments **72,** 1688 (2001).

[3] G. Schulze, K. J. Franke, and J. I. Pascual, "Resonant heating and substrate-mediated cooling of a single C_{60} molecule in a tunnel junction", New Journal of Physics **10,** 065005 (2008).

[4] H. I. Li, K. J. Franke, J. I. Pascual, L. W. Bruch, and R. D. Diehl, "Origin of Moiré structures in C_{60} on Pb(111) and their effect on molecular energy levels", Phys. Rev. B **80,** 085415 (2009).

[5] J. I. Pascual, J. Gómez-Herrero, D. Sánchez-Portal, H. -P. Rust, "Vibrational spectroscopy on single C_{60} molecules: The role of molecular orientation", J. Chem. Phys. **117,** 9531 (2002).

[6] X. Lu, M. Grobis, K. H. Khoo, S. G. Louie, and M. F. Crommie, "Charge transfer and screening in individual C60 molecules on metal substrates: A scanning tunneling spectroscopy and theoretical study", Phys. Rev. B, **70,** 115418 (2004).

[7] N. Néel, J. Kröger, L. Limot, T. Frederiksen, M. Brandbyge, and R. Berndt, "Controlled Contact to a C_{60} Molecule", Phys. Rev. Lett. **98,** 065502 (2007).

[8] N. Néel, L. Limot, J. Kröger, and R. Berndt, "Rotation of C_{60} in a single-molecule contact", Phys. Rev. B **77,** 125431 (2008).

[9] G. Schull, T. Frederiksen, A. Arnau, D. Sánchez-Portal, and R. Berndt, "Atomic-scale engineering of electrodes for single-molecule contacts", Nature Nanotechnology **6,** 23 (2011).

[10] M. Kiguchi and K. Murakoshi, "Conductance of Single C_{60} Molecule Bridging Metal Electrodes" J. Phys. Chem. C **112,** 8140 (2008).

[11] M. Kiguchi, "Electrical conductance of single C_{60} and benzene molecules bridging between Pt electrode", Appl. Phys. Lett. **95,** 073301 (2009).

[12] I. F. Torrente, K. J. Franke, and J. I. Pascual, "Spectroscopy of C 60 single molecules: the role of screening on energy level alignment", J. Phys.: Condens. Matter **20,** 184001 (2008).

[13] E. N. Bratus', V. S. Shumeiko, and G. Wendin, "Theory of Subharmonic Gap Structure in Superconducting Mesoscopic Tunnel Contacts", Phys. Rev. Lett. **74,** 2110 (1995).

[14] M. R. Savina, L. L. Lohr, and A. H. Francis, "A particle-on-a-sphere model for C_{60}", Chem. Phys. Lett. **205,** 200 (1993).

[15] J. Taylor, H. Guo, and J. Wang, "Ab initio modeling of open systems: Charge transfer, electron conduction, and molecular switching of a C_{60} device", Phys. Rev. B **63,** 121104 (2001).

[16] N. Kobayashi, T. Ozaki, K. Tagami, M. Tsukada, and K. Hirose, "First-Principles Calculations of Quantum Transport in Single Molecule", Jpn. J. Appl. Phys. **45,** 2151 (2006).

[17] N. J. TAO, "Electron transport in molecular junctions", Nature Nanotechnology **1,** 173 (2006).

[18] J. P. Bergfield, J. D. Barr, and C. A. Stafford, “The number of transmission channels through a single-molecule junction”, ACS Nano **5,** 2707 (2011).

Chapter 4
Electron Transport of Silicene Nano Ribbon (SiNR)

In this digest version, the contents in this chapter is omitted, and will be published in an academic journal.

Chapter 5
Magnetic Properties of Iron(II) Phthalocyanine (FePc) Junction

In this digest version, the contents in this chapter is omitted, and will be published in an academic journal.

Chapter 6
Summary and Outlook

In this thesis, we have reported the results of three experiments; the STM contact measurements on (1) the fullerene (C_{60}) molecule, (2) the silicene nano ribbon (SiNR) and (3) the Iron(II) phthalocyanine (FePc) molecule.

(1) Electron Transport of C_{60}

In Chapter 3, we discussed the electron transport characteristics of the single molecule. Our purpose is not only to determine the two key parameters appearing in the Landauer formula, the number of the transport channels (n) and their transmission coefficients (τ), but also to investigate the relation between the parameters and the geometric and electronic configurations of the molecule. We have investigated the transport characteristics of C_{60} by utilizing the superconducting metal electrodes [Nb STM tip and Pb(111) substrate]. The subharmonic gap structure (SGS) was observed in the I-V spectra of the Nb-C_{60}-Pb junction caused by the multiple Andreev reflection (MAR). We found that three transport channels in the C_{60} junction (n = 3) and determined their transmission coefficients τ.

STS spectra indicate that the LOMOs of C_{60} (triply degenerated in the gas phase) serve as the three dominant electron transport channels, which well supports the theoretical studies. Moreover, we found that the transmission coefficients depend on the molecular orientation (α and β). We conclude that the spatial distributions of the molecular orbitals are responsible for the different electron transport characteristics (different τ) in the different molecular orientations, while the number of the molecular orbitals near the Fermi level determines the number of the transport channels (n = 3).

These results are the benefits of STM and STM contact measurements, where we can identify the geometric and electronic states of the single molecule.

We have demonstrated that STM using the superconducting tip and substrate provides an effective way to investigate the electron transport characteristics of a single molecule. STM contact measurement will provide the opportunities of further investigations such as the molecular junction which has a certain function as the single molecular device. For example, we can investigate the switching events of the conductance and the *I-V* characteristics of the single molecular junction in terms of the transport characteristics (n and τ). The mechanism of the switching function can be experimentally investigated, which may provide us further insight for the realization of the single molecular device.

(2) Electron Transport of SiNR

In Chapter 4, we focused on the electronic properties and the electron transport characteristics of silicene nano ribbon (SiNR). SiNR is expected to have many interesting physical properties beyond graphene, not only the edge state and Dirac electrons but also the topological edge state, which provides the spin dependent electronic properties. Although SiNR has the potential to contribute both academic and industrial fields, the electronic states of SiNR are still unveiled. One of the problems is that it is expected that Si and Ag strongly interacts, followed by the vanishment of the π-electron system in silicene.

We performed the STM contact measurement on SiNR on Ag(110). The single SiNR junction was constructed and the *I-V* characteristics of the junction were measured. *dI/dV* spectra of SiNR obtained when the STM tip lifted up the SiNR showed a sharp peak structure at the E_F, which is attributable to the edge state. We conclude that the edge state was clearly observed in the *dI/dV* spectra because the SiNR was decoupled from the

Ag substrate by the STM tip. In contrast, STS spectra obtained on SiNR showed no peak structure attributable to the edge state around the E_F. Moreover, the electronic states of SiNR on Ag(110) are almost identical to the bare Ag substrate. We conclude that the hybridization between SiNR and Ag(110) cause the vanishment of the electronic states unique to SiNR around the E_F.

We have demonstrated that the edge state of SiNR can revive when the interaction between SiNR and the substrate is reduced. Our experimental results support the approaches to realize the exotic electronic properties in the Si honeycomb materials by reducing the hybridization between silicene and the substrate. We expect that further investigations will unveil whether the topological edge state is realized in SiNR or not, by preparing the SiNR on a proper substrate, which sustains SiNR and has a weak interaction to SiNR. If it is realized, electron transport experiments on the single SiNR device such as the Hall bar and the spin-polarized STM techniques will make a significant contribution to the study of silicene.

(3) Magnetic properties of FePc

In Chapter 5, we focused on the magnetic properties of the Iron(II) phthalocyanine (FePc) molecule on Au(111). Fe ion of FePc on Au(111) has the integer spin $S = 1$. Furthermore, FePc adsorbed at the on-top site of Au(111) shows the two-stage Kondo resonance; the two spins in the $3d$ orbitals of Fe, which produce the $S = 1$ state, are both screened at the low temperature. This system is a good sample to investigate the Kondo physics at the single molecular/atomic scale; the competition between the Kondo effect and the spin-orbit coupling (SOC) and Hund coupling, the effect of the symmetry and anisotropy can be explored.

We have performed the STM contact measurement on FePc to induce the external perturbation from the STM tip to the Fe. In contrast to the non-contact geometry, both

the peak and dip structures in the *dI/dV* spectra, which are the signature of the Kondo resonance state, gradually vanished as the STM tip approached. The gradual changes of the spectra indicate that the two Kondo resonance states are suppressed in series; the second Kondo resonance state, which is a weaker Kondo singlet state (T_{K2} = 2.6 K), is first suppressed and then the first Kondo resonance state (T_{K1} ~ 150 K) is suppressed when the STM tip-FePc-Au junction is formed.

dI/dV spectra obtained at the contact geometry showed the IETS feature. By analyzing the magnetic field dependence of the excitation energies, we conclude that the spin state of Fe in the STM tip-FePc-Au junction is the unscreened S = 1 state which is similar to that of the bulk FePc.

DFT calculations also support our conclusion. The LDOS spectra and the differential charge mapping showed that the $3d_{z^2}$ orbital of Fe, which hosts the first Kondo resonance state, is strongly affected by the STM tip contact. We conclude that the first Kondo resonance state, which is a strongly coupled state (T_{K1} ~ 150 K), is vanished by the STM tip.

We demonstrated that the magnetic ground state of Fe of FePc on Au(111) can be tunable by controlling the distance between the STM tip and Fe. The two-stage Kondo resonance state is suppressed and the magnetic ground state becomes the unscreened S = 1 state by the STM tip contact. It has shown that the Kondo resonance state with the competing effects such as the SOC and Hund coupling is vulnerable to the external perturbation. We stress that the first Kondo resonance state has the high Kondo temperature (T_{K1} ~ 150 K), i.e., in order to decouple the Kondo resonance state by the thermal energy, we have to raise the temperature of the system around a hundred Kelvin. This result demonstrated that the STM contact measurement is useful to induce external perturbation and investigate the Kondo physics at a single molecule level.

In summary, we have performed the STM contact measurement in order to investigate the electron transport characteristics of single molecular junctions. We focused on the effect of the contact states; the geometric and electronic states of the molecule in contact with the STM tip. The effect of the contacting electrode (STM tip) was also discussed. We demonstrated that the STM contact measurement can unveil the effect of the STM tip contact on the electronic and magnetic properties: the relation between the electronic/magnetic properties and the contact states.

These results cannot be obtained without the precise controllability of the STM contact measurement together with the single-adsorbate-level spatial resolution of STM and the energy resolution of STS measurements. The STM contact measurements will make a great contribution to the physics of the single molecule.

Appendix

A1 Andreev Reflection

In order to introduce the mechanism of the multiple Andreev reflections (MARs), the *I-V* characteristics of the normal conductor/vacuum/superconductor (N/V/S) junction is introduced at the beginning. Figures A1.1(a) and (b) show the schematic energy diagram of the N/V/S junction. In this model, the temperature is regarded as the absolute zero temperature and the superconducting gap parameter is Δ. The superconducting gap region is denoted by the red color, where normal electrons (holes) cannot exist and only the Cooper pairs exist at this energy region. When the bias voltage $V_b = +\Delta$ is applied to the superconductor, electrons in the normal conductor can tunnel to the unoccupied state of the superconductor, as shown in Fig. A1.1(a). When V_b is applied to the opposite direction ($V_b = -\Delta$), the energy of the bias voltage eV_b breaks the Cooper pair and the

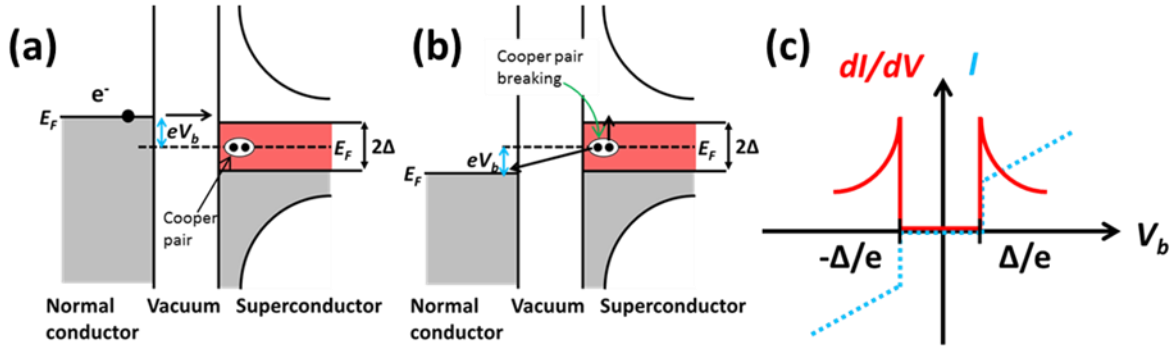

Fig. A1.1. (a) Schematic energy diagram of the normal conductor/vacuum/superconductor junction at the zero temperature. The superconducting gap is represented as the red color and the superconducting gap parameter is Δ. The two black filled circles in the white circle represent the Cooper pair. The bias voltage $V_b = \Delta$ is applied to the superconductor and the tunnel current flows from the normal conductor. (b) Similar schematic energy diagram when the polarity of the bias voltage is opposite. The Cooper pair is broken by the bias energy and the tunnel current flows, accompanied with the excitation of the one electron of the Cooper pair. (c) *I-V* and *dI/dV* spectra of the junction. The superconducting gap structure appears in the spectra.

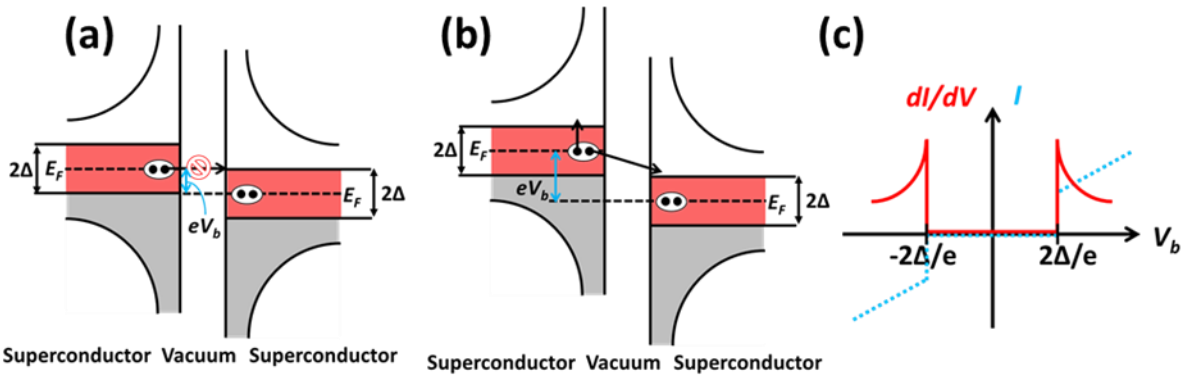

Fig. A1.2. (a) Schematic energy diagram of the superconductor/vacuum/superconductor junction at the zero temperature. The bias voltage $V_b = \Delta$ cannot induce enough energy to break the Cooper pair and the tunnel current cannot flow across the junction. (b) Similar schematic energy diagram with $V_b = 2\Delta$. The Cooper pair is broken by the bias energy and the tunnel current flows, accompanied with the excitation of the one electron of the Cooper pair. (c) *I-V* and *dI/dV* spectra of the junction. The sum superconducting gap are observed in the spectra.

current across the junction flows, as shown in Fig. A1.1(b). Hence, the superconducting gap structure appears in the *I-V* and *dI/dV* spectra of the junction, as shown in Fig. A1.1(c).

In the next step, let us consider the superconductor/vacuum/superconductor (S/V/S) junction. Again, the temperature is the absolute zero and the superconducting gap parameters of both superconductors are identical (Δ) in this model. Compared to the N/V/S junction, the current across the junction does not flow in the S/V/S junction at $V_b = \Delta$, as shown in Fig. A1.2(a). This is because the Cooper pair cannot tunnel to the state for the normal electrons (holes). The current can flow at $V_b = 2\Delta$, when the Cooper pair is broken in the same way shown in Fig. A1.1(b). As a result, the sum of the superconducting gap 2Δ is observed in the *I-V* and *dI/dV* spectra of the junction in Fig. A1.2(c). When the superconducting gap energies of the left and right superconductors are different (Δ_1 and Δ_2), the sum gap $\Delta_1 + \Delta_2$ appears in the spectra.

The Andreev reflection[1] occurs at the interface between the normal conductor and the superconductor (N-S interface). Figure A1.3 shows the schematic picture of the Andreev reflection. In the upper left picture, an electron in the normal conductor comes

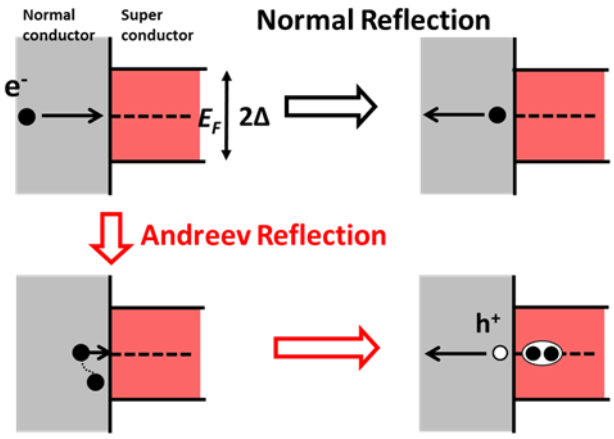

Fig. A1.3. Schematic views of the Andreev reflection. The gray and red regions represent the normal conducting and superconducting regions. The electron comes to the interface between the normal conducting and superconducting regions. The upper right image shows the normal reflection process, where the incident electron cannot enter into the superconducting region and is reflected due to the superconducting gap. The lower images show the Andreev reflection process. At a certain probability, the incident electron enters into the superconducting region by forming the Cooper pair with an electron in the normal conducting region. As a result, a hole is reflected.

to the N-S interface. The energy of the incident electron is in the region of the superconducting gap. Because of the superconducting gap, the incident electron cannot enter into the superconducting region and is reflected at the N-S interface, as shown in the upper right picture. This is called as the normal reflection process. In the Andreev reflection process, the incident electron finds another electron in the normal conductor to form the Cooper pair, as shown in the lower left picture. In this way, the incident electron enters into the superconducting region by forming the Cooper pair. Due to the charge conservation and energy conservation, the hole is reflected in the normal conductor, as shown in the lower right picture. In the same way, an incident hole forms a hole pair which can enter into the superconductor and an electron is reflected at the N-S interface. The process of the Andreev reflection is discussed by the Bogoljubov-de Gennes (BdG) equation[2,3]. The probability of the Andreev reflection depends on the potential barrier at the N-S interface[2]. When the N-S interface is clean and the electronic structures are

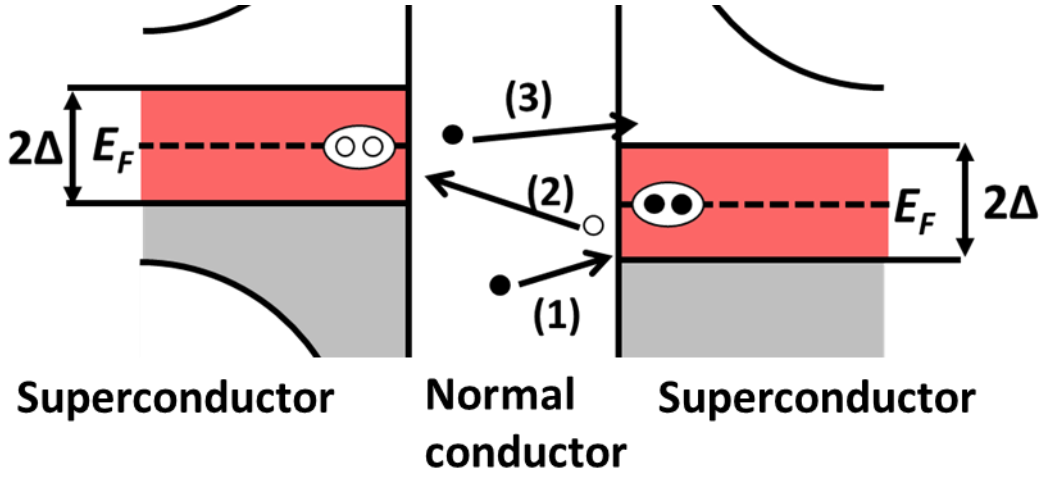

Fig. A1.4. Schematic image of the multiple Andreev reflection. The black filled circles are electrons and the blank circles are holes. A small bias voltage $V_b < 2\Delta$ is applied. In the superconductor/normal conductor/superconductor junction, a carrier in the normal conductor undergoes the Andreev reflection at the both interfaces. Since the charge of the carrier changes at the Andreev reflection, the carrier successively gains the bias energy and finally exceeds the superconducting gap energy as (1)→(2)→(3). As a result, current across the junction flows even when the bias voltage is low.

smoothly connected, the probability of the Andreev reflection is 100%. It follows that the conductance of the N/S junction is twice when $|V_b| < \Delta$ compared to $|V_b| > \Delta$.

The multiple Andreev reflection (MAR) is observed at the superconductor/normal conductor/superconductor (S/N/S) junction under the bias voltage[3-5]. The mechanism of the multiple Andreev reflection is schematically illustrated in Figure A1.4, using the quasi-classical picture. Under the bias voltage, an electron moves to the right N-S interface, denoted by (1). After the Andreev reflection at the right N-S interface, a hole is reflected. Because the charge is opposite, the reflected hole is then accelerated by the bias voltage and comes to the left N-S interface, denoted by (2). Again, the Andreev reflection occurs and the reflected electron finally obtains enough energy to enter into the unoccupied state of the right super superconductor. Hence, the current across the S/N/S junction flows even under a small bias voltage if the Andreev reflection occurs sequentially. As a result, the MAR produces a characteristic structure called subharmonic gap structure (SGS)[4,5] inside the superconducting gap region in the *I-V* and *dI/dV* spectra, which is

quite different from the *I-V* and *dI/dV* spectra of the S/V/S junction in Fig. A1.2(c). The *m*-times reflection process can carry the electric current across the junction when the bias energy eV_b reaches at $2\Delta/m$. The current of MAR in one transport channel is expressed in this form;

$$I_i(\tau_i, V) = \sum_{m=1}^{\infty} \theta(meV - 2\Delta)\, \tau_i^{\,m}\, K_m(\tau_i, V) \tag{A1}$$

where m is the number of the MAR processes, θ is the Heaviside step function, and K_m describes the current component carried by the m-fold Andreev reflections[6]. Figure A1.5 shows the calculated *I-V* spectra when the MAR occurs at the S/N/S junction. Note that the vertical axis is in the logarithmic scale and the *I-V* characteristics shown in Figure A1.5 show rapid increase at the $eV = 2\Delta/m$, which indicates the opening of the *m*-fold MAR process. In addition, the *I-V* characteristics depend strongly on the transmission coefficient τ. As stated before, the probability of the Andreev reflection depends on the potential barrier at the N-S interface, which determines the transmission (and reflection) probability at the interface. Hence, transmission coefficient τ relates with the probability

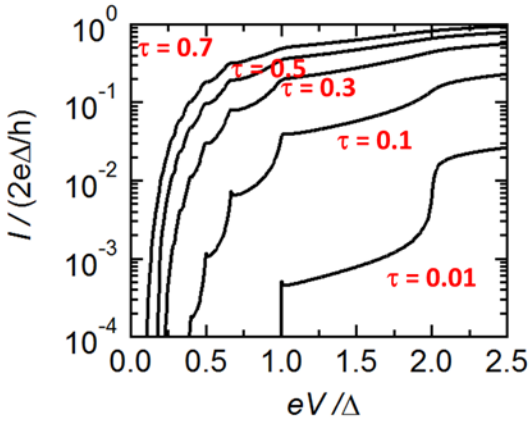

Fig. A1.5. Calculated *I-V* spectra for the single channel SNS junction when the multiple Andreev reflection occurs. The superconducting gap parameters Δ are same value for both superconductors. The vertical axis is in the logarithmic scale. The transmission coefficients τ are 0.01, 0.1, 0.3, 0.5 and 0.7 from the lower right spectra to the upper spectra.

of the Andreev reflection. It follows that the current contribution from the *m*-fold MAR process strongly depends on τ because the *m*-fold MAR process undergoes the Andreev reflection *m* times, which produces the term τ^m as shown in Eq. (A1).

Due to this non-linear and strong dependence on τ, we can resolve *I-V* spectra of the MAR which contains contributions from several channels into the contributions from each transport channel and evaluate the number of the transport channels and their transmission coefficients by the fitting analysis.

A2 Spin State of FePc

In this section, we describe the procedure of the analysis of the spin state of FePc discussed in Chapter 5.

The spins state of Fe (d^6) in FePc on Au(111) is considered to be $S = 1$ [Figs. A2.1(a),(b)]. The ground state is described by mixing the B_{2g} state ($d_{z^2} + d_{xy}$) into the E_g state ($d_{z^2} + d_{\pi}$). The B_{2g} state is energetically higher than the E_g state (the energy difference is Δ).

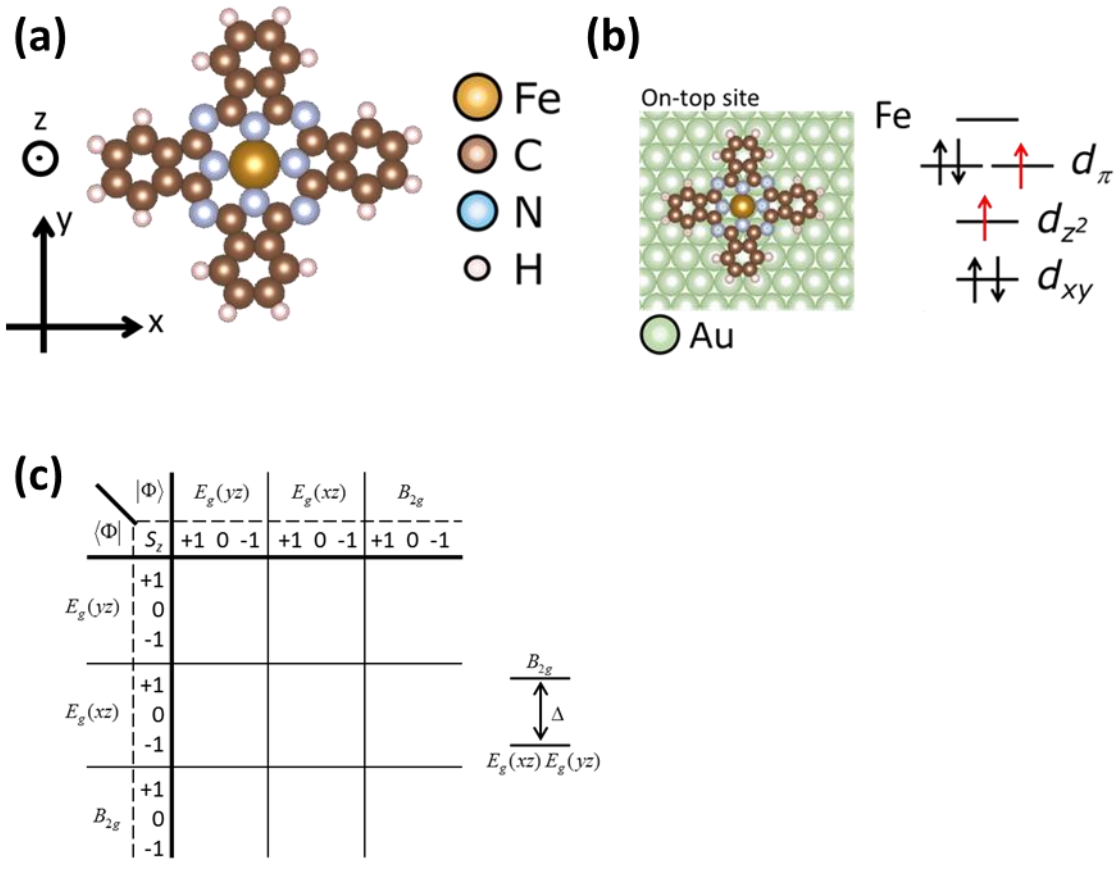

Fig. A2.1. (a) Molecular framework of FePc. The direction of the x,y,z axes are shown. (b) Schematic model of the on-top FePc on Au(111) and the electron configuration of Fe. (c) Schematic pictures of the 9x9 matrix considered in the model of the 2x2 Slater-determinant, which is identical to Fig. 5.2.

The Slater determinant (identical to Eq. 5.1) are as follows;

$$\begin{cases} E_g(yz):\frac{1}{\sqrt{2}}\left[\phi_{z^2}(1)\phi_{yz}(2)-\phi_{z^2}(2)\phi_{yz}(1)\right] \\ E_g(xz):\frac{1}{\sqrt{2}}\left[\phi_{z^2}(1)\phi_{xz}(2)-\phi_{z^2}(2)\phi_{xz}(1)\right] \\ B_{2g}:\frac{1}{\sqrt{2}}\left[\phi_{z^2}(1)\phi_{xy}(2)-\phi_{z^2}(2)\phi_{xy}(1)\right] \end{cases} \otimes \begin{cases} \alpha(1)\alpha(2) \\ \frac{1}{\sqrt{2}}\left[\alpha(1)\beta(2)+\alpha(2)\beta(1)\right], \\ \beta(1)\beta(2) \end{cases} \tag{A2}$$

where numbers 1 and 2 denotes the two holes, ϕ is the wave function of *d*-orbitals and α (β) is the up- (down-) spin function. The considered 9x9 matrix is schematically shown in Fig. A2.1(c), which is identical to Fig. 5.2.

The spin Hamiltonian (identical to Eq. 1.18) is the following equation:

$$H_{spin}=H_{SO}+H_{Zeeman}=\lambda\mathbf{L}\mathbf{S}+\mu_B\left(\mathbf{L}+g_e\mathbf{S}\right)\mathbf{H}, \tag{A3}$$

where $\mathbf{L}$ is the angular momentum operator, $\mathbf{S}$ is the spin operator, μ_B is the Bohr magneton g_e is the Landé factor, $\mathbf{H}$ is the magnetic fields (B_x, B_y, B_z). Operators $\mathbf{L}$ and $\mathbf{S}$ are in the forms below;

$$\mathbf{L}=\frac{\hbar}{i}\left[\mathbf{r}\times\text{grad }\right]=\frac{\hbar}{i}\begin{pmatrix} y\frac{\partial}{\partial z}-z\frac{\partial}{\partial y} \\ z\frac{\partial}{\partial x}-x\frac{\partial}{\partial z} \\ x\frac{\partial}{\partial y}-y\frac{\partial}{\partial x} \end{pmatrix}\equiv\frac{\hbar}{i}\begin{pmatrix}\mathbf{t_x}\\ \mathbf{t_y}\\ \mathbf{t_z}\end{pmatrix}, \tag{A4}$$

$$\mathbf{S}=\begin{pmatrix}\mathbf{S_x}\\ \mathbf{S_y}\\ \mathbf{S_z}\end{pmatrix},\quad \begin{cases} \mathbf{S_z}\left|S,S_z\right\rangle=S\left|S,S_z\right\rangle \\ \mathbf{S}_+\left|S,S_z\right\rangle=\sqrt{S(S-1)-S_z(S_z+1)}\left|S,S_z+1\right\rangle, \text{ where} \\ \mathbf{S}_-\left|S,S_z\right\rangle=\sqrt{S(S+1)-S_z(S_z-1)}\left|S,S_z-1\right\rangle \end{cases} \quad \begin{cases}\mathbf{S}_+=\mathbf{S_x}+i\mathbf{S_y}\\ \mathbf{S}_-=\mathbf{S_x}-i\mathbf{S_y}\end{cases}, \tag{A5}$$

where S and S_z are the spin quantum number and its projection to the z-axis. The wave functions of *d* orbitals are as follows:

$$\phi_{z^2}\propto\frac{2z^2-x^2-y^2}{r^2},\quad \phi_{xz}\propto\frac{xz}{r^2},\quad \phi_{yz}\propto\frac{yz}{r^2},\quad \phi_{xy}\propto\frac{xy}{r^2}. \tag{A6}$$

Considering the symmetry of the orbitals, the matrix elements $\langle\Phi|H_{spin}|\Phi\rangle$ are obtained as Fig. A2.2. Here, the magnetic fields $\mathbf{H}$ is (0, 0, B) since we applied the magnetic field along the z-axis in our experiments. For the visibility, the Bohr magneton

$\langle\Phi\vert$ \ $\vert\Phi\rangle$		$E_g(yz)$			$E_g(xz)$			B_{2g}		
	S_z	+1	0	-1	+1	0	-1	+1	0	-1
$E_g(yz)$	+1	$2\mu B$	0	0	$i\alpha + i\alpha\mu B$	0	0	0	β	0
	0	0	0	0	0	$i\alpha\mu B$	0	$-\beta$	0	β
	-1	0	0	$-2\mu B$	0	0	$-i\alpha + i\alpha\mu B$	0	$-\beta$	0
$E_g(xz)$	+1	$-i\alpha - i\alpha\mu B$	0	0	$2\mu B$	0	0	0	$-i\beta$	0
	0	0	$-i\alpha\mu B$	0	0	0	0	$-i\beta$	0	$-i\beta$
	-1	0	0	$i\alpha - i\alpha\mu B$	0	0	$-2\mu B$	0	$-i\beta$	0
B_{2g}	+1	0	$-\beta$	0	0	$i\beta$	0	$\Delta - 2\mu B$	0	0
	0	β	0	$-\beta$	$i\beta$	0	$i\beta$	0	Δ	0
	-1	0	β	0	0	$i\beta$	0	0	0	$\Delta - 2\mu B$

Fig. A2.2. Obtained matrix elements.

is written as μ and we treat the Landé factor $g_e = 2$. The terms α and β are the spin-orbit coupling (SOC) terms described as following integrations;

$$i\alpha = \int \phi_{yz}^{*}\, \mathbf{t_z}\, \phi_{xz}\, d\,\mathbf{r}$$
$$i\beta = \frac{1}{2\sqrt{2}} \int \phi_{yz}^{*}\, \mathbf{t_y}\, \phi_{xy}\, d\,\mathbf{r} = -\frac{1}{2\sqrt{2}} \int \phi_{xz}^{*}\, \mathbf{t_x}\, \phi_{xy}\, d\,\mathbf{r} \quad \text{(A7)}$$

Then, we calculated the eigenenergies by solving the determinant of the matrix. As shown in Fig. A2.3, three doublet states under the zero magnetic field (i) ~ (iii) and three singlet states (iv) are obtained. The third degree equation is numerically solved by the Cardano's method. In Fig. A2.4, we show the magnetic field dependence of the eigenenergies with the parameters (Δ, α, β) = (-56 meV, -3 meV, 12 meV), which is identical to Figs. 5.10(a) and (b). The singlet states are not sensitive to the magnetic fields in Fig. A2.4.

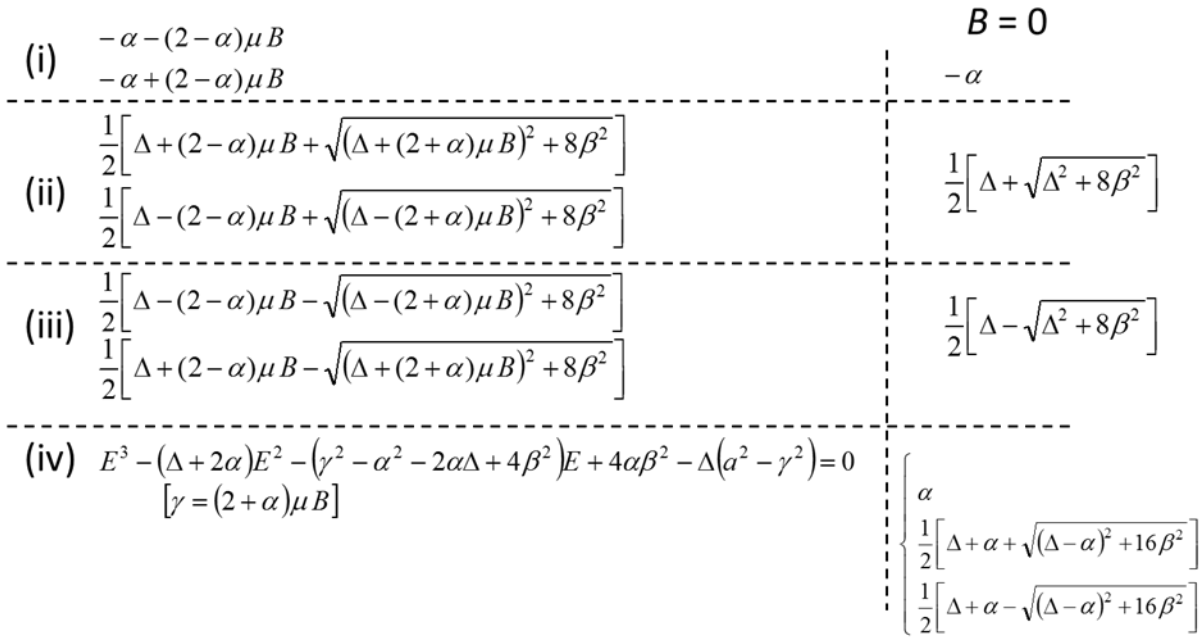

Fig. A2.3. Eigenenergies obtained from the matrix in Fig. A2.2. (i), (ii) and (iii) are the degenerated two states under the zero magnetic field and split as the magnetic field increases. (iv) contains three eigenenergies, where a third degree equation of E is shown. The eigenenergies under the zero magnetic field is also shown in the right side.

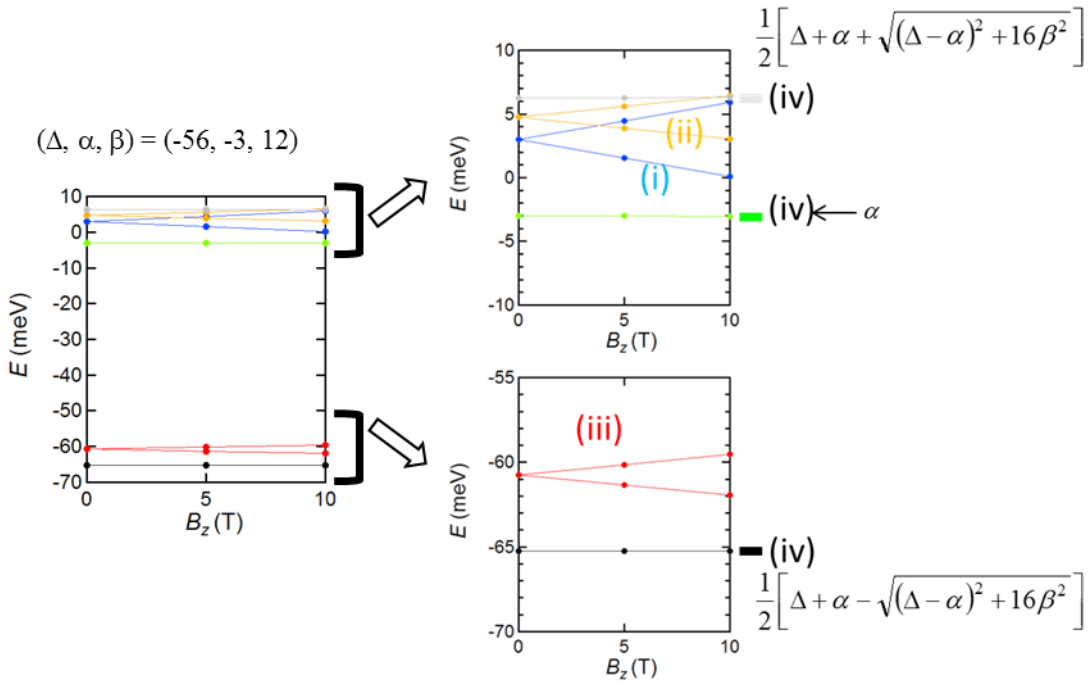

Fig. A2.4. Magnetic field dependence of the eigenstates. The parameters and the graph are identical to those of Figs. 5.10(a),(b). For the three eigenstates (iv), the corresponding energies at B = 0 are shown.

In Fig. A.2.5, we show the energy diagrams with different parameters. As expressed in the equations in Fig. A2.3, α and Δ determine the energy position of the states at the zero magnetic field and α determine the magnitude of the Zeeman splitting. When the absolute value of α is large compared to β and Δ, the three singlet states shifts depending on the magnetic field, as shown in the middle row in Fig. A2.5. In the right row, it can be seen that small β causes the crossing of the lowest two states (black and red).

The experimental results are as follows; there is single excitation process under the zero magnetic field and two excitation processes appear under the magnetic field, the lower excitation energy (ε_1) decreases and the higher excitation energy (ε_2) increases. In order to reproduce the experimental results, it is a presumable situation that the ground state is the singlet state and the first excited state is the doublet state. The other excited states should not cross the first excited state under the higher magnetic field. In addition, the energy of the SOC is expected to be a reasonable value; for reference, the SOC energy of Fe and Fe^{2+} ion are about 15 and 25 meV[7]. Under this restriction, we obtained the parameters reproducing of both our results and the bulk FePc by searching the parameters in the range: $\Delta = 0 \sim -70$, $\alpha = -25 \sim 25$, and $\beta = 0 \sim 40$.

Small α (= -3) is required to reproduce the Zeeman splitting of about 2.3 meV at B_z = 10 T and relatively large β (= 12) and Δ (= -56) is obtained to separate the eigenstates in a proper order and energy difference.

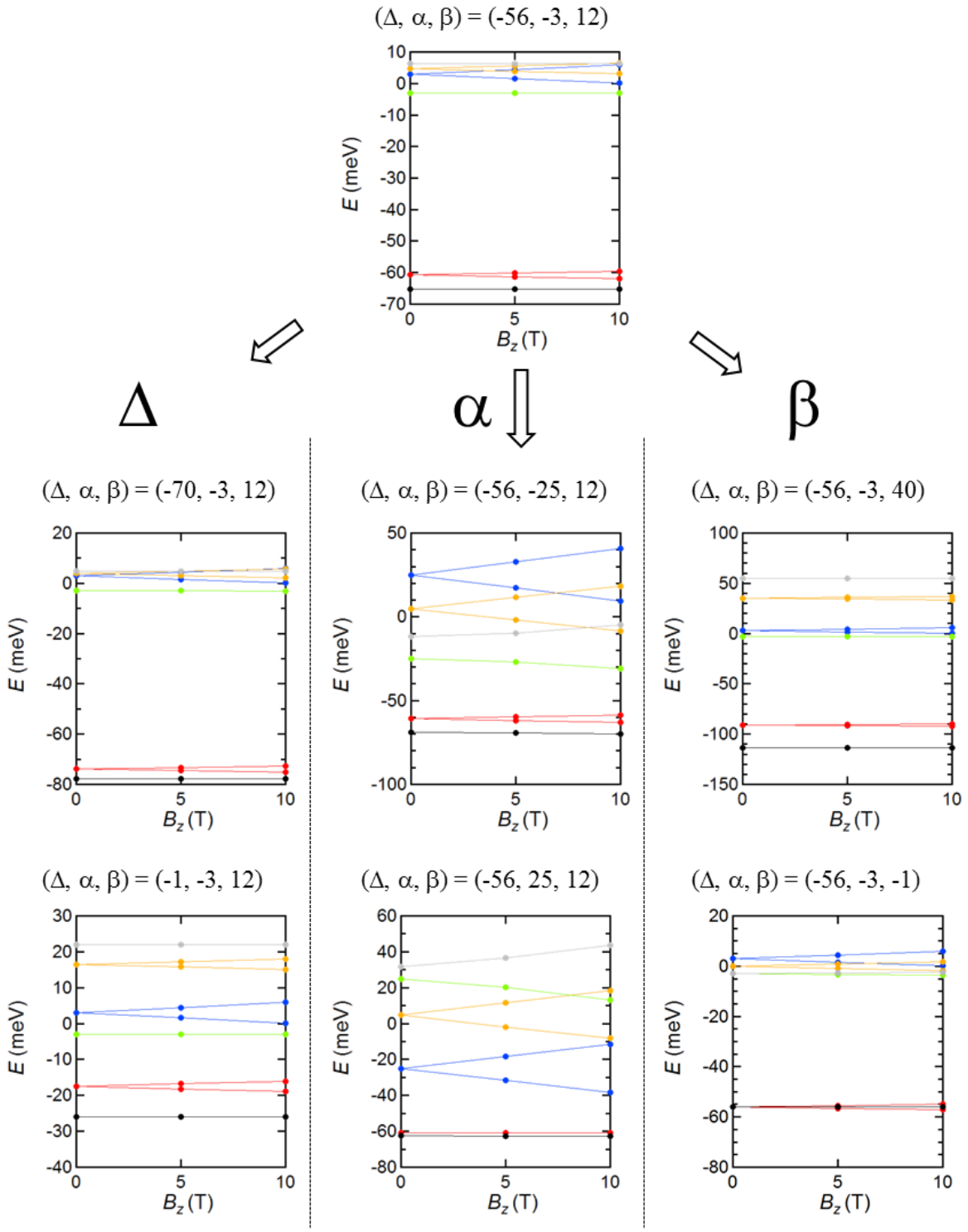

Fig. A2.5. Magnetic field dependence of the eigenstates with different parameters. The parameters are changed from (Δ, α, β) = (-56, -3, 12).

References

[1] Andreev, “The Thermal Conductivity of the Intermediate State in Superconductors”, Soviet Physics JETP-USSR **19,** 1228 (1964).

[2] G. E. Blonder, M. Tinkham, T. M. Klapwijk, “Transition from metallic to tunneling regimes in superconducting microconstrictions: Excess current, charge imbalance, and supercurrent conversion”, Phys. Rev. B **25,** 4515 (1982).

[3] Kulik, “Macroscopic Quantization and the Proximity Effect in S-N-S juncitons”, Soviet Physics JETP-USSR **30,** 944 (1970).

[4] T. M. Klapwijk, G. E. Blonder, M. Tinkham, “Explanation of subharmonic energy gap structure in superconducting contacts”, Physica **109 & 110B,** 1657 (1982).

[5] M. Octavio, M. Tinkham, G. E. Blonder, T. M. Klapwijk, “Subharmonic energy-gap structure in superconducting constrictions”, Phys. Rev. B **27,** 6739 (1983).

[6] E. N. Bratus, V. S. Shumeiko, and G. Wendin, “Theory of Subharmonic Gap Structure in Superconducting Mesoscopic Tunnel Contacts”, Phys. Rev. Lett. **74,** 2110 (1995).

[7] D. DAI, H. Xiang, and M. -H. Whangbo, “Effects of Spin-Orbit Coupling on Magnetic Properties of Discrete and Extended Magnetic Systems”, Journal of Computational Chemistry **29,** 2187 (2008).

Acknowledgement

博士論文を作成するにあたって、これまで私にお力をお貸し下さった多くの方々に感謝の意を表します。学士課程 4 年生の時に川合・高木研究室に迎えて頂いてから、修士課程そして博士課程まで長きに渡り、多くの方々にお世話になってきました。

特に、川合眞紀教授(Prof. Maki Kawai)、高木紀明准教授(Prof. Noriaki Takagi)、塚原規志助教(Dr. Tsukahara Noriyuki)、荒船竜一博士(Dr. Ryoichi Arafune)らには、私の研究室での研究において、新米のころから今日まで続けて、ご指導賜りました。

川合眞紀先生には、素晴らしい研究活動を行うことができる環境を与えて頂いたことを深く感謝いたします。最先端の研究に携わることができたこと、また、様々な学会に参加し、多くの優れた研究者の方々と触れ合う機会を与えて頂きました。川合先生にご教授頂くたびに、いつも私の中に新しく鮮烈な発想が湧き上がって来ました。自らの研究テーマに留まらず、科学というものについての考え方を広く学ばせて頂きました。

高木紀明先生には、常に熱心なご指導を賜りました。研究に対して前向きに取り組むことができたのも、高木先生のご指導あってのものでした。また、本論文を作製するにあたって、多くの示唆を頂戴できたことに深く感謝いたします。日々の研究室での生活において、アカデミックの世界や歴史に留まらず、大学や社会について広く学ぶことができました。

塚原規志先生には、研究室に配属された直後から、装置の取扱や実験の遂行にあたって多くのご指導を頂いたことを感謝いたします。FePc の実験とデータの解析を行うことができたのも、塚原先生のご指導のお蔭です。

荒船竜一先生には、C_{60} や SiNR の実験について、ディスカッションにお付き合いいただけたことを感謝いたします。加えて、シミュレーションのためのプログラミングや、VASP による第一原理計算など多くのサポートを頂けましたことを重ねて感謝いたします。

白木将先生(Dr. Susumu Shiraki)には、学士課程 4 年生の時にご指導賜りました。本論文の C_{60} の研究の取り掛かりのところで多くのご指導を頂きましたことを感謝致します。

林俊良先生(Dr. Chun-Liang Lin)には、実験が難航している際にも、積極的なご協力を頂けたことを感謝いたします。SiNR の実験において、実験の部分を多く助けて頂きました。いつも前向きな姿勢で励まして下さり、私も頑張ることができました。

また、理化学研究所の表面化学研究室の方々、ならびに Kim 表面界面科学研究室の方々には、セミナーでの議論を通して、多くの知見を頂けたことを感謝いたします。山田太郎先生(Dr. Taro Yamada)、金有洙先生(Dr. Yousoo Kim)、加藤浩之先生(Dr. Hiroyuki S. Kato)、南任真史先生(Dr. Masashi Nantoh)、清水智子博士(Dr. Tomoko K. Shimizu)、湊丈俊博士(Dr. Taketoshi Minato)、今田裕博士(Dr. Hiroshi Imada)、南谷英美博士(Dr. Emi Minamitani)、竹本整司さん(Dr. Seiji Takemoto)、みなさまに感謝を捧げます。

これまで川合・高木研究室で過ごした日々において、多くの先輩方にお世話になりました。松永宗一郎(Dr. Soichiro Matsunaga)さま、本林健太(Dr. Kenta Motobayashi)さま、鄭載勲さま(Dr. Jaehoon Jung)、高田有理子さま、土肥真路さま、能登健一さま、八百篤史さま、山本真祐子さま、金柱亨さま(Dr. Ju-Hung Kim)、伊藤彩香さま、岩谷忠彦さま、大谷徹也さま、鎌倉真一さま、酒井真利さま、高見剛史さま、梁賢眞さま(Dr. Hyun Jin yang)、数々の貴重な学び、体験、思い出を下さりありがとうございました。

同期の仲間たちには、日常生活から研究や発表といった課題に取り組む際に、いつも支えて頂けたことを感謝いたします。太田奈緒香さま、野村周平さま、福嶋徹さま、水澤岳さま、高橋祥子さま、杉山一生さま、難波江裕之さま、本当にありがとうございました。

また、多くの後輩たちにも、常に刺激を頂くことができ、自らの向上心の原動力とすることができました。今井みやびさん、木内久雄さん、清水裕章さん、寺内悠さん、仲村裕也さん、橋本千歩さん、川原一晃さん、中澤武夫さん、中村耕太郎さん、柚木崎航平さん、稲員慎一さん、閑野真央さん、長尾遼さん、古島弥来さん、森田和孝さん、太田仁孝さん、奥村元さ

ん、川上直也さん、河原祥太さん、進藤一樹さん、木村謙介さん、篠塚正之さん、下村遼さん、ありがとうございました。

秘書の和泉嘉枝さま、小倉洋子さま、小林恵さま、清水佳子さまには、研究室でのさまざまな活動において、いつも笑顔で助けて頂けたことに感謝いたします。

大学での生活全般において、多くの精神的助けを下さった友人たちに感謝の意をささげたいと思います。石崎翔太氏、大政直也氏、小名木悠輝氏、千葉大紀氏、中田行洋氏、藤田剛氏、前田泰一氏には特に感謝したいと思います。

最後になりますが、これまでの長きに渡り、大学での学業に専念することができたのは、経済的・精神的に支えて下さった父母、祖父母、また妹弟のお蔭です。ここに最大限の感謝を捧げます。

平岡　諒一

Ryoichi Hiraoka

Publication List

- Ryoichi Hiraoka, Ryuichi Arafune, Noriyuki Tsukahara, Maki Kawai, and Noriaki Takagi, "Transport characteristics of a single C_{60}-molecule junction revealed by multiple Andreev reflections", Phys. Rev. B **90,** 241405 (2014).

- R. Hiraoka, Chun-Liang Lin, Ryuichi Arafune, Noriyuki Tsukahara, Maki Kawai, and Noriaki Takagi, "Edge state of silicene nano ribbon measured by STM junction", *In preparation.*
- R. Hiraoka, Noriyuki Tsukahara, Maki Kawai, and Noriaki Takagi, "Control of adsorption site of individual FePc molecule on Au(111) and respective spectroscopic characters", *In preparation.*
- R. Hiraoka, Noriyuki Tsukahara, Maki Kawai, and Noriaki Takagi, "Direct manipulation of multi-stage Kondo resonance state in FePc on Au(111) by STM tip contact", *In preparation.*